Technical Report
RAL-TR-1998-029

CLRC

Parton Distributions: A New Global Analysis

A D Martin R G Roberts W J Stirling and R S Thorne

March 1998

COUNCIL FOR THE CENTRAL LABORATORY OF THE RESEARCH COUNCILS

Enquiries about copyright, reproduction and requests for additional copies of this report should be addressed to:

The Central Laboratory of the Research Councils
Library and Information Services
Rutherford Appleton Laboratory
Chilton
Didcot
Oxfordshire
OX11 0QX
Tel: 01235 445384 Fax: 01235 446403
E-mail library@rl.ac.uk

ISSN 1358-6254

RAL-TR-98-029
DTP/98/10
March 1998

Parton distributions : a new global analysis

A. D. Martin[a], R. G. Roberts[b], W. J. Stirling[a,c] and R. S. Thorne[d]

[a] *Department of Physics, University of Durham, Durham, DH1 3LE*
[b] *Rutherford Appleton Laboratory, Chilton, Didcot, Oxon, OX11 0QX*
[c] *Department of Mathematical Sciences, University of Durham, Durham, DH1 3LE*
[d] *Jesus College, University of Oxford, Oxford, OX1 3DW*

Abstract

We present a new analysis of parton distributions of the proton. This incorporates a wide range of new data and an improved treatment of heavy flavours and prompt photon production. The new set (MRST) shows systematic differences from previous sets of partons which can be identified with particular features of the new data and with improvements in the analysis. We also investigate the sensitivities of the results to (i) the uncertainty in the determination of the gluon at large x, (ii) the value of $\alpha_S(M_Z^2)$ and (iii) the minimum Q^2 cut on the data that are included in the global fit.

1. Introduction

The last few years have seen a spectacular improvement in the precision and in the kinematic range of the experimental measurements of deep inelastic and related hard scattering processes. As a consequence the parton distributions of the proton are much better known, with tight constraints on the gluon and the quark sea for Bjorken x as low as 10^{-4}. However, several significant sets of new data have become available recently which, when incorporated in a global analysis, will increase considerably our knowledge of the parton distributions.

First let us summarize the new experimental measurements that have become available, and their implications. The new information includes the following.

(i) We have new, more precise, measurements of the structure function F_2^{ep} for deep inelastic electron-proton scattering by the H1 and ZEUS collaborations at HERA [1, 2]. The data now extend over a much wider kinematic range. Loosely speaking F_2 and $\partial F_2/\partial \ln Q^2$ serve to constrain the sea quark and gluon[1] distributions in the region $10^{-4} \lesssim x \lesssim 10^{-2}$.

(ii) A re-analysis of the CCFR neutrino data has led to a new set of $F_2^{\nu N}$ and $xF_3^{\nu N}$ structure function measurements [3]. Besides affecting the quark densities, the new structure functions give a value of the strong coupling α_S much more in line with the world average determination than the original CCFR data [4].

(iii) There now exist measurements of the charm component of F_2^{ep} in electron-proton deep inelastic scattering at HERA [5, 6]. These new data sample $x \sim 10^{-3}$ and complement the existing EMC charm data with $x \sim 10^{-1}$ [7]. Such data constrain both the charm sea and gluon distributions via the subprocesses $\gamma^* c \to c$ and $\gamma^* g \to c\bar{c}$ respectively.

(iv) Very precise measurements of prompt photon production, $pp \to \gamma X$, have become available from the E706 collaboration [8]. These data motivate us to look again at our treatment of this reaction, and in particular of the WA70 prompt photon measurements [9]. We emphasize that such prompt photon data are the main constraints on the gluon[2] outside the HERA small x ($x \sim 10^{-3}$) domain, apart of course from the global momentum sum rule constraint.

(v) The E866 collaboration [10] have measured the asymmetry in Drell-Yan production in pp and pn collisions over an extended x range, $0.03 \lesssim x \lesssim 0.35$. The asymmetry data provide direct information on the x dependence of the difference, $\bar{u} - \bar{d}$, of the sea quark densities. Previously there existed only the single measurement of NA51 [11] at $x = 0.18$, which revealed that $\bar{d} \simeq 2\bar{u}$ at this x value. Now much more information on $\bar{u} - \bar{d}$ is available[3].

[1] At the lower values of Q^2 there is a significant correlation between $g(x, Q^2)$ and the value of the strong coupling $\alpha_S(Q^2)$.

[2] Other reactions can in the future offer important constraints on the gluon, see (ix) below.

[3] See also Section 7.2 where information on $\bar{u} - \bar{d}$ from semi-inclusive deep inelastic data is discussed.

(vi) The CDF collaboration [12] have been able to considerably improve the precision of their measurements of the asymmetry of the rapidity distributions of the charged lepton from $W^{\pm} \to l^{\pm}\nu$ decays at the Tevatron $p\bar{p}$ collider. The new data extend to larger values of lepton rapidity. These data offer a tight constraint on the u/d ratio of parton densities.

(vii) NMC have now completed their structure function analysis, and supplied further data on $F_2^{\mu p}$, $F_2^{\mu d}$ and the ratio $F_2^{\mu d}/F_2^{\mu p}$ [13]. The dedicated measurement of the ratio provides a valuable constraint on the u/d ratio.

(viii) The data on Drell-Yan production obtained by the E772 collaboration [14] cover a wider range of x_F than the E605 data [15] which we have used to constrain the sea. For $x_F \sim 0$ both experiments provide a useful measure of the quark sea at larger values of x, typically $x \lesssim 0.3$. For larger x_F the E772 data probe, in principle, the valence quarks at $x \sim 0.5$ and the sea quarks at $x \sim 0.025$.

(ix) There are several other data sets which have the potential to provide important information on partons in the future. These include jet, $W+$ jet and heavy quark (b, t) production at Fermilab, and diffractive J/ψ and dijet production at HERA, as well as jet production in deep inelastic scattering.

The paper is organized as follows. In Section 2 we describe our procedure and the input parametrization of the partons. The optimum global set of partons, which we denote simply MRST, is presented together with two other sets which represent the possible range of behaviour of the gluon[4]. The quality of the description of the deep inelastic scattering data is shown in Section 3. The sensitivity to the cuts imposed on the data that are fitted and to the value of α_S are also discussed. In Section 4 we study the impact of the prompt photon data on the determination of the gluon. We pay particular attention to the transverse momentum (k_T) smearing of the incoming partons. In Section 5 we present a self-contained discussion of our new treatment of the heavy flavour (c, b) contributions to the structure functions. The description of the data for the Drell-Yan process is given in Section 6 and in Section 7 we discuss the (u, d, s) flavour decomposition of the sea. Section 8 is devoted to the constraint imposed by the new W asymmetry data. Some implications of the impact of our new partons for processes observed at the Fermilab Tevatron collider are presented in Section 9. Finally in Section 10 we summarize the key features of our analysis.

2. Global parton analysis

The parton distributions f_i are determined from a global fit to a wide range of deep inelastic and related hard scattering data. The basic procedure is to parametrize the $f_i(x, Q^2)$ at a low value of $Q^2 = Q_0^2$ such that the $f_i(x, Q^2)$ can be calculated at higher Q^2 by using next-to-leading-order (NLO) DGLAP (Dokshitzer-Gribov-Lipatov-Altarelli-Parisi) evolution equations. Data

[4]The FORTRAN code for all the parton sets described in this paper can be obtained from `http://durpdg.dur.ac.uk/HEPDATA/PDF`, or by contacting `W.J.Stirling@durham.ac.uk`.

are fitted for all $Q^2 > Q_1^2$, where $Q_1^2 > Q_0^2$ is a value of Q^2 where perturbative QCD is believed to be the dominant contribution. We shall study the sensitivity of the results to variation of the choice of Q_1^2.

We parametrize the starting parton distributions at $Q^2 = Q_0^2 = 1$ GeV^2 where the number of active flavours is $n_f = 3$. We work in the $\overline{\rm MS}$ renormalization scheme and use the starting parametric forms

$$xu_v = A_u x^{\eta_1}(1-x)^{\eta_2}(1+\epsilon_u\sqrt{x}+\gamma_u x) \quad (1)$$

$$xd_v = A_d x^{\eta_3}(1-x)^{\eta_4}(1+\epsilon_d\sqrt{x}+\gamma_d x) \quad (2)$$

$$xS = A_S x^{-\lambda_S}(1-x)^{\eta_S}(1+\epsilon_S\sqrt{x}+\gamma_S x) \quad (3)$$

$$xg = A_g x^{-\lambda_g}(1-x)^{\eta_g}(1+\epsilon_g\sqrt{x}+\gamma_g x). \quad (4)$$

The flavour structure of the light quark sea at Q_0^2 is taken to be

$$2\bar{u} = 0.4S - \Delta \quad (5)$$

$$2\bar{d} = 0.4S + \Delta \quad (6)$$

$$2\bar{s} = 0.2S \quad (7)$$

where the $2\bar{s}/(\bar{u}+\bar{d})$ ratio of 0.5 is chosen to obtain a $\bar{s}$ density consistent with the CCFR data on dimuon production [16], see Fig. 29 of Section 7. The parametric form of Δ, which specifies the difference between $\bar{u}$ and $\bar{d}$, is taken to be

$$x\Delta \equiv x(\bar{d}-\bar{u}) = A_\Delta x^{\eta_\Delta}(1-x)^{\eta_S+2}(1+\gamma_\Delta x+\delta_\Delta x^2). \quad (8)$$

The data require the integral $\int_0^1 dx(\bar{d}-\bar{u})$, which occurs in the Gottfried sum rule, to be positive. For the parton sets obtained in this analysis the integral is approximately equal to 0.1 giving a Gottfried sum

$$I_{\rm GS} \equiv \int_0^1 \frac{dx}{x}[F_2^p - F_2^n] \approx 0.27 \quad (9)$$

in the region $Q^2 \approx 5$ GeV^2. The relevant data are the measurements of the asymmetry in Drell-Yan production in pp and pn collisions. The pioneering experiment of the NA51 collaboration [11] measured the asymmetry at one value of x, $x = 0.18$. Very recently the E866 collaboration [10] have made measurements over a range of x. The new data indicate that, while indeed $x\Delta > 0$ for $x \lesssim 0.2$, for larger x values $\Delta \equiv \bar{d} - \bar{u}$ becomes small and may even become negative. The structure of $x\Delta$ is accommodated in our parametrizations by negative values of δ_Δ. To ensure that the individual densities $\bar{u}$ and $\bar{d}$ are both positive at all x, we suppress the difference Δ at very large x by an extra factor of 2 in the exponent of $(1-x)$, see (8).

For the first time our treatment of the heavy flavour densities, charm and bottom, is on a firm theoretical footing. These densities are determined by the other parton distributions and no extra parameters are introduced apart from the heavy quark masses. At very low Q^2 the structure functions $F_2^H(x,Q^2)$, with $H = c, b$, are described by boson-gluon fusion and the

heavy quark densities turn on at $Q^2 \simeq m_H^2$. The procedure for ensuring a smooth continuation in the behaviour of F_2^H in the threshold region is described in Section 5.

A new feature of our analysis is the particular attention to the uncertainties in the gluon distribution at large x. The main constraints in this region are data on prompt photon production in pp or pA collisions from the WA70 [9] and the E706 [8] experiments. The latter data confirm the implication from other high energy prompt photon experiments [17] that a significant initial state partonic transverse momenta is needed to obtain agreement with the NLO QCD prediction [18]. This naturally raises the question whether such a transverse momentum component should be included when determining the behaviour of the gluon at large $x(x \simeq 0.4)$ from the lower energy ($\sqrt{s} = 23$ GeV) WA70 measurements — even though the WA70 data can be adequately described without such a component[5]. We find[6] that the E706 data, which correspond to $\sqrt{s} = 31.5$ and 38.8 GeV, require the average value of the transverse momentum of the initial partonic system $\langle k_T \rangle \sim 1$ GeV, and we expect this to be less for experiments at lower energies. We therefore begin by taking a canonical value of $\langle k_T \rangle = 0.4$ GeV for the analysis of the WA70 data at $\sqrt{s} = 23$ GeV. We then explore a range of gluon distributions which result from global analyses in which $\langle k_T \rangle$ goes from one extreme of $\langle k_T \rangle = 0$ to the other $\langle k_T \rangle = 0.64$ GeV, which is the maximum value that we find compatible with a reasonable description of the WA70 data, see Section 4. We call the gluon distributions which correspond to $\langle k_T \rangle = 0$, 0.4 and 0.64 GeV the higher, central and lower (large x) gluons respectively — since a smaller gluon density is compensated by a larger $\langle k_T \rangle$. We denote the corresponding parton sets by MRST($g\uparrow$), MRST and MRST($g\downarrow$). The three choices of the large x gluon behaviour give, we believe, a realistic indication of the uncertainty of the gluon distribution due to the transverse momentum of the initial state partons. Table I lists the values of the parameters of (1)-(4),(8) for the three parton sets.

The optimum global MRST description has the QCD parameter $\Lambda_{\overline{\rm MS}}(n_f = 4) = 300$ MeV, which corresponds to $\alpha_S(M_Z^2) = 0.1175$, in excellent agreement with the world average value $\alpha_S(M_Z^2) = 0.118$ [19]. The same α_S value is also used for the MRST($g\uparrow$ and $g\downarrow$) partons[7]. In the literature errors between ± 0.005 and ± 0.003 are quoted on the world average value of $\alpha_S(M_Z^2)$. In Section 3.3 we will present parton sets which cover the range given by the more conservative error of ± 0.005, in each case taking $\langle k_T \rangle = 0.4$ GeV when analysing the WA70 data.

From Table I we see that the values of λ_g are negative, which imply a 'valence' type of behaviour for the gluon at low x for $Q^2 = 1$ GeV^2. Care should be taken not to attach physical significance to this behaviour, as it arises from an 'extrapolation' outside the domain of the fitted data. Indeed as Q^2 increases the behaviour rapidly changes so that by $Q^2 = 2$ GeV^2 the gluon distributions are approximately 'flat' in x. Fig. 1 shows the three gluon solutions as Q^2 varies from 2 to 100 GeV^2 and we can see how evolution up in Q^2 soon blurs the distinction between

[5] In previous MRS analyses of the WA70 data we did not include initial state transverse momentum.

[6] The calculation is described in Section 4 and compared with existing descriptions of the E706 data.

[7] The optimum value of $\alpha_S(M_Z^2)$ for the ($g\uparrow$ and $g\downarrow$) parton sets is close to that of the central gluon fit.

the initial starting distributions. Notice also that at low Q^2 the distinct behaviour at $x \sim 0.4$ is compensated by the opposite behaviour at $x \sim 0.05$ so that in each case the momentum fraction carried by the gluon remains at roughly 35% at $Q_0^2 = 1$ GeV^2. This structure is more evident in Fig. 2 which shows the ratio of the gluons at $Q^2 = 10$ and 10^4 GeV^2. We see that all our three gluon distributions converge for $x \lesssim 0.01$ due to the requirement of fitting the HERA data. The CTEQ4M [20] gluon distribution is also shown[8] and the comparison will be discussed later.

Table II lists the fraction of momentum carried by the individual partons as a function of Q^2 for the central solution, MRST. For $Q^2 = 200$ GeV^2, for example, 46%, 31% and 23% is carried by the gluon, valence and sea quarks respectively. In fact the flavour decomposition of the sea momentum fraction is

$$u,\ d,\ s,\ c,\ b\ =\ 7,\ 8,\ 5,\ 3,\ 1\%, \tag{10}$$

demonstrating the growth of the strange, charm and bottom distributions with increasing Q^2.

The wide range of processes used in the global analyses is listed in Table III. We include deep inelastic scattering (DIS) data from H1[1], ZEUS[2], BCDMS[22], NMC[13], E665[23], SLAC[24] and CCFR[3]. In general we only fit to DIS data with $Q^2 > 2$ GeV^2 and $W^2 > 10$ GeV^2, but in order to include very small x measurements of F_2^{ep} we admit the HERA data for Q^2 down to 1.5 GeV^2. Compared to our 1996 global analysis [25], the HERA data are updated to include the H1 shifted vertex as well as nominal vertex data, the NMC data now include all five beam energies and, finally, we use the reanalysed CCFR neutrino data. Table IV shows the χ^2 values for all these DIS data for the three 'gluon' fits described above. The important constraints from non-DIS data are discussed in detail in later sections. The upper plot of Fig. 3 shows the MRST parton distributions as a function of x for $Q^2 = 20$ GeV^2 while the lower plot compares them with those of MRS(R2), our favoured set of the previous analysis [25]. Fig. 4 shows the same plots at $Q^2 = 10^4$ GeV^2. We discuss the comparison of the new partons with previous sets in Section 10.

3. Description of DIS data

The description of the DIS structure function data by the MRST partons is shown in Figs. 5–11. Overall the quality of the fit is satisfactory as reflected by the χ^2 values listed in Table IV. However, it is informative to note special features of the fit and, in particular, to highlight those areas in which the description of the DIS data is systematically poorer than average.

A comparison with the small x data that are used in the fit is shown in Fig. 5. For the purposes of illustration, data at adjacent x values are grouped together at a mean value, together with the MRST fit. Very recently the H1 collaboration [26] have made available unpublished preliminary measurements of F_2 from the 1996 run. These data are not included in the fit but

[8]Very recently CTEQ [21] have attempted to estimate the uncertainty on the gluon, without using any constraints from prompt photon data.

a comparison with MRST is shown in Fig. 6. It is clear that the data in Fig. 5 are sufficient to put strong constraints on the small x behaviour of both the sea quark and gluon distributions. Loosely speaking F_2 and $\partial F_2/\partial \ln Q^2$ determine the $x^{-\lambda}$ exponents, λ_S and λ_g, of the sea and gluon distributions respectively, as well as constraining the overall normalization. The values of λ_S and, particularly, λ_g depend sensitively on the value of $Q^2 = Q_0^2$ chosen to parametrize the input distributions.

We may look at how the exponents λ_S and λ_g vary with Q^2 by fitting the sea quark and gluon distributions of the MRST partons to the forms

$$xf_i(x,Q^2) \;=\; A(Q^2)x^{-\lambda_i(Q^2)} \tag{11}$$

as $x \to 0$. The results are shown in Fig. 12. As Q^2 increases from the input scale, $Q_0^2 = 1$ GeV^2, we see that the valence-like character of the gluon rapidly disappears due to evolution being driven by the much steeper sea, and that by $Q^2 \simeq 2$ GeV^2 the gluon is 'flat' in x, that is $\lambda_g = 0$. By $Q^2 \simeq 6$ GeV^2 we see that $\lambda_g = \lambda_S$, which incidentally is close to the assumption[9] made in the early NLO global analyses in which the input scale was chosen to be $Q_0^2 = 4$ GeV^2. For higher values of Q^2 the gluon exponent 'leads' that of the sea, $\lambda_g > \lambda_S$, since the gluon drives the sea quark distribution via the $g \to q\bar{q}$ transition.

Fig. 13 is an alternative way of looking at the quality of the description of $\partial F_2/\partial \ln Q^2$ at low x. The continuous curves on the plots show the values of the slope $\partial F_2/\partial \ln Q^2$ versus x for both the H1 and ZEUS data, compared with the slope found in the MRST fit (evaluated at the particular values of Q^2 appropriate to the experimental data). Though the overall description is satisfactory, it is possible that for $x \lesssim 10^{-3}$ there may be a systematic difference between the data and the fit which reflects the onset of $\ln 1/x$ contributions which are outside the scope of our NLO DGLAP analysis. This systematic trend is even more evident in the preliminary H1 data from the 1996 run [26]. As the precision of the HERA measurements of F_2 improves, it will be interesting to see whether or not the statistical significance of the discrepancy increases.

The description of the NMC DIS data [13] for F_2^p and F_2^d is shown in Fig. 7 and Fig. 8. It is apparent that the data have systematically a larger slope, $\partial F_2/\partial \ln Q^2$, than the fit. This is well illustrated by the continuous curve in Fig. 14 which shows $\partial F_2/\partial \ln Q^2$ for the NMC F_2^p data. The discrepancy indicates that the NMC data would prefer a larger gluon in this x region and/or a larger α_S value than that of MRST. In turn the larger gluon would imply (by momentum conservation) a smaller gluon in the very small x domain, contrary to the HERA data. The fit is a compromise between these data sets, but it demonstrates the tight constraints now imposed by the increased precision of the F_2 data. A particular virtue of the NMC data is the accurate measurement of F_2^n/F_2^p. We postpone a study of their implications until we discuss the description of the asymmetry in Drell-Yan production in pp and pn collisions and the rapidity asymmetry in the processes $p\bar{p} \to W^{\pm}X$.

[9] Approaches in which λ_S is tied to λ_g at lower scales (say $Q_0^2 < 2$ GeV^2), as in the dynamical GRV model [27], will clearly have difficulty in fitting the new HERA data.

The BCDMS data [22] cover the range $0.1 \lesssim x \lesssim 0.75$ and are the most precise data at large x, see Fig. 9. From the figure it is apparent that the data would prefer a smaller value of α_S than that found in the global fit, namely $\alpha_S(M_Z^2) = 0.1175$. Indeed if the BCDMS data are analysed on their own (apart from including SLAC data [24] to constrain the higher twist contribution) then $\alpha_S(M_Z^2)$ is found to be 0.113 ± 0.005 [29]. Our optimum value of α_S is therefore within a standard deviation of the BCDMS determination.

The re-analysed CCFR neutrino measurements of $F_2^{\nu N}$ and $xF_3^{\nu N}$ are compared with the MRST values in Figs. 10 and 11. The long-standing discrepancy between the CCFR $F_2^{\nu N}$ and the NMC $F_2^{\mu d}$ measurements for $x \lesssim 0.1$ remains: in this x region the $F_2^{\nu N}$ measurements are in excess of the $F_2^{\mu d}$ data by a significantly larger amount than that implied by the strange quark distribution[10] determined from dimuon data, see Fig. 29 of Section 7.1. However, it is important to note that the neutrino data must be corrected for heavy target effects. In Figs. 10 and 11 we have subjected the MRST curves to a heavy target correction. The parametric form that we use for the correction factor is deduced from deep inelastic data for the scattering of muons on heavy targets. The correction factor that we obtain in this way is more severe at low x than that implied by shadowing. This is one reason why the (dashed) curves are considerably below the $x < 0.1$ neutrino data. It is not clear whether the correction factor should be the same for neutral current and charged current DIS data, or be the same for F_2 and xF_3 neutrino data. For these reasons we do not include the CCFR heavy target data for $x < 0.1$ in the fit. The remaining neutrino data are well described. However, it is possible to see that the fit slightly underestimates the slopes as a function of $\ln Q^2$, which reflects the value $\alpha_S(M_Z^2) = 0.119$ obtained from fitting to the neutrino data alone [3].

3.1 F_L and implications for partons

In the DIS experiments it is not the structure function $F_2(x, Q^2)$ which is measured directly but the differential cross section. Defining the rescaled differential cross section

$$\tilde{\sigma}(x, Q^2) = \frac{Q^4 x}{2\pi\alpha^2} \frac{1}{[1 + (1-y)^2]} \frac{d^2\sigma}{dx dQ^2}, \tag{12}$$

where $y = Q^2/xs$, we have

$$\tilde{\sigma}(x, Q^2) = F_2(x, Q^2) - \frac{y^2}{[1 + (1-y)^2]} F_L(x, Q^2). \tag{13}$$

Since both y and F_L are usually small the latter term in this expression is usually negligible, and the measurement of F_2 is effectively direct.

However, the analysis of data on the longitudinal structure function $F_L(x, Q^2)$ is in principle an important probe of the parton distributions. This is particularly the case for the gluon at small x since in this region, to a good approximation, we have the relationship

$$xg(x, Q^2) = 5.9(3\alpha_S/4\pi) F_L(0.4x, Q^2) \tag{14}$$

[10] Recall, at LO, that $xs(x) = \frac{5}{6} F_2^{\nu N}(x) - 3F_2^{\mu d}(x)$.

for three massless flavours [30] at leading order in α_S (though the next-to-leading correction leads to an increased gluon relative to a fixed F_L). Nevertheless, until recently there have been little data on F_L, and these have been at high x (where there are likely to be important higher twist effects) and have very large errors. The situation is now beginning to change. The HERA experiments measure the differential cross section at $y > 0.5$, and are thus sensitive to the component due to F_L. Also, the NMCollaboration have direct measurements of F_L for $0.1 \gtrsim x \gtrsim 0.01$, obtained by data runs for different beam energies, and hence different values of y.

The only consistent way in which to analyse the HERA data at large y is to calculate both the NLO expressions for F_2 and F_L (i.e. using the $\mathcal{O}(\alpha_S^2)$ coefficient functions for F_L [31, 32], where those for heavy quarks use the prescription of [46]) and to compare (13) with the measured $\tilde{\sigma}$. Of course, this is equivalent to the correction of the extracted values of $F_2(x,Q^2)$ to take account of the predicted values of $F_L(x,Q^2)$, and it is this latter procedure that we employ when fitting to the HERA data. (This results in corrections of at most $2-3\%$ to the values of $F_2(x,Q^2)$ quoted in [1, 2].) Since in the published data the value of y is nearly always < 0.6, there is relatively little sensitivity to the value of F_L. However, the H1 collaboration have also published a number of measurements of $\tilde{\sigma}$ for $y = 0.7$ [33], and in the preliminary 1996 data have reproduced these measurements, and also produced measurements at $y = 0.82$ [26]. In Fig. 15 we show a comparison of the prediction for $\tilde{\sigma}(x,Q^2)$ obtained from the MRST partons with this preliminary H1 data. It is clear that the $y = 0.82$ points (the first data point in each plot) lie below the theoretical curves in general (which implies that the predicted F_L is too small). However, it is also clear that the points for $0.01 \gtrsim x \gtrsim 0.001$ tend to lie above the curve. Indeed, the curves in Fig. 15 resemble the curves in Fig. 13: there is a tendency for $\partial F_2(x,Q^2)/\partial \ln Q^2$ to be too small at $x \sim 0.005$ and hence $F_2(x,Q^2)$ tends to be too small at high Q^2, and at $x \sim 0.0005$ there is a tendency for $\partial F_2(x,Q^2)/\partial \ln Q^2$ to be too large and hence $F_2(x,Q^2)$ tends to be too large at high Q^2. Thus, also bearing in mind the large errors on the points at $y = 0.82$, we feel that it is premature to claim any inconsistency in the NLO prediction for $F_L(x,Q^2)$.[11] Alternative theoretical treatments to ours, in particular the inclusion of leading $\ln(1/x)$ terms, lead to different predictions for F_L for similar fits to F_2, and measurements at high y are therefore an important test of such approaches.[12] However, direct measurements of F_L would provide an even better test. We exhibit the predictions for F_L in the HERA kinematic range obtained using the MRST partons in Fig. 16.

In Fig. 17 we compare our predictions for $F_L(x,Q^2)$, made using the partons resulting from each of the three parton sets, MRST, MRST($g\uparrow$) and MRST($g\downarrow$), with the direct measurements made by NMC[13]. There is little variation in the predictions, and each provides a

[11] We note that in the NLO fit performed by H1 there is no direct constraint on the gluon at large x. From the momentum sum rule this leads to more flexibility for the gluon at small x, and hence the details of their best fit are rather different from ours in this region.

[12] For a discussion of such tests, and in particular a demonstration that the high y data gives strong evidence against the validity of a LO-in-α_S fit, see [34].

perfectly satisfactory description of the data. Hence, the NLO calculation of structure functions seems to be compatible with both direct and indirect data on F_L.

3.2 Sensitivity to cuts on the data fitted

Given that there are potentially important higher twist and $\ln(1/x)$ contributions at small Q^2 and/or small x it is instructive to explore the sensitivity of our fits to the minimum Q^2 and/or x cuts. Recall that our minimum Q^2 cut is at $Q_1^2 = 2$ GeV^2, except for the HERA data where the cut is at 1.5 GeV^2. We have imposed no minimum cut on x. We have made repeated global analyses with different minimum Q^2 cuts up to a value $Q_1^2 = 10$ GeV^2. Note that increasing Q_1^2 has the effect of removing much of the lowest x data from the fit. The dashed curve in Fig. 13 shows the effect on $\partial F_2/\partial \ln Q^2$ when the cut is increased to $Q_1^2 = 10$ GeV^2. Not surprisingly the description of the slope determined from the HERA data with $Q^2 \gtrsim 10$ GeV^2 is much improved. We should note that with $Q_1^2 = 10$ GeV^2 a significant fraction of the NMC data is also excluded, see Fig. 7. This removes a strong constraint on the behaviour of the gluon at intermediate x thus allowing the gluon to increase at small x, which improves the fit to the HERA data. As we can see from Fig. 18 the gluon obtained from the $Q_1^2 = 10$ GeV^2 fit is larger at small x than the standard MRST gluon. As expected the difference between the gluons decreases rapidly with increasing Q^2. The effect of an intermediate choice of Q_1^2 can be anticipated by interpolating the $Q_1^2 = 2$ and $Q_1^2 = 10$ GeV^2 results.

Fig. 19 shows the sensitivity of the parton distributions at $Q^2 = 10$ GeV^2 to the minimum Q^2 cut on the structure function data that are included in the fit. Recall that only data with $Q^2 > Q_1^2$ are included. Fig 19 compares the results of analyses with cuts at $Q_1^2 = 5$ and $Q_1^2 = 10$ GeV^2 to our default MRST set obtained by taking the cut at $Q_1^2 = 2$ GeV^2. The plot is interesting because the variation of the values of the partons with the Q_1^2 cut reflects the interplay of the constraints imposed by the various data sets. For instance the u and d quarks for $0.01 \lesssim x \lesssim 0.5$ are stable to a choice of Q_1^2 in the range 2–10 GeV^2, since precise data remain in this domain even for the highest Q_1^2 cut. For the higher Q_1^2 values the small enhancement (up to at most 2%) in the u distribution in the region $0.01 \lesssim x \lesssim 0.1$ can be understood by looking at the description of the highest Q^2 NMC F_2^p data points in this x range, see Fig. 7. The variation of the gluon with Q_1^2 has been discussed above, and is responsible for the similar variation of the charm distribution. The decrease of the light quarks at small x ($x <$ few $\times 10^{-3}$) with increasing Q_1^2 is partly due to compensation for the increase of the charm contribution to F_2^p and partly due to the decrease of F_2^p itself induced by the larger slope $\partial F_2/\partial \ln Q^2$ required by the higher Q^2 data.

We have also repeated the global analysis with various x cuts on the data up to $x_{\rm min} = 0.01$. This removes more than half of the HERA data, but leaves the NMC and other fixed target data virtually untouched. The removal of the constraint on the gluon at very small x allows a larger gluon in the region $x \sim 0.1$, leading to an improvement in the description of the NMC data illustrated in Fig. 14. Nevertheless, as can be seen, the improvement is not as great as might be expected.

3.3 Sensitivity to α_S

We have mentioned that $\alpha_S(M_Z^2) = 0.1175$ yields the optimum χ^2 of the global fit to the combined data sets. Next we explore the sensitivity to the variation of the value of α_S. To do this we perform global analyses with fixed values of α_S in the range ± 0.005 of our optimum value. In each case we use $\langle k_T \rangle = 0.4$ GeV when analysing the WA70 data, which corresponds to the central gluon distribution of the three 'gluon' fits described in the previous section. The contributions to the total χ^2 coming from the various data sets are plotted as a function of α_S in Fig. 20. We emphasize that this is not the optimum χ^2 for a particular data set fitted on its own, but is the contribution to χ^2 for the global fit which, of necessity, has to make compromises between the descriptions of the various data sets. As expected from our previous discussion, we see the opposite trend for the χ^2 of the BCDMS data (which favour a smaller α_S) and the CCFR data (which favour a larger α_S). Similarly the NMC data favour a larger α_S to compensate for the global fit yielding a smaller gluon than that which would be obtained by fitting to the data set on its own. It is noticeable that the recent, more precise, HERA data give a contribution to χ^2 which is less sensitive to variation in α_S than the earlier HERA measurements (see ref. [35]). In summary we see that the overall minimum value $\alpha_S(M_Z^2) = 0.1175$ in the *global fit* is a pinch between the BCDMS and HERA data favouring smaller α_S values and the NMC, SLAC and CCFR data favouring larger values.

An independent sensitive measure of the value of α_S is the single jet inclusive E_T distribution measured in the Fermilab $p\bar{p}$ experiments [36, 37]. We shall see in Section 9 that these data favour values of $\alpha_S(M_Z^2)$ in the region 0.115–0.118. There thus seems to be general agreement that the value of $\alpha_S(M_Z^2)$ is in the region of our optimal value 0.1175 with a spread of about ± 0.0025. It is useful to have a range of parton sets available for different values of α_S, so we present four additional sets which cover a conservative range of ± 0.005 about our optimal value. We denote these by MRST($\alpha_S \downarrow\downarrow$), MRST($\alpha_S \downarrow$), MRST($\alpha_S \uparrow$) and MRST($\alpha_S \uparrow\uparrow$) corresponding to $\alpha_S(M_Z^2) = 0.1125$, 0.1150, 0.1200 and 0.1225 respectively.

Given the recent interest in the very high Q^2 region at HERA it is important to quantify the uncertainty in the extrapolation of F_2^p to high Q^2 at a large value of x. In this x region the main effect comes from the uncertainty in the value of α_S in the DGLAP evolution of F_2^p. The effect is illustrated at $x = 0.45$ in Fig. 21, which shows the spread in the extrapolated values of F_2^p arising from α_S varying across the interval 0.1175 ± 0.005.

4. Prompt photon production and the gluon at large x

In previous MRS parton analyses the WA70 data for $pp \to \gamma X$ [9] have been a key constraint on the gluon distribution for $x \sim 0.3$–0.5. In these analyses we have not included any initial state partonic transverse momenta, that is we have taken $\langle k_T \rangle = 0$, in fitting to the prompt photon data. If we continue to fit the WA70 photon p_T spectrum in this way then the global analysis yields the set of partons that we have called MRST($g \uparrow$) in Table I. We use the $\overline{\rm MS}$ renormalization and factorization prescriptions, with a common scale $Q = p_T/2$. We perform

a full NLO calculation including the effects of fragmentation [38][13]. A good description of the WA70 data is achieved.

However, there is now compelling evidence for the need to include non-zero transverse momentum k_T of the incoming partons (arising from parton multigluon emission[14] and from non-perturbative 'intrinsic' partonic transverse momentum). The reason is apparent if we consider all the data for prompt photon production in high energy pp and $p\bar{p}$ collisions simultaneously. Collectively these data span the entire interval $0.1 \lesssim x \lesssim 0.5$. A major experimental challenge in these experiments is to cleanly extract the prompt photon signal from the copious background of π^0 and η decays. There is a pattern of deviation between theory and experiment in the shape of the photon p_T spectrum. The data fall off more steeply with increasing p_T than the NLO QCD predictions. Neither changes of scale nor the introduction of fragmentation effects can resolve the discrepancy[15] since the various experiments probe different ranges of $x \simeq x_T \equiv 2p_T/\sqrt{s}$. On the other hand it has been shown [41] that the discrepancy can be removed by a broadening of the initial state parton k_T which increases with the energy $\sqrt{s}$.

The parton k_T effect is found to be least in fitting the data due to WA70 — the lowest energy prompt photon experiment. Moreover these data do not exhibit the p_T shape discrepancy with QCD that is seen in the other experiments [17, 8]. For these reasons we have set $\langle k_T \rangle = 0$ in our previous analyses. However, if we include this type of analysis in our new global fit and use the resulting partons, MRST($g\uparrow$), to predict the high precision E706 prompt photon p_T spectra the description is disastrous. To reconcile our prediction with the E706 data we may fold in a Gaussian k_T spectrum[16] with $\langle k_T \rangle \simeq 1$ GeV, or to be precise $\langle k_T \rangle = 0.87(0.97)$ GeV for data taken at laboratory momentum $p_{\rm lab} = 530(800)$ GeV. As a consequence it can be argued that our $\langle k_T \rangle = 0$ analysis of the WA70 data is inconsistent. We should include $\langle k_T \rangle \neq 0$ in the description of these lower energy data but with a smaller value[17] of $\langle k_T \rangle$ than that needed to describe the E706 data.

We therefore repeat the global analysis but fit to the WA70 data using a Gaussian partonic k_T spectrum with $\langle k_T \rangle = 0.4$ GeV, corresponding to 280 MeV per incoming parton. The description of the WA70 data is shown by the continuous curve in Fig. 22. For comparison the dashed curve shows the unsmeared prediction, which of necessity undershoots the data. The resulting set of partons are labelled simply MRST in Table I, and give an equally good fit to

[13]We thank Werner Vogelsang for performing the relevant calculations.

[14]An estimate of the amount of smearing expected from the perturbative component based on the resummation of leading logs has been made in Ref. [39].

[15]Vogelsang and Vogt [40] have demonstrated that these effects can improve the description of a single prompt photon experiment. However, experiments at different $\sqrt{s}$ reproduce a similar pattern, but in different x intervals.

[16]This is in qualitative agreement with the findings of the E706 collaboration [42], although the detailed prescriptions for the k_T smearing are different. We smear the perturbative QCD distribution by first making an analytic continuation of $(d\sigma/dp_T^2)_{\rm QCD}$ to small p_T ($p_T < 3$ GeV) and then we convolute with a Gaussian form $(1/\pi\sigma)\exp(-k_T^2/\sigma)$ where $\sigma = (4/\pi)\langle k_T \rangle^2$.

[17]The empirical evidence that $\langle k_T \rangle$ increases with $\sqrt{s}$ is supported by a similar effect in Drell-Yan production [43].

those of MRST($g\uparrow$) with $\langle k_T \rangle = 0$. How well are the E706 photon data described by the MRST partons, and in particular by the new gluon which is smaller at $x \sim 0.4$? From the continuous curves in Figs. 23 and 24 we see an excellent description of the $p_{\rm lab} = 530$ (800) GeV E706 data is obtained if we take $\langle k_T \rangle = 0.92$ (1.01) GeV.

We can regard the MRST($g\uparrow$) partons with $\langle k_T \rangle = 0$ as one extremum. Conversely how large can we take $\langle k_T \rangle$ to be to describe the WA70 data and still retain a satisfactory fit? We find that we cannot choose $\langle k_T \rangle$ to be arbitrarily large because not only does the gluon become smaller, but it becomes steeper and eventually the shape of the p_T spectrum is not reproduced. The maximum value of $\langle k_T \rangle$ for which a reasonable fit to the WA70 data can still be found is 0.64 GeV. The parton set corresponding to this upper extremum for $\langle k_T \rangle$ is labelled MRST($g\downarrow$), to indicate that it has the smallest gluon at $x \sim 0.4$. The E706 data are well described by the MRST($g\downarrow$) partons provided we take $\langle k_T \rangle = 0.97$ (1.04) GeV at $p_{\rm lab} = 530$ (800) GeV.

So far we have considered the variation of the partons, and in particular of the gluon, due to the uncertainties in the $\langle k_T \rangle$ smearing. Our preferred set of partons with $\langle k_T \rangle = 0.4$ GeV is MRST. The 'extremum' parton sets with $\langle k_T \rangle = 0$ and 0.64 GeV are labelled MRST($g\uparrow$) and MRST($g\downarrow$) in Table I, with gluons which are respectively larger and smaller than the MRST gluon at $x \sim 0.4$.

There is also a non-negligible dependence on the choice of scale. For instance the effect of changing the scale from $Q = p_T/2$ to $Q = p_T$ is shown in Fig. 23. We see that the unsmeared cross section is decreased by some 30%, which can be compensated by a relatively modest increase in the size of the gluon distribution and/or in $\langle k_T \rangle$. That is the effect of the change of scale is considerably less than the uncertainties associated with smearing. In principle the former can be reduced by a knowledge of the NNLO perturbative contributions, while a reduction in the latter will require a more detailed theoretical understanding of the origin of the partonic transverse momentum.

5. Treatment of Heavy Flavours

Until recently the treatment of heavy quark distributions in MRS and CTEQ global analyses has been rather naive. In previous analyses the charm and bottom quarks were regarded as infinitely massive below a threshold $Q^2 = m_H^2$, and then being treated as massless, and thus evolving according to the normal massless evolution equations above this threshold. Up to NLO in α_S this prescription guarantees that the correct results will be obtained asymptotically, but is clearly rather unsatisfactory near threshold where there should be a smooth threshold at $W^2 = Q^2(1/x - 1) = 4m_H^2$, where W^2 is the invariant mass of the hadronic system, rather than an abrupt threshold in $Q^2 = m_H^2$. Nevertheless, choosing the slightly high value of $m_c^2 = 2.7$ GeV^2, a reasonable match to the EMC data [7] on the charm structure function for $Q^2 > 4$ GeV^2 was obtained[18], and the low contribution due to charm for the total structure

[18] In the MRS global analysis of [25] the charm evolved from the low value of $Q^2 = 1$ GeV^2 but was suppressed by a phenomenological damping factor.

function rendered a more complete treatment of heavy quark contributions unnecessary in this x and Q^2 range.

An alternative procedure to that outlined above is where all charm is regarded as being produced from the hard scatter between the electroweak boson and a light parton, i.e. the number of active flavours, n_f, is 3 and the charm cross section is generated (mainly) by photon-gluon fusion (PGF). This corresponds to the so-called fixed flavour number scheme (FFNS) and it incorporates the correct threshold behaviour automatically. For example, at order $\mathcal{O}(\alpha_S)$ the charm structure function is given by

$$F_2^c(x,Q^2,m_c^2) \;=\; \frac{\alpha_S(\mu^2)}{2\pi}\, C_g^{(1)\,\mathrm{FF}}(Q^2/m_c^2) \;\otimes\; g_{n_f=3}(\mu^2), \tag{15}$$

where the coefficient function (CF), which is convoluted with LO evolved gluon density $g_{n_f=3}$, is

$$\begin{aligned} C_g^{(1)\,\mathrm{FF}}(z,Q^2/m_c^2) \;&=\; \Big[(P_{qg}^0(z) + 4\frac{m_c^2}{Q^2}z(1-3z) - 8\Big(\frac{m_c^2}{Q^2}\Big)^2 z^2)\, \ln\Big(\frac{1+v}{1-v}\Big) \\ &+\; (8z(1-z) - 1 - 4\frac{m_c^2}{Q^2}z(1-z))v\Big]\, \theta(\hat{W}^2 - 4m_c^2) \end{aligned} \tag{16}$$

where $\hat{W}^2 = Q^2(1/z-1)$ is the gluon quark centre of mass energy, v is the velocity of the charm quark or antiquark in the photon–gluon centre–of–mass frame, defined by $v^2 = 1 - 4m_c^2/\hat{W}^2$, and $P_{qg}^0(z) = z^2 + (1-z)^2$, the LO quark-gluon splitting function. These v–dependent terms ensure that the coefficient function tends to zero smoothly as $\hat{W}^2 = 4m_c^2$ is approached from below, and hence the structure function has a smooth threshold in W^2. This method does not sum potentially large logarithms in Q^2/m_c^2, and thus is unsuitable for $Q^2 \gg m_c^2$, but provides an acceptable description provided Q^2 is not large and one is not interested in the concept of a charm quark density. It is the method used to produce the most recent GRV structure functions [27], and is also used in the analyses by H1 and ZEUS.

However, the more recent measurements of charm production at HERA [5, 6] emphasise the importance of having a consistent theoretical framework for heavy flavour production in deep inelastic scattering. Not only are there more direct measurements of the charm structure function F_2^c, but the charm contribution could be 20% or more of the total F_2 at small x. Indeed, even the NMC data which contains only $5-10\%$ charm, but has rather smaller errors than the HERA data, is sensitive to the treatment of charm. Hence, a modern global analysis of structure functions must necessarily include a satisfactory description of F_2^c.

As a consequence there have been several recent theoretical studies [44, 45, 46] to improve the treatment of heavy quark mass effects in deep inelastic scattering. For instance ref. [45] proposes a simple procedure to sum up the leading (and next-to-leading) log contributions of Feynman diagrams including explicitly the $m_H \neq 0$ mass effects. It is straightforward to generalize this procedure to any order. In this approach the natural scale to resolve charm quarks in the proton is $Q^2 = (m_c^2 + k_T^2)/(z(1-z)) \gtrsim 4m_c^2$, whereas the conventional $\overline{\mathrm{MS}}$ scheme, which we

adopt, requires the charm threshold to be at $Q^2 = m_c^2$. (k_T and z define the momentum of the charm quark). For this reason the procedure is difficult to reconcile with the $\overline{\rm MS}$ scheme.

5.1. Theoretical procedure

In order to have a reliable treatment of massive quarks over the whole range of Q^2 we must clearly use an approach which extrapolates smoothly from the FFNS at low Q^2 to the massless evolution at high Q^2, maintaining the correct ordering in both schemes. To do this we use a method which has recently been developed by two of the authors and is discussed in detail in [46], and more briefly in [47]. Since this treatment of charm is such a major change to our previous analyses we present the method briefly here. First we note that in the FFNS (15) is valid up to corrections of $\mathcal{O}(\Lambda^2/m_c^2)$ while the massless prescription is valid only up to corrections of $\mathcal{O}(m_c^2/\mu^2)$, i.e. threshold corrections. In order to improve the accuracy of the latter scheme we need to examine the connection between the parton densities in the two schemes. The connection between the $\overline{\rm MS}$ parton densities for 3 and 4 flavours takes the form

$$\begin{aligned} c_+(z,\mu^2,\mu^2/m_c^2) &= A^{cg}(\mu^2/m_c^2) \otimes g_{n_f=3}(\mu^2) \\ g_{n_f=4}(z,\mu^2,\mu^2/m_c^2) &= A^{gg}(\mu^2/m_c^2) \otimes g_{n_f=3}(\mu^2) \end{aligned} \tag{17}$$

at leading order, where the elements A^{ba} which contain $\ln(\mu^2/m_c^2)$ terms, are, in general, part of a full 5×4 matrix which also connects the light quark flavours. Hence the charm distribution $c_+ \equiv c + \bar{c}$ is determined entirely in terms of the light parton distributions, and it is the above equations which lead to the requirement of evolving from zero charm at $\mu^2 = m_c^2$. Since we use the scale choice $\mu^2 = Q^2$ for all the light partons we also take this simple choice for the heavy quark structure function. Thus, from now on we will always use Q^2 instead of μ^2.

For $Q^2 \gg m_c^2$, the equivalence of the FFNS and the massless scheme at all orders lead to the connections between the CF's in the two schemes up to $\mathcal{O}(m_c^2/Q^2)$ [48], in particular up to $\mathcal{O}(\alpha_S^2)$

$$\begin{aligned} C_g^{\rm FF}(z,Q^2/m_c^2) &= C_c^{n_f=4} \otimes A^{cg}(Q^2/m_c^2) \\ &\quad + C_g^{n_f=4} \otimes A^{gg}(Q^2/m_c^2) + \mathcal{O}(m_c^2/Q^2). \end{aligned} \tag{18}$$

The details of the connection are fully worked out in [48]. To improve the accuracy of (18), where the uncertainty is reduced to $\mathcal{O}(\Lambda^2/m_c^2)$, requires defining 'corrected' CF's, $C_i^{\rm VF}$ $(i = 1,\ldots,4)$, in another $n_f = 4$ scheme – the variable flavour number scheme (VFNS) – where one can write

$$\begin{aligned} F_2^c(x,Q^2,m_c^2) &= C_c^{\rm VF}(Q^2/m_c^2) \otimes c_+(Q^2,Q^2/m_c^2) \\ &\quad + C_g^{\rm VF}(Q^2/m_c^2) \otimes g_{n_f=4}(Q^2,Q^2/m_c^2) + \mathcal{O}(\Lambda^2/m_c^2), \end{aligned} \tag{19}$$

where the corrected CF's are related to the FFNS CF's by

$$C_i^{\rm FF}(z,Q^2/m_c^2) = C_j^{\rm VF}(Q^2/m_c^2) \otimes A^{ji}(Q^2/m_c^2), \tag{20}$$

the new n_f=4 CF's now being *exact* at all values of Q^2.

Hence, our procedure is to use the FFNS for $Q^2 \leq m_c^2$ where it should be very reliable and switch to the VFNS for $Q^2 \geq m_c^2$. (The precise choice of the transition point is undetermined, however, taking $Q^2 = m_c^2$ removes complications arising from $\ln(Q^2/m_c^2)$ terms in the matching conditions between the partons at threshold.) In order to define the VFNS one must solve (20) for the $C_i^{\rm VF}$. Unfortunately the all-orders matching of F_2^c in the two schemes, from which (20) arose, is not sufficient since, for example, at low orders the *single* quantity $C_g^{\rm FF}$ is expressed in terms of the *two* quantities $C_c^{\rm VF}$ and $C_g^{\rm VF}$. We stress that any choice satisfying (20) is 'correct' in the sense that it leads to the same all orders expression. Nevertheless, each choice leads to a different expression if one uses the usual rules of combining coefficient functions and parton distributions of a given order to obtain a fixed order in α_S expression for the structure functions. In order to remove this ambiguity we apply a sensible, physically motivated constraint and impose not only continuity of the structure function but also demand, in addition, order-by-order matching of the evolution of F_2^c at threshold.

The explicit form of (17) at $\mathcal{O}(\alpha_S)$ is

$$\begin{aligned} c_+(z,Q^2,Q^2/m_c^2) &= \frac{\alpha_S}{2\pi}\,\ln\!\left(\frac{Q^2}{m_c^2}\right) P_{qg}^0 \otimes g_{n_f=3} \\ g_{n_f=4}(z,Q^2,Q^2/m_c^2) &= g_{n_f=3}(z,Q^2) - \frac{\alpha_S}{6\pi}\,\ln\!\left(\frac{Q^2}{m_c^2}\right) g_{n_f=3}. \end{aligned} \tag{21}$$

Inserting the implied expressions for the matrix elements $A^{cg}(z,Q^2/m_c^2)$ and $A^{gg}(z,Q^2/m_c^2)$ into (18) gives the relation (first seen in [44])

$$C_g^{(1)\,\rm FF}(z,Q^2/m_c^2) = C_g^{(1)\,\rm VF}(z,Q^2/m_c^2) + C_c^{(0)\,\rm VF}(Q^2/m_c^2) \otimes P_{qg}^0\,\ln\!\left(\frac{Q^2}{m_c^2}\right) \tag{22}$$

connecting the gluonic CF's in the FFNS and VFNS. Let us now consider the evolution of F_2^c. From (15) the LO expression in the FFNS for the $\ln Q^2$ derivative is simply

$$\frac{dF_2^c(x,Q^2,m_c^2)}{d\ln Q^2} = \frac{\alpha_S}{2\pi}\,\frac{dC_g^{(1)\,\rm FF}(Q^2/m_c^2)}{d\ln Q^2} \otimes g_{n_f=3}(Q^2). \tag{23}$$

The corresponding expression obtained by differentiating the LO expression in the VFNS, for Q^2 just above m_c^2, is

$$\begin{aligned} \frac{dF_2^c(x,Q^2,m_c^2)}{d\ln Q^2} &= \frac{dC_c^{(0)\,\rm VF}(Q^2/m_c^2)}{d\ln Q^2} \otimes c_+(Q^2) \\ &+ \frac{\alpha_S}{2\pi}\,C_c^{(0)\,\rm VF}(Q^2/m_c^2) \otimes \Big(P_{qg}^0 \otimes g_{n_f=4}(Q^2) + P_{qq}^0 \otimes c_+(Q^2)\Big). \end{aligned} \tag{24}$$

At $Q^2 = m_c^2$, the terms in (24) involving c_+ vanish because of (21) and so demanding continuity of the evolution across the transition point immediately leads, from (23,24), to

$$C_c^{(0)\,\rm VF}(Q^2/m_c^2) \otimes P_{qg}^0 = \frac{dC_g^{(1)\,\rm FF}(z,Q^2/m_c^2)}{d\ln Q^2}. \tag{25}$$

Generalising this relation to be the definition of $C_c^{(0)\,\mathrm{VF}}(z, Q^2/m_c^2)$ at *all* Q^2 guarantees a smooth passage for charm structure function from $Q^2 < m_c^2$ to $Q^2 > m_c^2$, by definition. It is also easy to see that in the limit $Q^2 \to \infty$,

$$\frac{dC_g^{(1)\,\mathrm{FF}}(z, Q^2/m_c^2)}{d\ln Q^2} \to P_{qg}^0(z). \tag{26}$$

Hence, from (25), we see that $C_c^{(0)\,\mathrm{VF}}(z, Q^2/m_c^2)$ must indeed tend to the usual simple form $z\,\delta(1-z)$ in this limit. Also, since $C_g^{(1)\,\mathrm{FF}}(z, Q^2/m_c^2)$ contains the factor $\theta(\hat{W}^2 - 4m_c^2)$ so does its $\ln Q^2$ derivative, thus ensuring the correct threshold behaviour in W^2 for $C_c^{(0)\,\mathrm{VF}}$ and in turn for F_2^c at LO. Furthermore (25) allows the gluonic CF in the VFNS to be written as

$$C_g^{(1)\,\mathrm{VF}}(z, Q^2/m_c^2) = C_g^{(1)\,\mathrm{FF}}(z, Q^2/m_c^2) \; - \; \frac{dC_g^{(1)\,\mathrm{FF}}(z, Q^2/m_c^2)}{d\ln Q^2} \; \ln\!\left(\frac{Q^2}{m_c^2}\right), \tag{27}$$

and $C_g^{(1)\,\mathrm{VF}}$ also has the correct threshold behaviour as $Q^2/m_c^2 \to \infty$ and $C_g^{(1)\,\mathrm{VF}}(z, Q^2/m_c^2)$ tends to the correct asymptotic $\overline{\mathrm{MS}}$ limit. The extension of this procedure to any arbitrary order, i.e. continuity of the derivative in the gluon sector, is described in full in [46].

The implementation of the charm coefficient function is also described in detail in [46], and results in the relatively straightforward expression

$$\begin{aligned} C_c^{(0)\,\mathrm{FF}}(Q^2/m_c^2) \otimes c_+(Q^2) \;\; &= \;\; -\int_x^{x_0} dz\, \frac{dC_g^{(1)\,\mathrm{FF}}(z, Q^2/m_c^2)}{d\ln Q^2} \left(\frac{x}{z}\right)^2 \frac{dc_+(x/z, Q^2)}{d(x/z)} \\ &+ \;\; 3\int_x^{x_0} dx\, \frac{dC_g^{(1)\,\mathrm{FF}}(z, Q^2/m_c^2)}{d\ln Q^2}\, \frac{x}{z}\, c_+(x/z, Q^2) \\ &- \;\; 2\int_x^{x_0} dz\, \frac{dC_g^{(1)\,\mathrm{FF}}(z, Q^2/m_c^2)}{d\ln Q^2} \int_{x/z}^1 dz'\, r(z')\, \frac{x}{zz'}\, c_+(x/zz', Q^2) \end{aligned} \tag{28}$$

where $x_0 = (1 + 4m_c^2/Q^2)^{-1}$ and $r(z)$ is given by

$$r(z) = z^{\frac{1}{2}}\left[\cos\!\left(\frac{\sqrt{7}}{2}\ln\frac{1}{z}\right) + \frac{3}{\sqrt{7}}\sin\!\left(\frac{\sqrt{7}}{2}\ln\frac{1}{z}\right)\right]. \tag{29}$$

This general method can be applies at all orders, and the $\mathcal{O}(\alpha_S)$ charm coefficient function is determined by demanding continuity of $dF_2^c(x, Q^2, m_c^2)/d\ln Q^2$ (in the gluon sector) at $\mathcal{O}(\alpha_S^2)$, and is discussed in detail in [46]. However, in practice its contribution to the charm structure function is only at the level of a couple of percent at most, and it can be treated using a phenomenological approximate expression.

Thus we can calculate the charm structure function at NLO. For $Q^2 < m_c^2$ we use the usual FFNS expression, i.e. using coefficient functions [32] to $\mathcal{O}(\alpha_S^2)$[19] and parton distributions with

[19] We are grateful to Steve Riemersma and Jack Smith for providing the program to compute the $\mathcal{O}(\alpha_S^2)$ contributions.

3 light quarks. For $Q^2 > m_c^2$ we use the VFNS coefficient functions to $\mathcal{O}(\alpha_S)$ and the partons are evolved via the NLO DGLAP equations in $\overline{\rm MS}$ scheme with 4 massless quarks. Since the coefficient functions reduce to the usual massless expressions as $Q^2/m_c^2 \to \infty$, the structure functions approach the previous massless expressions in this limit.

We feel we should distinguish between this approach and previous implementations of a VFNS. In [44] (22) served as the definition for $C_g^{(1)\,\rm VF}$ in terms of the PGF CF (16) with an assumed form of $C_c^{(0)\,\rm VF}$ given by

$$\hat{C}_c^{(0)\,\rm VF}(z, Q^2/m_c^2) = z\,\delta(\hat{x}_0 - z)\Big(1 + \frac{4m_c^2}{Q^2}\Big), \qquad \hat{x}_0 = \Big(1 + \frac{m_c^2}{Q^2}\Big)^{-1} \tag{30}$$

where the delta-function describes the tree-level diagram for a massive quark scattering from a photon and the modified argument of the delta-function follows from demanding that the massive quark is on-shell.[20] We believe that this manner of determining the charm coefficient function does not reflect the true physics, i.e. that a real charm-anticharm pair must be generated via the photon scattering, leading to the physical threshold in W^2, and cancellation between terms is required to reflect this correct threshold. A full critique of this approach can be found in [46], but we note here that our variable flavour number scheme is certainly very different to this alternative prescription (which is not yet implemented in their definition of NLO).

The theoretical treatment of the bottom quark is essentially identical to that for the charm quark outlined above, and we use the FFNS below $Q^2 = m_b^2$ and the VFNS above $Q^2 = m_b^2$. As discussed in [46], the procedure also generalizes to other processes in a simple manner.

5.2 Implications for F_2^c and the global analysis

In Fig. 25 we show the result of the NLO calculation of F_2^c for $x = 0.05$. The very smooth transition from the description at low Q^2 in terms of the FFNS to high Q^2 in terms of the massless prescription demonstrates the success of our procedure. The result is qualitatively similar for all other x values. However, the obvious discrepancy between the continuation of the FFNS curve and the zero-mass curve for relatively low Q^2 (i.e. $\sim 5{-}20$ GeV^2), diminishes as we go to lower x as we are then further from the physical threshold in W^2, and mass-dependent effects become less important.

As was demonstrated in [46], the global fit to structure function data achieved using our prescription for charm was superior to that using either the FFNS or the massless prescription. The former has too slow an evolution due to the lack of $\ln(Q^2/m_c^2)$ terms, and the latter gives a definite kink in $F_2(x, Q^2)$ at mass thresholds. Thus our global fit incorporates the best available treatment of heavy quark mass effects using NLO-in-α_S QCD.

One point to note is the influence of the charm prescription on the optimum value of $\alpha_S(M_Z^2)$. In the most recent global analysis this value came out to be 0.113, although an alternative set

[20] We note that the same definition of the zeroth order coefficient function is adopted in [45], although of course there are differences between this and [44], notably the mass dependent evolution in the former.

of partons was also given for $\alpha_S(M_Z^2) = 0.120$ [25]. The fact that the value of $\alpha_S(M_Z^2)$ for the best fit has risen to 0.1175 is partially due to some of the new data in this fit, e.g. the reanalysed CCFR data, and the final NMC data. However, a fit to the new data using the old massless charm prescription results in a value of $\alpha_S(M_Z^2) = 0.116$. Hence, the effect of the new treatment of heavy quarks is to increase the value of $\alpha_S(M_Z^2)$ by about 0.002. We also note that the prediction for $F_L(x, Q^2)$ is very different to previous analyses, i.e. smaller; the charm contribution being very suppressed near threshold since the gluon coefficient function behaves like v^3. This leads to a better description of the NMC data on R [13], as seen in Fig. 17.

We can also look at the charm structure function directly. In Fig. 26 we show the comparison of the charm structure function $F_2^c(x, Q^2)$ resulting from the MRST partons with all available data. The data at intermediate x values come from EMC [7] measurements of inclusive muons, while the new data from HERA are obtained by measuring D and D^* cross sections [5, 6]. We show MRST curves together with those resulting from the MRST($g\uparrow$) and MRST($g\downarrow$) parton sets. In all cases the value of m_c is taken to be 1.35 GeV. (A comparison for different values of m_c can be found in [46].) The predictions using the central gluon agree well with the data. As we would expect the difference between the predictions is only significant for relatively high x. However, we see that for the two highest x bins the curves for MRST($g\downarrow$) tend to fall below the data. Thus, the EMC charm data are capable of acting as a weak constraint on the form of the gluon at high x, and it is clear that any parametrization which has an even smaller gluon at high x than MRST($g\downarrow$) would be inconsistent with these charm data.

We should also justify our choice of $m_c = 1.35$ GeV. This value is chosen somewhat as a compromise. As shown in [46] the charm data on their own prefer a value in the region of 1.5 GeV. However, the quality of the *global* fits obtained are slightly sensitive to the value of m_c and we find that $m_c \sim 1.2$ GeV, or even lower, actually gives the best fit. Practically all this sensitivity to m_c comes from the NMC F_2 data with $x < 0.1$. As already discussed, these data grow with Q^2 more quickly than the theory predicts. If m_c is lowered then the charm evolution is slowed down less by mass effects, and the slopes of the theory curves increase. This is seen clearly in Figs. 7 and 14 which demonstrate the improvement in the description, although it is clear that a problem remains. As already mentioned there are other effects which could be responsible for the apparent discrepancy with the observed value of $dF_2/d\ln Q^2$ in this region, and hence we do not take this as strong evidence for a low value of m_c. Indeed, as seen in [46], the F_2^c data themselves completely rule out such a low value of m_c. Hence we choose $m_c = 1.35$ GeV as a compromise between the values required by the best global fit and the best description of charm data.

Of course there are as yet no data on the bottom quark contribution to the structure function, and because it contributes with a charge squared of 1/9, and only at relatively high Q^2, it forms only a very small fraction of the total structure function. Hence, the value of m_b has essentially no impact on the quality of the fit, and is always taken to be 4.3 GeV. Future data on the bottom structure function could act both as a verification of our treatment of heavy flavours and as a determination of the bottom quark mass. The b quark distribution at $Q^2 = 10^4$ GeV

is shown in Fig. 4.

6. Drell-Yan production

The observation of Drell-Yan production in high energy pN collisions offers a valuable constraint on the sea quark distributions since the leading-order subprocess is $q\bar{q} \to \gamma^* \to \ell^+\ell^-$. The small x_F data of the E605 collaboration [15] are used in the global analysis and they constrain the sea in the interval $0.15 \lesssim x \lesssim 0.4$. The description of the E605 data is shown in Fig. 27. The curves are obtained using NLO QCD, with the factorization and renormalization scales set equal to the invariant mass M of the lepton pair, together with an overall phenomenological normalization parameter which allows for possible higher-order effects.

The more recent measurements of the E772 collaboration [14] span a larger kinematic range and, in principle, allow the sea quark distribution to be probed down to $x \simeq 0.025$. In general the agreement between the data and the MRST prediction is quite satisfactory, see Fig. 28. However, we point out a discrepancy at high x_F and low $\sqrt{\tau}$. In this region the dominant contribution is

$$d\sigma \simeq u(x_1)\left[\bar{u}(x_2) + \bar{d}(x_2)\right] \tag{31}$$

where $x_1 \simeq x_F$ and $x_2 \simeq \tau/x_1$, and where the partons are sampled at scales $Q^2 = M^2 = s\tau$ with $\sqrt{s} \simeq 40$ GeV. If we assume that $u(x_1)$ is known, then there is a factor of two discrepancy between the E772 data and $(\bar{u} + \bar{d})$ evaluated at $x_2 \sim 0.03$. We find that there is no way in which the global fit can remove this discrepancy since, at such small x values, $(\bar{u} + \bar{d})$ gives approximately a third of the total contribution to F_2, and so is well determined by the deep inelastic scattering data..

7. Flavour decomposition of the sea

As seen in Figs. 3 and 4 the sea quark distributions ($\bar{u}, \bar{d}, \bar{s}, \bar{c}$ and $\bar{b}$) have an interesting non-trivial structure. Of course, as Q^2 increases, all these distributions ultimately evolve to a common form, concentrated at small values of x, since they are driven by $g \to q\bar{q}$ transitions. However, at accessible Q^2 values the different flavour sea quark distributions are quite distinct. Due to their heavy mass, the $\bar{c}$ and $\bar{b}$ can be treated perturbatively, as discussed in Section 5. The x and Q^2 dependence of these heavy quark densities are therefore completely determined, with their mass being the only free parameter. On the other hand for the light quark distributions, $\bar{u}, \bar{d}$ and $\bar{s}$, we may use massless evolution, but here the distributions at the starting scale have a non-perturbative origin and are determined by experiment. For the light quark distributions we use the parametric forms given in (3), (5)–(8).

7.1 The strange quark distribution

The observations of deep inelastic dimuon production indicate that $\bar{s}$ has the same x shape as $(\bar{u} + \bar{d})$ but with an overall suppression of the order of 50% at $Q^2 \simeq 4$ GeV^2, presumably due to the mass of the strange quark. We reflect this behaviour by using an $\bar{s}$ parametrization

which has the same shape as $(\bar{u}+\bar{d})$ at Q_0^2, but with a single overall parameter (0.2 in (7)) which is adjusted to fit to the CCFR dimuon data [16]. Fig. 29 shows the MRST strange quark distribution compared to the measurements determined by the CCFR collaboration in a NLO analysis [16] of their dimuon production data. We see that our minimal parametrization gives excellent agreement with their experimental result, which supports the assumption that $\bar{s}/(\bar{u}+\bar{d})$ is essentially independent of x. As noted earlier, at small x, the differences between $\bar{u}, \bar{d}$ and $\bar{s}$ decrease with increasing Q^2, due to the dominance of the $g \to q\overline{q}$ subprocesses. Finally we note that an independent measurement of $\bar{s}$ could, in principle, be made at HERA using the charged current subprocess $e^- + \bar{s} \to \nu + (\bar{c} \to \mu^-)$ provided that the accelerator integrated luminosity was sufficiently high.

7.2 Determination of the difference $\bar{u} - \bar{d}$

The structure function measurements (of $F_2^{\mu p}, F_2^{\mu n}, F_2^{\nu N}$ and $xF_3^{\nu N}$) determine $(\bar{u}+\bar{d})$, but not $(\bar{u}-\bar{d})$. The sum rules do give some information on the integral over $\bar{u}-\bar{d}$, which indicate that, on average, $\bar{d}$ is greater than $\bar{u}$.

For a direct determination of $\bar{u}-\bar{d}$ we must look elsewhere. One proposal [49] is to measure the asymmetry of Drell-Yan production in pp and pn collisions

$$A_{\rm DY} \equiv \frac{\sigma_{pp}-\sigma_{pn}}{\sigma_{pp}+\sigma_{pn}} = \frac{1-r}{1+r}, \tag{32}$$

where $r = \sigma_{pn}/\sigma_{pp}$ and where $\sigma \equiv d^2\sigma/dMdx_F$ with M and x_F being the invariant mass and the Feynman x of the produced lepton pair. At leading order we have

$$r \equiv \frac{\sigma_{pn}}{\sigma_{pp}} = \frac{(4u_1\bar{d}_2 + d_1\bar{u}_2 + 4\bar{u}_1 d_2 + \bar{d}_1 u_2 + 2s_1 s_2 + 8c_1 c_2)}{(4u_1\bar{u}_2 + d_1\bar{d}_2 + 4\bar{u}_1 u_2 + \bar{d}_1 d_2 + 2s_1 s_2 + 8c_1 c_2)} \tag{33}$$

where the 1,2 subscripts indicate that the partons are to be evaluated at

$$x_1, x_2 = \frac{1}{2}\left(\pm x_F + \sqrt{x_F^2 + 4\tau}\right), \tag{34}$$

with $\tau = M^2/s$. We may rearrange the expression for $1-r$, and hence that for $A_{\rm DY}$, to show that it is dependent on the combinations $(\bar{u}_1 - \bar{d}_1)$ and $(\bar{u}_2 - \bar{d}_2)$.

The first experiment of this type was performed by the NA51 collaboration [11]. They measured

$$R_{dp} \equiv \frac{\sigma_{pd}}{2\sigma_{pp}} = \frac{1}{2}(1+r) \tag{35}$$

at $x_1 = x_2 = 0.18$ and found $A_{\rm DY} = -0.09 \pm 0.02 \pm 0.025$, which corresponds to $\bar{d}/\bar{u} \simeq 2$. Very recently the E866 collaboration [10] have measured R_{dp} over a much wider range of M and x_F, which enables a study of the x dependence of $(\bar{u}-\bar{d})$ over the range $0.04 < x < 0.3$. The continuous curve in Fig. 30 shows our fit to these data[21]. The dotted curve shows the

[21] We calculate the ratio R_{dp} from the NLO QCD expression for $d^2\sigma/dx_1dx_2$, with x_1 computed from the mean value of x_2 for each bin, and then we join the resulting values of R_{dp} to form a smooth curve.

values which would have been obtained for the ratio if we were to set $\bar{u}$ equal to $\bar{d}$, that is if we were to take $A_\Delta = 0$ in (8). The implications for $\bar{d}/\bar{u}$ from our fit to the E866 data are shown in Fig. 31. Interestingly the structure of $\bar{d}/\bar{u}$ shows that, at the maximum value of x that is measured[22], the ratio has decreased to give $\bar{d} \simeq \bar{u}$. Moreover we see that the NA51 measurement occurs at a value of x for which $\bar{d}/\bar{u}$ is essentially at a maximum. Nevertheless the new data indicate a somewhat smaller value of $\bar{d}/\bar{u}$ at this point, $x = 0.18$. For comparison we also show the prediction for $\bar{d}/\bar{u}$ obtained from the MRS(R2) set of partons [25] — partons which were obtained from a global fit which included the NA51 measurement, but for which the E866 data were not available.

Independent information on the $\bar{u}$,$\bar{d}$ flavour asymmetry is currently being obtained by the HERMES experiment [50] at HERA from the observation of semi-inclusive deep inelastic events. By observing final state $\pi^\pm$ mesons, they measure the ratio

$$r(x,z) = \frac{\sigma(ep \to e\pi^- X) - \sigma(en \to e\pi^- X)}{\sigma(ep \to e\pi^+ X) - \sigma(en \to e\pi^+ X)} \tag{36}$$

where z is the fractional energy of the fragmenting parton that is carried by the pion. The HERMES semi-inclusive data lie in the kinematic range $0.02 < x < 0.3$ and $0.3 < Q^2 < 10$ GeV^2. At leading order $r(x,z)$ is a direct measure of $(\bar{u} - \bar{d})/(u - d)$ since

$$\frac{1 + r(x,z)}{1 - r(x,z)} = \frac{(u-d) + (\bar{u} - \bar{d})}{(u-d) - (\bar{u} - \bar{d})} \frac{3}{5} \left(\frac{1+F}{1-F}\right) \tag{37}$$

where $F(z)$ is the ratio of the disfavoured to favoured $u \to \pi$ fragmentation functions, $F = D_u^{\pi^-}/D_u^{\pi^+}$. Fig. 32 compares[23] the MRST predictions with the preliminary HERMES measurements [50] of $(\bar{d} - \bar{u})/(u - d)$ as a function of x. The good agreement between the MRST curve and this independent measure of $\bar{u} - \bar{d}$ is confirmation that $\bar{d}/\bar{u}$ is now reliably known as a function of x and Q^2 for $x < 0.3$.

Historically the first indication of the $\bar{u} \neq \bar{d}$ flavour asymmetry of the sea came from the evaluation of the Gottfried sum

$$I_{\rm GS} \equiv \int_0^1 \frac{dx}{x} (F_2^{\mu p} - F_2^{\mu n}) \tag{38}$$

by NMC [51]. The final NMC measurements [52] of $(F_2^{\mu p} - F_2^{\mu n})$ are compared with the values obtained from the MRST partons in Fig. 33. The area under the MRST curve yields the value $I_{\rm GS} = 0.266$. This is slightly larger than the value $I_{\rm GS} = 0.235 \pm 0.026$ found at $Q^2 = 4$ GeV^2 by NMC [52]. The small discrepancy is induced in part by the requirement that the MRST partons also fit the E866 data.

[22]Our parametric form should not be extrapolated to predict $\bar{d}/\bar{u}$ at larger values of x, where both $\bar{u}$ and $\bar{d}$ are very small.

[23]Note that we compare NLO MRST partons with a LO ratio extracted from the semi-inclusive data. However the effect of the NLO corrections is expected to largely cancel in the ratio.

8. W rapidity asymmetry

The $W^{\pm}$ charge asymmetry at the Fermilab $p\bar{p}$ collider,

$$A_W(y) \;=\; \frac{d\sigma(W^+)/dy - d\sigma(W^-)/dy}{d\sigma(W^+)/dy + d\sigma(W^-)/dy}, \tag{39}$$

is a sensitive probe of the difference between u and d quarks in the $x \sim 0.1$, $Q \sim M_W$ region. Because the u quarks carry more momentum on average than the d quarks, the W^+ bosons tend to follow the direction of the incoming proton and the W^- bosons that of the antiproton, i.e. $A_W > 0$ for $y > 0$. Thus a precise measurement of the W asymmetry serves as a valuable independent check on the u- and d-quark distributions. In practice it is the lepton asymmetry,

$$A(y_\ell) \;=\; \frac{\sigma(\ell^+) - \sigma(\ell^-)}{\sigma(\ell^+) + \sigma(\ell^-)}, \tag{40}$$

which is measured, where $\sigma(\ell^{\pm}) \equiv d\sigma/dy_\ell$ are the differential $p\bar{p} \to W^{\pm}X \to \ell^{\pm}\nu X$ cross sections for producing $\ell^{\pm}$ leptons of rapidity y_ℓ. There is a direct correlation between the lepton asymmetry and the *slope* of the d/u ratio. To see this we first note that the dominant contribution to $W^+(W^-)$ production comes from the $u\bar{d}$ $(d\bar{u})$ annihilation process. Thus

$$A_W(y) \;\simeq\; \frac{u(x_1)d(x_2) - d(x_1)u(x_2)}{u(x_1)d(x_2) + d(x_1)u(x_2)}, \tag{41}$$

where the scale $Q = M_W$ is implicit for the parton distributions, and

$$x_{1,2} \;=\; x_0 \exp(\pm y), \quad x_0 \;=\; \frac{M_W}{\sqrt{s}}. \tag{42}$$

If we introduce the ratio $R_{du}(x) = d(x)/u(x)$, then, for small y,

$$A_W(y) \;\simeq\; -x_0 y\, \frac{R'_{du}(x_0)}{R_{du}(x_0)}, \tag{43}$$

where the prime denotes differentiation. In reality, the situation is of course more complicated — it is the *lepton* asymmetry which is measured, and there are subleading and higher-order corrections to (41). Nevertheless, the correlation implied by (43) is evident in the full prediction.

The CDF collaboration [12] have recently extended the range and improved the precision of their measurements of the asymmetry A_ℓ. The new data extend to higher values of lepton rapidity y_ℓ and the measured values are below the extrapolation of the previous global fits. The fit[24] to the lepton asymmetry data is shown in Fig. 34. For comparison we also show the result from a previous set of partons, MRS(R2), which were fitted to earlier CDF asymmetry measurements. Recently the effects of soft gluon resummation on A_ℓ have been calculated [54]. They increase the asymmetry slightly at the highest y_ℓ values of the data. For example at the

[24]The curves in Fig. 34 are calculated using the next-to-leading-order program DYRAD of [53]. We thank Nigel Glover for helping with these calculations of the W asymmetry.

highest value, $y_\ell = 2.2$, the increase in A_ℓ is about 0.02 so that the MRST prediction would, as it happens, be raised to coincide exactly with the data point.

In order to accommodate the new A_ℓ measurements the d distribution increases with respect to the u at $x \sim 0.3$ (in comparison with our previous global analysis). The change affects F_2^n much more than F_2^p. The consequence is that the ratio F_2^n/F_2^p is increased, and the description of the new NMC data is improved relative to MRS(R2), see Fig. 35.

9. Implications for hadron collider cross sections

According to the QCD factorization theorem, 'hard scattering' hadron collider cross sections can be expressed in terms of parton distribution functions convoluted with perturbatively calculable subprocess cross sections,

$$d\sigma_X = \sum_{ij} \int dx_1 dx_2 \, f_i(x_1,\mu^2) f_j(x_2,\mu^2) \, d\hat{\sigma}_{ij\to X} \, , \tag{44}$$

with, for example, $X = W^\pm, Z, Q\overline{Q}$, jets or Higgs. Processes with well-measured final states, and for which the next-to-leading order corrections to $\hat{\sigma}$ are known, can therefore provide important cross-checks on the parton distributions. A prime example is the W rapidity asymmetry at the Tevatron which, as we have just seen, is used in our global analysis to constrain the u and d distributions. Leading-order kinematics imply $x_{1,2} = M_X \exp(\pm y_X)/\sqrt{s}$. In general, at colliders like the Tevatron and the LHC, quark and gluon distributions are probed at x values where they are 'measured' by deep inelastic scattering and prompt photon experiments, but at significantly higher scales $\mu^2 \sim M_X^2$.

A precise knowledge of parton distributions is absolutely vital for reliable predictions for signal and background cross sections at the LHC [55]. Uncertainties can arise both from the starting distributions and from DGLAP evolution. A detailed assessment of these uncertainties illustrated with reference to various standard cross sections will be presented elsewhere [56]. In this section we focus on several standard cross sections measured at the Tevatron $p\bar{p}$ collider.

9.1 W, Z production

While the W (lepton) rapidity asymmetry probes the relative size of the u and d distributions, the *total* cross sections for W and Z boson production in $p\bar{p}$ collisions at $\sqrt{s} = 1.8$ TeV provide an important check of the overall magnitude of the quark distributions in a region of $x \sim 0.05 - 0.1$ where they are constrained at lower μ^2 by deep-inelastic (in particular NMC) data. Since the perturbative QCD subprocess cross section is known to next-to-next-to-leading order [57] and the electroweak parameters are precisely determined, there is very little theoretical uncertainty in the predictions once the parton distributions are specified.

We begin by displaying in Fig. 36 the W and Z total cross sections times the leptonic branching ratios[25] as measured by UA1 [58] and UA2 [59] at $\sqrt{s} = 630$ GeV and by CDF

[25]The Standard Model values $B(W \to l\nu) = 0.1084$ and $B(Z \to l^+l^-) = 0.03364$ are used. The electroweak boson masses are taken to be $M_W = 80.43$ GeV and $M_Z = 91.1887$ GeV.

[60] and D0 [61] at $\sqrt{s} = 1.8$ TeV, together with the predictions obtained using our default MRST set. Only the most recent (Run 1A) Tevatron published measurements are included. The factorization and renormalization scales are set equal to M_W and M_Z respectively. The overall agreement between theory and experiment is excellent.

To study this in more detail, we focus on the more precise Tevatron measurements and show, in Fig. 37, the predictions of the five MRST sets (the default MRST set, together with $g\uparrow, g\downarrow, \alpha_S\uparrow\uparrow, \alpha_S\downarrow\downarrow$). There is an overall spread of approximately $\pm 2\%$ about the default prediction,[26] significantly smaller than the current experimental errors. The variations in the predictions are easily understood. At these (small) x values, the quark distributions *increase* with increasing μ^2. The larger the α_S the faster the increase, and so $\sigma_V(\alpha_S\downarrow\downarrow) < \sigma_V(\text{MRST}) < \sigma_V(\alpha_S\uparrow\uparrow)$. The different gluon distributions also give rise to differences in the σ_V predictions. In this $x \sim 0.05$ region, the ordering of the gluon distributions is $g\uparrow < g(\text{MRST}) < g\downarrow$, see Fig. 37. The larger the gluon the more rapid the DGLAP evolution, and so $\sigma_V(g\uparrow) < \sigma_V(\text{MRST}) < \sigma_V(g\downarrow)$. The gluon variation is slightly smaller than the α_S variation.

We may conclude from Fig. 37 that for a given set of quark distributions fixed by DIS data at a relatively low $Q^2 \sim 10$ GeV^2 scale, the net uncertainty in the $\sigma_{W,Z}$ predictions at high $Q^2 \sim 10^4$ GeV^2 coming from the gluon, α_S and unknown higher-order corrections is of order $\pm 2\%$. The *true* theoretical uncertainty has a significant additional component from the uncertainty in the absolute normalizations of the (u and d) distributions as determined by the normalization uncertainties in the structure function data themselves. In the relevant x range for the Tevatron W and Z cross sections, the main constraints on the quarks come from the precise NMC F_2^p and F_2^d data. These have an overall systematic (normalization) error of approximately $\pm 2.5\%$, which would give a corresponding error of $\pm 5\%$ on the weak boson cross sections, comparable to the current experimental errors from CDF and D0. However this is almost certainly a large overestimate since the requirement of mutual consistency between the various deep inelastic data sets, together with the sum rule constraints, does not permit the possibility of changing the normalization of an individual data set over its full allowed range. This point will be addressed in [56].

A final point concerns the impact on the experimental cross sections of the luminosity measurement and uncertainty. The latter ($\pm 3.6\%$ for CDF and $\pm 5.4\%$ for D0 [60, 61]) dominate the most precise ($W \to e\nu$) cross section errors. In addition, the value assumed for the total $p\bar{p}$ cross section is slightly different for the two experiments, and this may account in part for the systematically smaller D0 cross sections displayed in Fig. 37.

9.2 Top production

At the Tevatron, $t\bar{t}$ production occurs dominantly ($\sim$90%) via $q\bar{q}$ annihilation. The cross section therefore samples valence u and d quarks at $x \gtrsim 2m_t/\sqrt{s} \sim 0.2 - 0.3$ and $\mu^2 \sim m_t^2 \sim$

[26] A measure of the scale dependence of these predictions is obtained by using instead $\mu = M_V/2$ and $2M_V$. The effect is shown as error bars on the default prediction and is evidently very small.

10^{4-5} GeV^2. The leading order subprocess cross section is proportional to α_S^2, but the enhancement obtained by increasing α_S is partially compensated by the decrease in the parton distributions at large x caused by more rapid DGLAP evolution.

The production cross section is known exactly at NLO [62]. It is traditional to estimate the residual theoretical scale dependent uncertainty by varying the factorization and renormalization scales in the range $m_t/2 < \mu < 2m_t$ which, at the Tevatron, gives an approximate $\pm 10\%$ variation about the $\mu = m_t$ prediction for a fixed set of partons and fixed α_S.

Another important effect is the higher-order contributions from soft gluon emission, which are expected to be large when the $t\bar{t}$ system is produced near threshold. Techniques have recently been developed for resumming the dominant leading (LL) $\ln(1 - 4m_q^2/\hat{s})$ logarithms [63]. In Ref. [64] the NLL logarithms have been computed and used to obtain an 'improved' resummed cross section. The effects of resummation are particularly large for large scale choices, whereas for $\mu = m_t/2$ the NLO cross section approximates the resummed cross section to better than 1% at Tevatron energies [64][27]. In our calculations we will therefore compute the top cross sections using NLO QCD, with $m_t = 175$ GeV and $\mu = m_t/2$.

Figure 38 shows predictions for the total $t\bar{t}$ cross section at the Tevatron using the five canonical MRST parton sets. Data points from CDF [65] and D0 [66] are also shown. The cross sections are slightly larger for the sets with the larger (large-x) gluon and larger α_S (although for the latter, note that the variation is smaller than the naive estimate of $\pm 10\%$ from the change in the overall α_S^2 value would suggest). The uncertainties due to the valence quarks, the gluons, and α_S are all at the $\pm 5\%$ level. The resulting overall parton distribution uncertainty in the $\sigma(t\bar{t})$ prediction is therefore at the $\pm 10\%$ level, comparable in magnitude to the scale dependence (combined with other higher-order effects [64]) uncertainty. The agreement with the current CDF and D0 measurements is entirely satisfactory.

9.3 Large E_T jet production

The single jet inclusive E_T distribution at the Tevatron is a particularly interesting observable. Even though the measured cross section falls by more than six orders of magnitude when E_T increases from 50 to 400 GeV, the NLO QCD predictions reproduce the data to well within the systematic error band. Nevertheless the detailed shape of the spectrum, taking only the statistical errors into account, shows interesting features. The spectrum has been measured by both the CDF and D0 collaborations [36, 37]. The experimental spectra are compared with the NLO predictions[28] obtained from five of our canonical sets of partons in Figs. 39–42. In each case we use the prediction of the MRST parton set as the base line for the comparison. The predictions contain an overall normalization factor which is adjusted to give the optimum description of the data. The value of the factor is shown on the plots for each set of partons.

[27] For the choice $\mu = m_t$ the effects of beyond-NLO resummation increase the NLO cross section by approximately 5% [64].

[28] We are grateful to Nigel Glover for help in performing these calculations.

Figs. 39 and 40 compare the CDF and D0 spectra with the predictions obtained from the three parton sets based on different gluons. It is interesting to see that the set, MRST($g\uparrow$), with the larger gluon at large x (that is the set in which the WA70 prompt photon data are fitted with partonic $\langle k_T \rangle = 0$) gives the best description of the shape of the observed spectrum and an overall normalization nearest to unity. The effect is particularly pronounced for the D0 data. Figs. 41 and 42 compare the CDF and D0 spectra with the predictions of parton sets corresponding to three different values of $\alpha_S(M_Z^2)$. In this case the parton set, MRS($\alpha_S\downarrow\downarrow$), with the smallest α_S gives the best description.

Note, however, that the comparisons between experiment and theory shown in Figs. 39–42 should not be taken too literally. Aside from the large experimental systematic errors which have not been included, there are residual theoretical uncertainties, for example from scale dependence and the precise modelling of the experimental jet algorithm, which are important at the $\mathcal{O}(\pm 5\%)$ level (see for example the recent study in Ref. [67]). It is therefore premature to draw any definite conclusions about preferred gluons distributions and/or α_S values.

A final point concerns the impact of 'intrinsic' transverse momentum smearing on the jet E_T distribution. Using the same procedure as implemented in the prompt photon studies of Section 4, we have investigated the effect of different choices of $\langle k_T \rangle$ on the shape of the distribution. Qualitatively, the effect is to *steepen* the distribution slightly at the low E_T end of the spectrum, as for the $p_T(\gamma)$ distributions shown in Figs. 22–24. For example, for $\langle k_T \rangle = 4$ GeV we find that the jet cross section is increased by +3% for $E_T = 75$ GeV, and by less than +1% for $E_T > 150$ GeV. The description of the CDF and D0 data by the canonical MRST parton set is not therefore improved.

10. Conclusions

In order to examine the partonic structure of nucleons we have performed a global analysis of data on deep inelastic scattering and related hard scattering processes using NLO-in-α_S QCD. This present treatment represents a significant improvement over our previous analyses for a number of reasons. First, there is the availability of a number of updated, or completely new sets of data. These have all been discussed in the introduction. However, we note that those experiments which have had a major impact on the changes to the parton distributions include those that produce a relatively small number of data points: i.e. the new data from the E866 and HERMES experiments, which constrain the value of $(\bar{u} - \bar{d})$; the extended data on the W rapidity asymmetry, which constrain d/u; and the new prompt photon data from the E706 experiment, which probe the gluon at high values of x.

There are also new features in the way in which we perform the analysis itself. For the first time we incorporate intrinsic parton k_T when examining those data which are sensitive to it, which in practice means the prompt photon data. We also use a new, much more sophisticated treatment of the charm (and bottom) contribution to structure functions. This new procedure naturally includes both a smooth behaviour in the threshold region and the summation of large logarithms at high Q^2, and gives a parameter free (up to the charm mass) prediction for the

charm contribution. For the first time we have also examined the sensitivity of the partons sets obtained to cuts in both Q^2 and x imposed on the data, letting the former vary between 2 GeV^2 and 10 GeV^2 and the latter up to $x_{\rm min} = 0.01$. We have also investigated the uncertainties which exist for our determination of the strong coupling constant α_S in a more systematic manner than in previous analyses, obtaining a quantitative estimate of the allowed variation about our central value of $\alpha_S(M_Z^2) = 0.1175$. Finally, for the first time we have also made a thorough investigation of the uncertainty in the gluon distribution obtained from our analysis, producing two sets of partons which represent two extremes as well as the central, preferred set.

Both the new data sets and the new theoretical procedures have led to significant differences between the MRST partons and those produced by previous analyses. In order to exhibit these differences we can look at Figs. 3 and 4, which show the comparison between the MRST partons and the preferred set from our previous global analysis, i.e. MRS(R2). First, looking at the comparison at $Q^2 = 10$ GeV^2, most partons show significant differences. The new gluon is much smaller for $x \gtrsim 0.2$, since the inclusion of intrinsic k_T means a smaller gluon is required to fit the WA70 prompt photon data. The form of the gluon at small x is constrained by the HERA data, and therefore the momentum sum rule allows a larger gluon at $x \sim 0.05$. The form of the charm quark distribution is clearly very different to our previous MRS(R) analysis [25], where the evolution of the charm quark in the $\overline{\rm MS}$ scheme took place from $Q^2 = 1$ GeV^2 rather than the correct value of $Q^2 = m_c^2$, and a phenomenological damping factor was used. It is this damping factor which led to the previous small charm distribution at small x. However, the charm distribution is driven by the gluon distribution, and one can see that the difference in shape between the new and old charm distribution mirrors that of the gluon. It is this which causes the MRS(R2) charm quark to be larger at large x, overcoming the effect of the damping factor which is a function of Q^2 only. The light quark distributions are all a little larger for the MRS(R2) partons at small x, compensating for the smaller charm distribution. At high x the u quark is essentially unchanged, the d quark is larger in the MRST partons in order to accommodate the extended W asymmetry data, and the strange quark (which effectively represents the sea quark distribution) is a little smaller, presumably due to the requirements of fitting the Drell-Yan data with a slightly larger valence quark distribution. Also examining Fig. 4 we see that the systematic differences between the light partons are of the same form as at the lower Q^2 value, but have been washed out somewhat (in particular the small x form of the partons is almost identical in each set). However, the charm distribution is still very different. Again, the shape difference mirrors that of the gluon, but the MRS(R2) charm distribution is larger. This is because the damping factor is now unity at such a high value of Q^2, but the fact that the evolution of the MRS(R2) distribution began at lower Q^2 results in a constant difference between the two distributions, i.e. the charm generated in the evolution from $Q^2 = 1$ GeV^2 to $Q^2 = m_c^2$. Although this difference disappears in the ratio asymptotically, it is still significant at $Q^2 = 10^4$ GeV^2.

We can also compare the new MRST partons with the preferred set of the most recent CTEQ analysis, i.e. CTEQ4M. This comparison is displayed in Fig. 43. We first compare

the partons at $Q^2 = 10$ GeV^2. In the high x region there is very little difference between the CTEQ4M partons and the MRS(R2) partons. The CTEQ4M strange (and therefore sea) distribution becomes much larger at $x \gtrsim 0.4$, but this is beyond the range of the E605 Drell-Yan data. Hence, all differences between quarks in this region are presumably due to the new data included in the MRST analysis. Even the gluon is similar to MRS(R2) in this range, being constrained mainly by the high-E_T jet data, which, as we have already noted, require a high x gluon similar to MRST($g\uparrow$). However, the CTEQ4M gluon becomes significantly larger than the MRST gluon at small x, leading to a stronger growth of $F_2(x,Q^2)$ with Q^2 in this region. This is partly due to the Q^2 cut of 4 GeV^2 imposed by CTEQ, and a similar trend is seen for our gluon when similar cuts are imposed, as demonstrated in Fig. 19. Since the evolution of the charm parton distribution is the same for CTEQ4M as for MRST (the treatment of the coefficient function being very different), differences in the charm are largely due to differences in the gluon, and indeed the shape of the charm ratios mirrors that of the gluon ratios. The light quark distributions at small x are a little smaller than those for the MRST partons, but as with the gluon differences this can be attributed mainly to the different cuts, the same qualitative effect again being seen in Fig. 19. However, the slightly different ratio between the u and d quarks and the strange quarks, even at $x = 10^{-4}$, is due to the CTEQ requirement that $2\bar{s}/(\bar{u}+\bar{d}) = 0.5$ at $Q^2 = 2.56$ GeV^2 rather than 1 GeV^2, which results in the strange quark being a little smaller. In the intermediate x region the CTEQ4M u and d quarks are both slightly larger than those for MRST, compensating for the smaller strange and charm quarks. As with the previous comparison, differences between the parton sets tend to be washed out at very high Q^2.

In summary the main differences between the CTEQ4M and MRST partons arise from (i) our inclusion of new data, (ii) the different treatment of the gluon at large x and (iii) the choice of cuts in Q^2. However, there are some small additional systematic differences between the two analyses. The normalizations imposed on the data sets are a percent or two higher for CTEQ than MRST. If we compare CTEQ4M partons with those obtained in our analysis using a comparable Q^2 cut ($Q^2 > 5$ GeV^2) then the partons are more similar, but significant differences remain. These may be due to the systematic difference between the output of the evolution programs, as noted in [68]. With the quality of data now available such differences are becoming significant.

Let us briefly justify our confidence in our new canonical set of partons (MRST). As we have seen they give an excellent overall description of the data. There are certain conflicts: as in our previous analyses we omit the (new) CCFR neutrino F_2 and xF_3 data for $x < 0.1$ from our fit as explained in Section 3; and we have also noted a discrepancy with the E772 Drell-Yan data for large x_F and small τ. There is also a slight systematic discrepancy with the measured value of $\partial F_2(x,Q^2)/\partial \ln Q^2$ for the NMC data below $x = 0.1$ and for some of the HERA data. The quality of the fit to these data is clearly very satisfactory, but this observed effect may be a sign that NLO-in-α_S DGLAP evolution is not sufficient at small x, and that theoretical corrections are required.[29] It will be interesting to see whether further HERA data

[29]The discrepancy with the E772 data occurs when one of the partons has $x \sim 0.03$, but it seems unlikely

confirms the observed trend, and measurements at high y may be particularly important since they probe both $F_2(x,Q^2)$ and $F_L(x,Q^2)$. We see from Fig. 20 that if we vary α_S away from our central value of 0.1175 in either direction, then the quality of the fit to one or more of the data sets becomes rather poor very quickly. Hence, variation of α_S allows very little variation in our partons. We believe that our default set of partons, denoted simply by MRST, gives the most reliable treatment of the gluon at high x. The E706 prompt photon data have made it clear that intrinsic parton k_T is required, as one might expect from theoretical arguments and from the evidence already observed in Drell-Yan data. It is also very plausible that the amount of intrinsic k_T increases with centre of mass energy, and this hypothesis has recently received support from the theoretical calculation of Ref. [39]. Hence, the MRST($g\uparrow$) gluon obtained from assuming zero intrinsic k_T for the fit to WA70 data is clearly at one extreme, while the MRST($g\downarrow$) gluon obtained from allowing the partons to have the maximum $\langle k_T\rangle$ in the fit to WA70 data is at the other extreme by construction. The default MRST gluon has $\langle k_T\rangle$ intermediate to these extremes. While we cannot be absolutely sure of the most appropriate values of $\langle k_T\rangle$ to take for the two prompt photon experiments they cannot be much different to those employed in MRST. Since MRST($g\uparrow$) and MRST($g\downarrow$) represent such extreme variation in parton $\langle k_T\rangle$ we feel that the variation in the gluon they encompass is also sufficient to account for the smaller effect of scale dependence in prompt photon production. We note that there is no dependence on intrinsic parton k_T in any of the other data sets we analyse except for the high E_T jet data from CDF and D0, where the effect is very small, and not helpful.

We now have the most complete determination of the proton parton distributions yet achieved, both in terms of the theoretical treatment and in terms of the data analysed. However, in both there are possible improvements to be made. In terms of the theoretical procedure used in the analysis there are two major points. At present we use a leading twist NLO-in-α_S calculation. However, there are both leading $\ln(1/x)$ and higher twist corrections which should have a significant effect in certain kinematic domains (we impose a cut in W^2 in order to remove the sensitivity to higher twist effects at high x and low Q^2), and a hint of this is perhaps seen in the results of our analysis when different cuts are applied. In order to be truly confident of our results over the whole kinematic domain we need either proof that these possible corrections are very small, or a reliable method of including them in our analysis. Also, our present treatment of intrinsic parton k_T is phenomenologically inspired. While we believe it is a good representation of the true effects we await an improved theoretical understanding of the origin of both perturbative and nonperturbative intrinsic k_T, hopefully pinning down the actual amount in a quantitative manner.

There are a number of improvements in data which would also be very important in increasing the accuracy of determinations of parton distributions. Obviously, any increase in the precision of existing data and/or a widening of the kinematic range would be useful. It would be advantageous to have further sources of neutrino structure function data as a consistency check, since at present the analysis relies on a single high precision experiment. Of particular

that such a large discrepancy can be cured by leading $\ln(1/x)$ effects at such a high value of x.

use would be an increase in both the amount and precision of data on the charm structure function, as this would help differentiate between different prescriptions for heavy flavour effects, be a direct probe of the gluon, and possibly be important in determining small x corrections. We anticipate data of this type from HERA in the near future. Likewise, data on the bottom structure function would be useful for the same reasons, but since the mass is higher, it would be a cleaner probe of perturbative QCD. Finally, it would be very interesting to have a direct measurement of $F_L(x, Q^2)$ at small x, as this is an excellent test of different approaches to incorporating small x corrections.

In summary we have used all the deep inelastic and hard scattering data in order to obtain what we believe is the most precise determination of parton distributions of the proton to date. On the theoretical side this illuminates the short-distance structure of the proton, while at the same time it provides an essential ingredient for extracting new physics from current and forthcoming hadron colliders.

Acknowledgements

We thank Arie Bodek, Chuck Brown, Antje Bruell, Albert De Roeck, Jerry Garvey, Joey Huston, Mike Vetterli and Manuella Vincter for valuable discussions and information concerning the data. This work was supported in part by the EU Fourth Framework Programme 'Training and Mobility of Researchers', Network 'Quantum Chromodynamics and the Deep Structure of Elementary Particles', contract FMRX-CT98-0194 (DG 12 - MIHT).

TABLE I. The numerical values of the parameters of the starting distributions of three parton sets which differ in the value of the initial state partonic $\langle k_T \rangle$ used to describe the prompt photon data. The three columns correspond to $\langle k_T \rangle = 0.64$, 0.4 and 0 GeV for WA70 respectively. Note that A_g is fixed by the momentum sum rule and that A_u, A_d are fixed by flavour sum rules, and are not therefore free parameters.

	Lower gluon MRST($g\downarrow$)	Central gluon MRST	Higher gluon MRST($g\uparrow$)
(A_g)	89.32	64.57	152.1
(A_u)	0.8884	0.6051	0.7763
(A_d)	0.05950	0.05811	0.06015
λ_g	-1.082	-0.9171	-1.035
η_g	6.124	6.587	7.451
ϵ_g	-2.409	-3.168	-4.341
γ_g	1.562	3.251	5.251
η_1	0.4710	0.4089	0.4398
η_2	3.404	3.395	3.427
ϵ_u	1.628	2.078	1.152
γ_u	9.628	14.56	12.36
η_3	0.2736	0.2882	0.2694
η_4	3.902	3.874	3.941
ϵ_d	29.78	34.69	27.96
γ_d	35.09	28.96	38.35
A_S	0.2699	0.2004	0.1786
λ_S	0.2410	0.2712	0.2819
η_S	7.549	7.808	8.212
ϵ_S	0.2062	2.283	3.725
γ_S	18.35	20.69	21.80
A_Δ	0.1494	1.290	1.260
η_Δ	0.6440	1.183	1.157
γ_Δ	42.94	9.987	9.778
δ_Δ	-100.8	-33.34	-30.83

TABLE II. The fractions of the total momentum of the proton carried by the various partons in the MRST set.

Q^2 (GeV^2)	u_v	d_v	$2\bar{u}$	$2\bar{d}$	$2\bar{s}$	$2\bar{c}$	$2\bar{b}$	g
2	0.310	0.129	0.058	0.075	0.037	0.001	0.000	0.388
20	0.249	0.103	0.063	0.077	0.046	0.017	0.000	0.439
200	0.216	0.090	0.066	0.078	0.052	0.026	0.012	0.456
2×10^3	0.194	0.080	0.068	0.079	0.056	0.032	0.020	0.466
2×10^4	0.178	0.074	0.070	0.080	0.058	0.036	0.026	0.472
2×10^5	0.165	0.068	0.072	0.081	0.061	0.040	0.030	0.477

TABLE III. Processes studied in the global analysis.

Process/ Experiment	**Leading order subprocess**	**Parton behaviour probed**
DIS ($\mu N \to \mu X$) $F_2^{\mu p}$, $F_2^{\mu d}$, $F_2^{\mu n}/F_2^{\mu p}$ (SLAC, BCDMS, NMC, E665)	$\gamma^* q \to q$	Four structure functions $\to$ $u+\bar{u}$, $d+\bar{d}$, $\bar{u}+\bar{d}$, s (assumed $=\bar{s}$), but only $\int x g(x,Q_0^2)dx \simeq 0.35$ and $\int(\bar{d}-\bar{u})dx \simeq 0.1$
DIS ($\nu N \to \mu X$) $F_2^{\nu N}$, $xF_3^{\nu N}$ (CCFR)	$W^* q \to q'$	
DIS (small x) F_2^{ep} (H1, ZEUS)	$\gamma^*(Z^*)q \to q$	λ $(x\bar{q} \sim x^{-\lambda_S},\ xg \sim x^{-\lambda_g})$
DIS (F_L) NMC, HERA	$\gamma^* g \to q\bar{q}$	g
$\ell N \to c\bar{c}X$ F_2^c (EMC; H1, ZEUS)	$\gamma^* c \to c$	c $(x \gtrsim 0.01;\ x \lesssim 0.01)$
$\nu N \to \mu^+\mu^- X$ (CCFR)	$W^* s \to c$ $\hookrightarrow \mu^+$	$s \approx \frac{1}{4}(\bar{u}+\bar{d})$
$pN \to \gamma X$ (WA70, UA6, E706, ...)	$qg \to \gamma q$	g at $x \simeq 2p_T^\gamma/\sqrt{s} \to$ $x \approx 0.2 - 0.6$
$pN \to \mu^+\mu^- X$ (E605, E772)	$q\bar{q} \to \gamma^*$	$\bar{q} = ...(1-x)^{\eta s}$
$pp, pn \to \mu^+\mu^- X$ (E866, NA51)	$u\bar{u}, d\bar{d} \to \gamma^*$ $u\bar{d}, d\bar{u} \to \gamma^*$	$\bar{u} - \bar{d}$ $(0.04 \lesssim x \lesssim 0.3)$
$ep, en \to e\pi X$ (HERMES)	$\gamma^* q \to q$ with $q = u, d, \bar{u}, \bar{d}$	$\bar{u} - \bar{d}$ $(0.04 \lesssim x \lesssim 0.2)$
$p\bar{p} \to WX(ZX)$ (UA1, UA2; CDF, D0)	$ud \to W$	u, d at $x \simeq M_W/\sqrt{s} \to$ $x \approx 0.13;\ 0.05$
$\to \ell^\pm$ **asym** (CDF)		slope of u/d at $x \approx 0.05 - 0.1$
$p\bar{p} \to t\bar{t}X$ (CDF, D0)	$q\bar{q}, gg \to t\bar{t}$	q, g at $x \gtrsim 2m_t/\sqrt{s} \simeq 0.2$
$p\bar{p} \to$jet $+ X$ (CDF, D0)	$gg, qg, qq \to 2j$	q, g at $x \simeq 2E_T/\sqrt{s} \to$ $x \approx 0.05 - 0.5$

TABLE IV. The χ^2 values for the DIS data included in the three global fits which resulted in the parameter values listed in Table I.

Data set	No. of data pts	MRST	MRST($g\uparrow$)	MRST($g\downarrow$)
H1 ep	221	164	166	161
ZEUS ep	204	269	273	258
BCDMS μp	174	248	239	264
NMC μp	130	141	148	142
NMC μd	130	101	107	104
SLAC ep	70	119	104	135
E665 μp	53	59	54	56
E665 μd	53	61	62	61
CCFR $F_2^{\nu N}$	66	93	102	92
CCFR $F_3^{\nu N}$	66	68	69	67
NMC n/p	163	186	192	174

Notes:

(i) The relative normalizations of the data sets are taken to be unity, except that the BCDMS μp data is normalized down by 2% and the SLAC ep data up by 2.5%.

(ii) The CCFR data are corrected for heavy (iron) target effects using the information obtained from the muon-nucleus measurements. Since the $x < 0.1$ corrected CCFR data are in disagreement with the NMC data, they are omitted from the fit. Only statistical errors together with a 1.5% uncertainty (to represent uncertainty in the heavy target correction) are included in the χ^2 for the CCFR data since no overall systematic errors are given.

(iii) All deuterium data are corrected for shadowing effects using the method of Badelek and Kwiecinski [28].

References

[1] H1 collaboration: S. Aid et al., Nucl. Phys. **B470** (1996) 3; C. Adloff et al., Nucl. Phys. **B497** (1997) 3.

[2] ZEUS collaboration: M. Derrick et al., Zeit. Phys. **C69** (1996) 607; M. Derrick et al., Zeit. Phys. **C72** (1996) 399.

[3] CCFR collaboration: W.G. Seligman et al., Phys. Rev. Lett. **79** (1997) 1213.

[4] CCFR collaboration: A.O. Bazarko et al., Columbia University Report No. NEVIS-1492, 1993 (unpublished).

[5] H1 collaboration: C. Adloff et al., Zeit. Phys. **C72** (1996) 593.

[6] ZEUS collaboration: J. Breitweg et al., Phys. Lett. **B407** (1997) 402; Paper N-645 presented at International Europhysics Conference on High Energy Physics, HEP97, Jerusalem 1997.

[7] J.J. Aubert et al., Nucl. Phys. **B213** (1983) 31.

[8] E706 collaboration: L. Apanasevich et al., `hep-ex/9711017`.

[9] WA70 collaboration: M. Bonesini et al., Z. Phys. **C38** (1988) 371.

[10] E866 collaboration: E.A. Hawker et al., `hep-ex/9803011`, to be published in Phys. Rev. Lett.

[11] NA51 collaboration: A. Baldit et al., Phys. Lett. **B332** (1994) 244.

[12] CDF collaboration: presented by A. Bodek at the Cracow International Symposium on Radiative Corrections (CRAD96), Cracow, Poland, August 1–5, 1996, Acta Phys. Polon. **B28** (1997) 477.

[13] NMCollaboration: M. Arneodo et al., Nucl. Phys. **B483** (1997) 3.

[14] E772 collaboration: P.L. McGaughey et al., Phys. Rev. **D50** (1994) 3038.

[15] E605 collaboration: G. Moreno et al., Phys. Rev. **D43** (1991) 2815.

[16] CCFR collaboration: A.O. Bazarko et al., Z. Phys. **C65** (1995) 189.

[17] R806 collaboration: T. Akesson et al., Sov. J. Nucl. Phys. **51** (1990) 836;
UA2 collaboration: J. Alitti et al., Phys. Lett. **B263** (1991) 544;
UA6 collaboration: G. Ballocchi et al., Phys. Lett. **B317** (1993) 243, 250;
CDF collaboration: F. Abe et al., Phys. Rev. Lett. **73** (1994) 2662.

[18] CTEQ collaboration: J. Huston et al., Phys. Rev. **D51** (1995) 6139.

[19] See for example: W.J. Stirling, hep-ph/9709429.

[20] CTEQ collaboration: H.-L. Lai et al., Phys. Rev. **D55** (1997) 1280.

[21] CTEQ collaboration: J. Huston et al., hep-ph/9801444.

[22] BCDMS collaboration: A.C. Benvenuti et al., Phys. Lett. **B223** (1989) 485.

[23] E665 collaboration: M.R. Adams et al., Phys. Rev. **D54** (1996) 3006.

[24] L.W. Whitlow et al., Phys. Lett. **B282** (1992) 475;
L.W. Whitlow, preprint SLAC-357 (1990).

[25] A.D. Martin, R.G. Roberts and W.J. Stirling, Phys. Lett. **B387** (1996) 419.

[26] H1 collaboration: Paper 262 presented at International Europhysics Conference on High Energy Physics, HEP97, Jerusalem 1997.

[27] M. Glück, E. Reya and A. Vogt, Zeit. Phys. **C67** (1995) 433.

[28] B. Badelek and J. Kwiecinski, Phys. Rev. **D50** (1994) R4.

[29] A. Milsztajn and M. Virchaux, Phys. Lett. **B274** (1992) 221.

[30] A.M. Cooper-Sarkar et al., Zeit. Phys. **C39** (1988) 281.

[31] E.B. Zijlstra and W.L van Neerven, Nucl. Phys. **B383** (1992) 525;
S.A. Larin and J.A.M. Vermaseren, Zeit. Phys. **C57** (1993) 93.

[32] S. Riemersma, J. Smith and W.L. van Neerven, Phys. Lett. **B347** (1995) 143;
E. Laenen, S. Riemersma, J. Smith and W.L. van Neerven, Nucl. Phys. **B392** (1993) 162.

[33] H1 collaboration: Phys. Lett. **B393** (1997) 452.

[34] R.S. Thorne, hep-ph/9708302, to be published in Phys. Lett.

[35] A.D. Martin, R.G. Roberts and W.J. Stirling, Phys. Lett. **B356** (1995) 89.

[36] CDF collaboration: F. Abe et al., Phys. Rev. Lett. **77** (1996) 438. See also: B. Flaugher, Proceedings of the XVII International Conference on Physics in Collision, University of Bristol, UK, June 25–27, 1997.

[37] D0 collaboration: F. Nang (for the CDF and D0 collaborations) *Jet Production at the Tevatron*, Proceedings of the XXXII Rencontres de Moriond 'QCD and High Energy Hadronic Interactions', Les Arcs, France, March 22–29, 1997, preprint FERMILAB-Conf-97/192-E.

[38] L.E. Gordon and W. Vogelsang, Phys. Rev. **D50** (1994) 1901.

[39] H.-L. Lai and H. Li, hep-ph/9802414.

[40] W. Vogelsang and A. Vogt, Nucl. Phys. **B453** (1995) 334.

[41] CTEQ collaboration: J. Huston et al., Phys. Rev. **D51** (1995) 6139.

[42] E706 collaboration: J. Huston, private communication.

[43] See for example: W.J. Stirling and M.R. Whalley, J. Phys. G. Nucl. Part. Phys. **19** (1993) D1.

[44] F. Olness and W.-K. Tung, Nucl. Phys. **B308** (1988) 813;
M. Aivazis, F. Olness and W.-K. Tung, Phys. Rev. **D50** (1994) 3085;
M. Aivazis, J.C. Collins, F. Olness and W.-K. Tung, Phys. Rev. **D50** (1994) 3102.

[45] A.D. Martin, R.G. Roberts, M.G. Ryskin and W.J. Stirling, hep-ph/9612449, to be published in Eur. Phys. J.

[46] R.S. Thorne and R.G. Roberts, hep-ph/9709442, to be published in Phys. Rev. **D**.

[47] R.S. Thorne and R.G. Roberts, hep-ph/9711223, to be published in Phys. Lett. **B**.

[48] M. Buza et al., Nucl. Phys. **B472** (1996) 611;
M. Buza, Y. Matiounine, J. Smith and W.L. van Neerven, Eur. Phys. J. **C1** (1998) 301; Phys. Lett. **B411** (1997) 211.

[49] S.D. Ellis and W.J. Stirling, Phys. Lett. **B256** (1991) 258.

[50] HERMES collaboration, presented by M. Vincter at the Lake Louise Winter Institute, Lake Louise, Canada, February, 1998.

[51] NMCollaboration: P. Amaudruz et al., Phys. Rev. Lett. **66** (1991) 2712.

[52] NMCollaboration: M. Arneodo et al., Phys. Rev. **D50** (1994) R1.

[53] W.T. Giele, E.W.N. Glover and D. Kosower, Nucl. Phys. **B403** (1993) 633.

[54] C. Balázs and C.-P. Yuan, Phys. Rev. **D56** (1997) 5558.

[55] See for example: *Parton Distributions and the LHC*, W.J. Stirling, presented at the Theory of LHC Processes Workshop, CERN, February 9 – 13, 1998 (transparencies available from http://wwwth.cern.ch/lhcworkshop98/ps/program.html).

[56] A.D. Martin, R.G. Roberts, W.J. Stirling and R.S. Thorne, in preparation.

[57] R. Hamberg, T. Matsuura and W.L. van Neerven, Nucl. Phys. **B345** (1990) 331; Nucl. Phys. **B359** (1991) 343.
W.L. van Neerven and E.B. Zijlstra, Nucl. Phys. **B382** (1992) 11.

[58] UA1 collaboration: C. Albajar et al., Z. Phys. **C44** (1989) 115.

[59] UA2 collaboration: J. Alitti et al., Z. Phys. **C47** (1990) 11.

[60] CDF collaboration: F. Abe et al., Phys. Rev. Lett. **76** (1996) 3070.

[61] D0 collaboration: S. Abachi et al., Phys. Rev. Lett. **75** (1995) 1456.

[62] P. Nason, S. Dawson and R.K. Ellis, Nucl. Phys. **B312** (1989) 607;
W. Beenakker, H. Kuijf, W.L. van Neerven and J. Smith, Phys. Rev. **D40** (1989) 54.

[63] E. Laenen, J. Smith and W.L. van Neerven, Nucl. Phys. **B369** (1992) 543; Phys. Lett. **B321** (1994) 254;
E. Berger and H. Contopagnos, Phys. Lett. **B361** (1995) 115; Phys. Rev. **D54** (1996) 3085, **D57** (1998) 253;
E. Berger, `hep-ph/9801381`;
S. Catani, M.L. Mangano, P. Nason and L. Trentadue, Phys. Lett. **B351** (1996) 555; Nucl. Phys. **B478** (1996) 273.

[64] R. Bonciano, S. Catani, M.L. Mangano and P. Nason, `hep-ph/9801375`.

[65] CDF collaboration: F. Abe et al., `FERMILAB-PUB-97/286-E`.

[66] D0 collaboration: S. Abachi et al., Phys. Rev. Lett. **79** (1997) 1203.

[67] B. Abbott et al., `hep-ph/9801285`.

[68] J. Blümlein et al., Proc. of the 1996 HERA Physics Workshop, ed. G. Ingelman, R. Klanner and A. De Roeck, DESY, Hamburg, 1996, Vol. 1, p. 23.

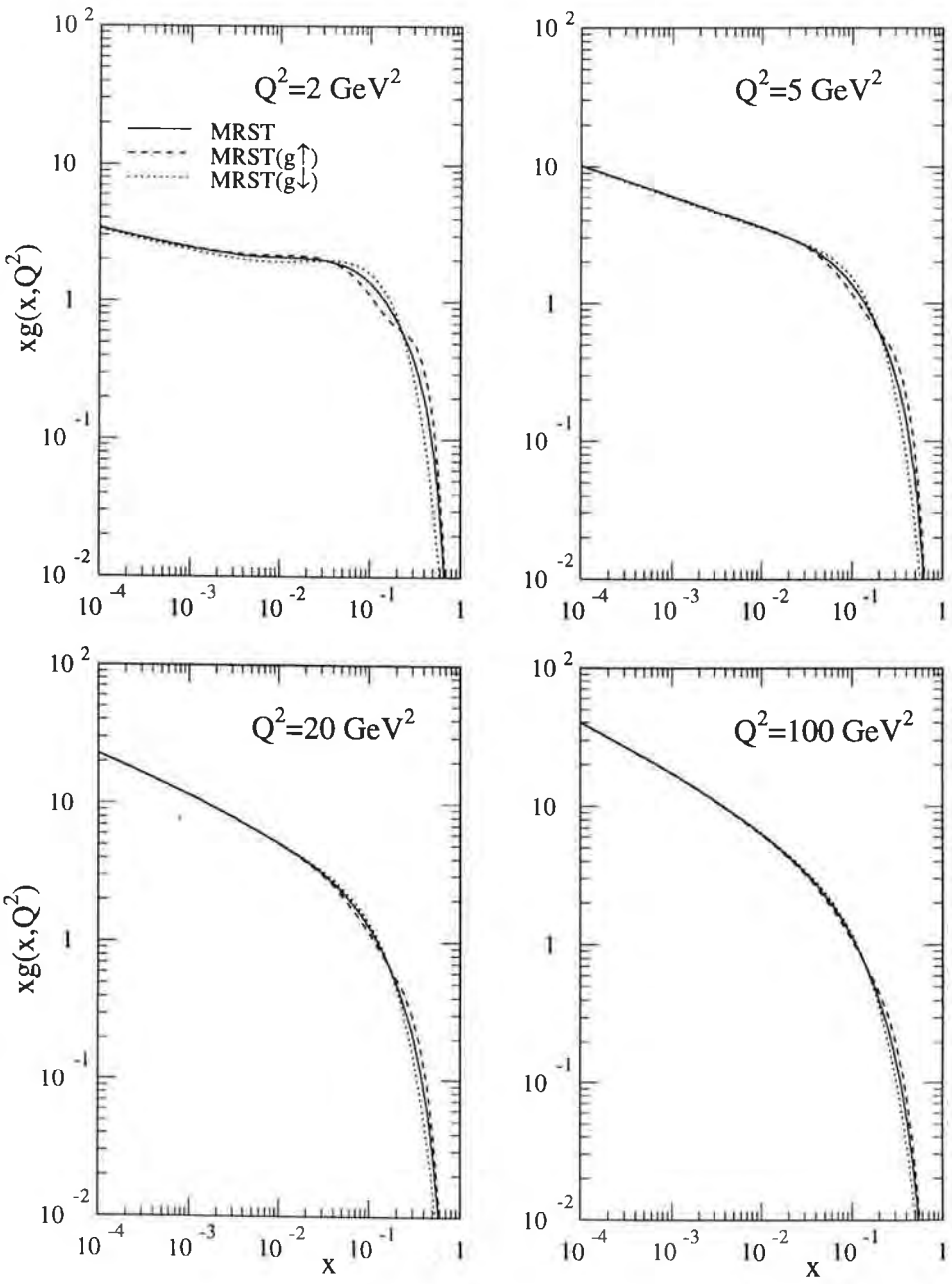

Figure 1: The gluon distributions at $Q^2 = 2$, 5, 20 and 100 GeV^2 corresponding to the MRST, MRST($g\uparrow$) and MRST($g\downarrow$) sets of partons with, respectively, the central, larger and smaller gluon at large x. We take MRST as the default set of partons throughout the paper.

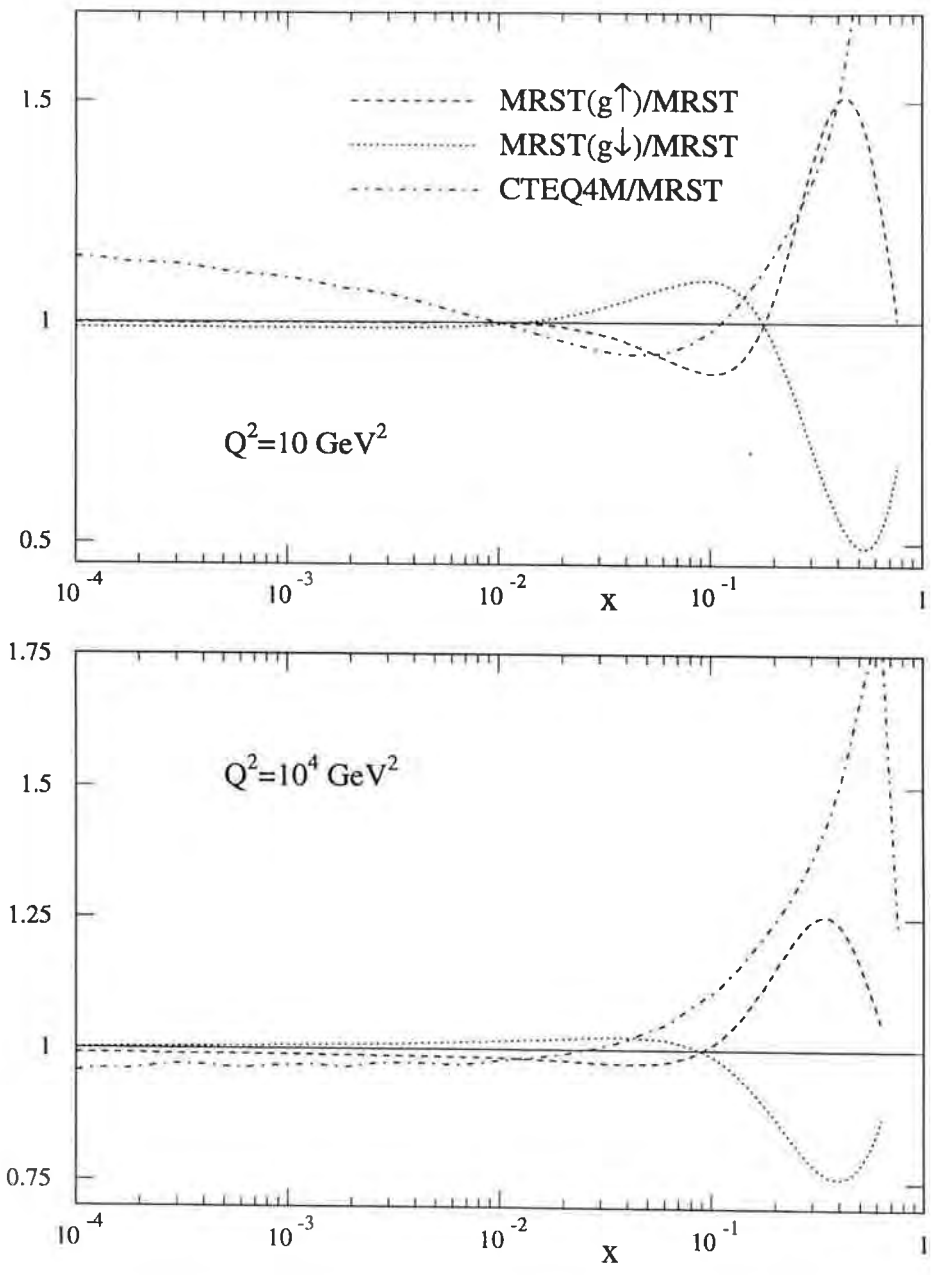

Figure 2: The ratios of the $g\uparrow$ and $g\downarrow$ gluons to the 'central' gluon (MRST) at $Q^2 = 10$ and 10^4 GeV^2. For comparison the ratio of the CTEQ4M [20] gluon to our central gluon is also shown.

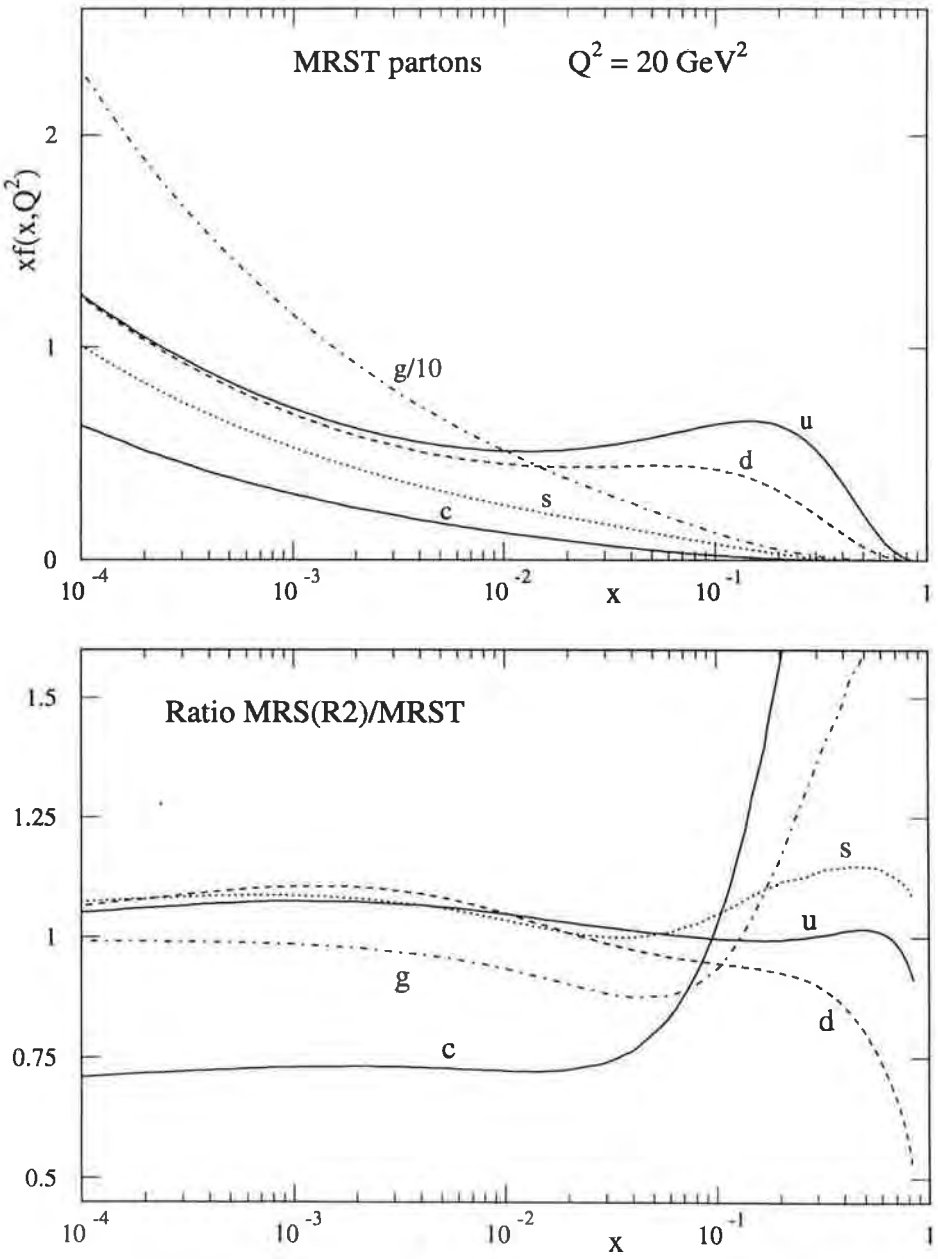

Figure 3: MRST partons at $Q^2 = 20$ GeV^2 (upper plot), together with the ratios of one of the previous sets [25] – MRS(R2) – to the new set at the same value of Q^2 (lower plot).

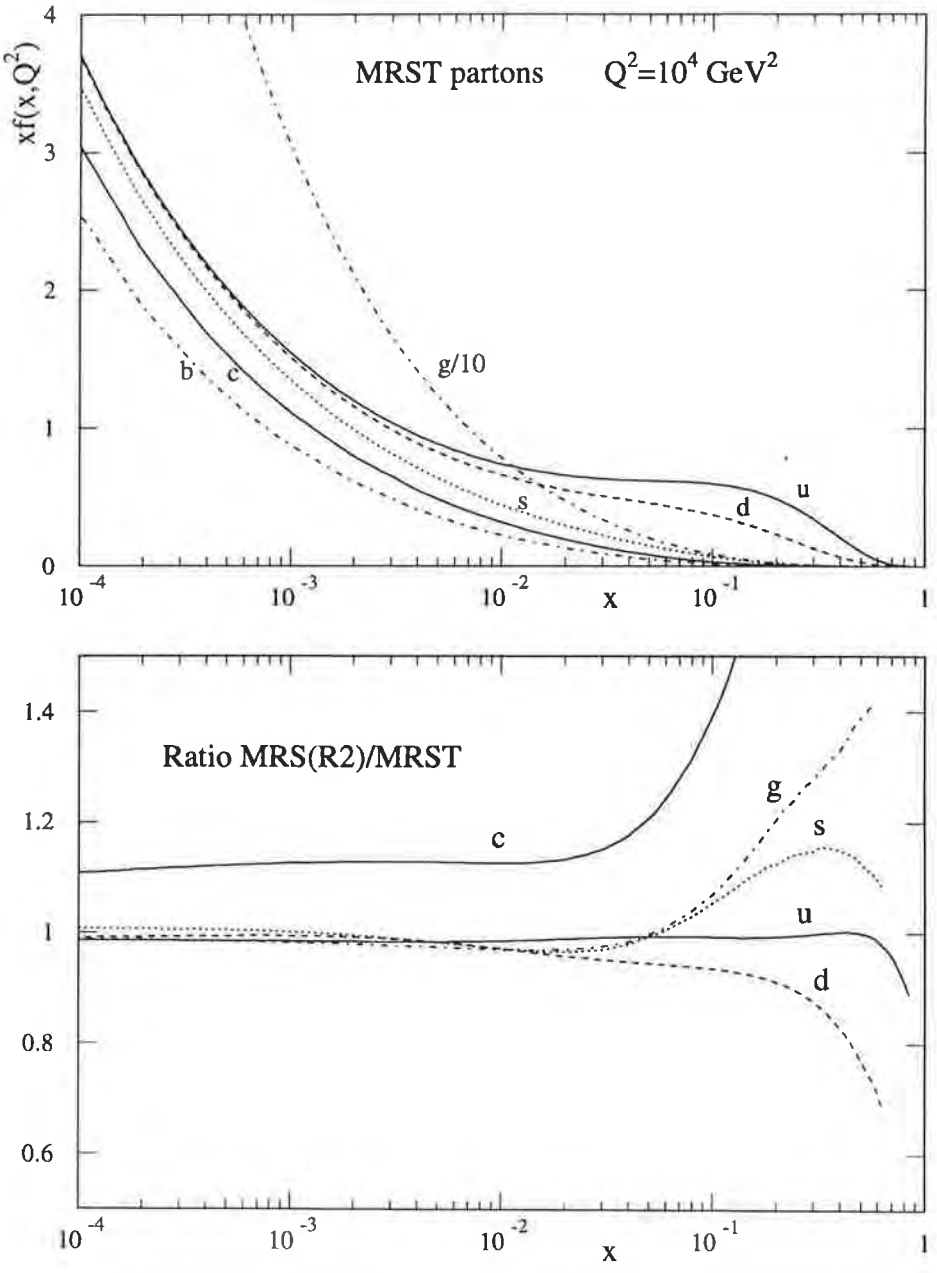

Figure 4: MRST partons at $Q^2 = 10^4$ GeV^2 (upper plot), together with the ratios of one of the previous sets – MRS(R2) – to the new set at the same value of Q^2 (lower plot).

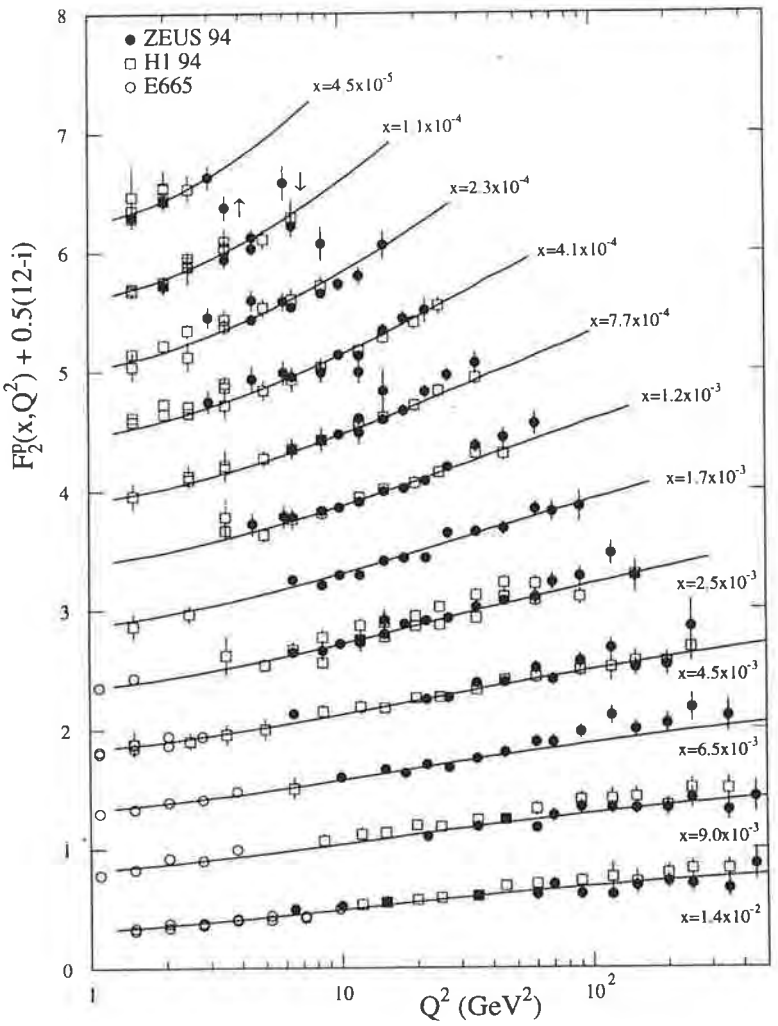

Figure 5: The description of the F_2^p data at small x by the MRST set of partons. The comparison is made at twelve values of x chosen to be the most appropriate for the new HERA data. For display purposes we add $0.5(12-i)$ to F_2^p each time the value of x is decreased, where $i = 1, 12$. The experimental data are assigned to the x value which is closest to the experimental x bin. Thus the ZEUS data [2] are shown in groupings with x values $(3.5, 6.3, 6.5 \times 10^{-5})$, $(1.02, 1.20 \times 10^{-4})$, $(1.98, 2.53 \times 10^{-4})$, $(4.0, 4.5 \times 10^{-4})$, $(6.32, 8.00 \times 10^{-4})$, $(1.02, 1.20 \times 10^{-3})$, (1.612×10^{-3}), $(2.53, 2.60 \times 10^{-3})$, (4.00×10^{-3}), (6.325×10^{-3}), (1.02×10^{-2}), (1.612×10^{-2}), and the H1 data [1] in groupings with x values $(3.2, 5.0 \times 10^{-5})$, $(0.80, 1.30 \times 10^{-4})$, $(2.0, 2.5 \times 10^{-4})$, $(3.2, 5.0 \times 10^{-4})$, $(6.3, 8.0 \times 10^{-4})$, (1.3×10^{-3}), (1.585×10^{-3}), $(2.0, 2.5, 3.2 \times 10^{-3})$, $(3.98, 4.0, 5.0 \times 10^{-3})$, (6.3×10^{-3}), (8.0×10^{-3}), (1.3×10^{-2}). The E665 data [23], which are shown on the curves with the five largest x values, are measured at $x = (2.46 \times 10^{-3})$, $(3.698, 5.2 \times 10^{-3})$, (6.934×10^{-3}), (8.933×10^{-3}), $(1.225, 1.73 \times 10^{-2})$.

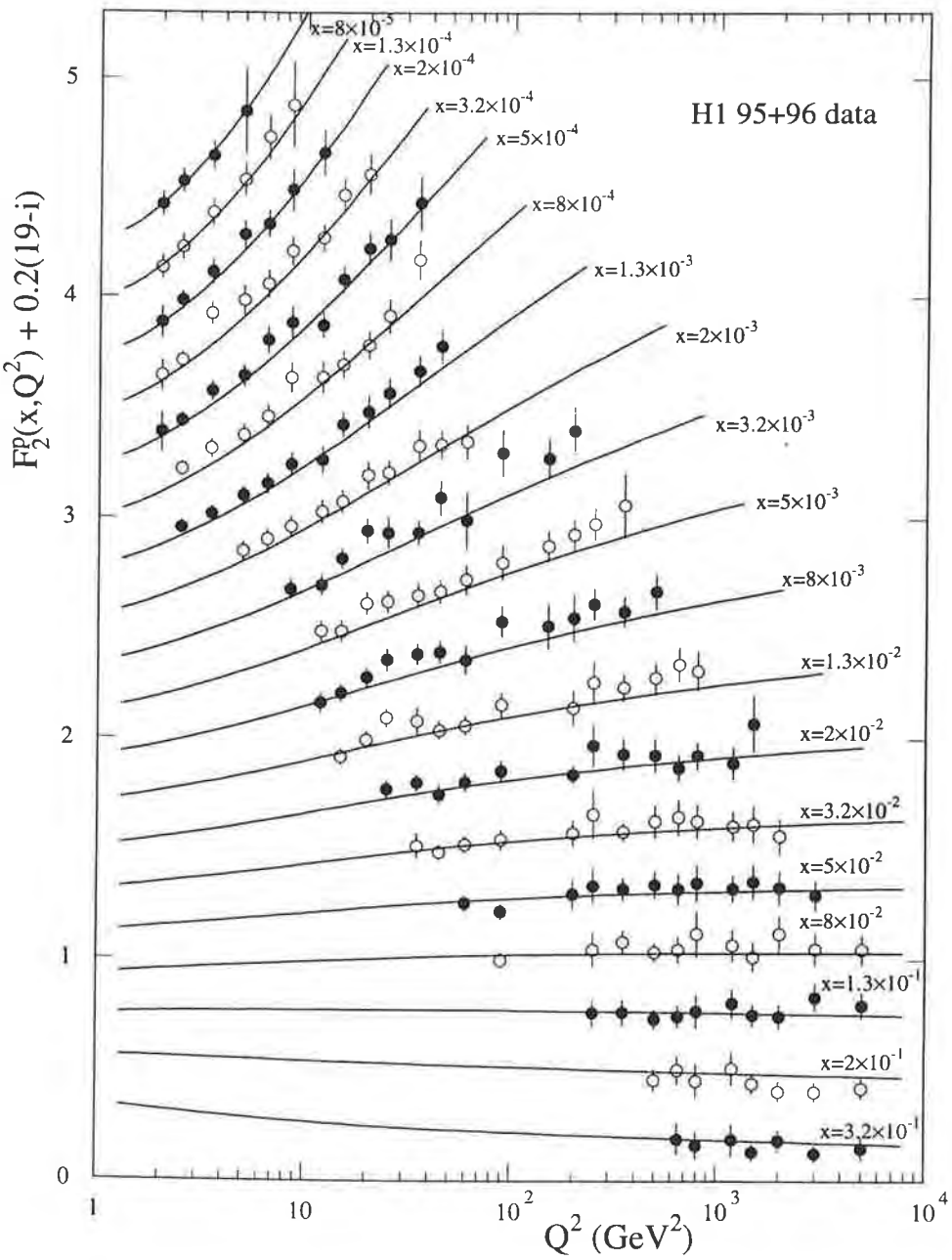

Figure 6: Comparison of the F_2^p predictions of the MRST partons with the 1995 and 1996 nominal vertex data of H1 [26]. For display purposes we add $0.2(19-i)$ to F_2^p each time the value of x is decreased, where $i = 1, 19$. These data are not used in the global analysis.

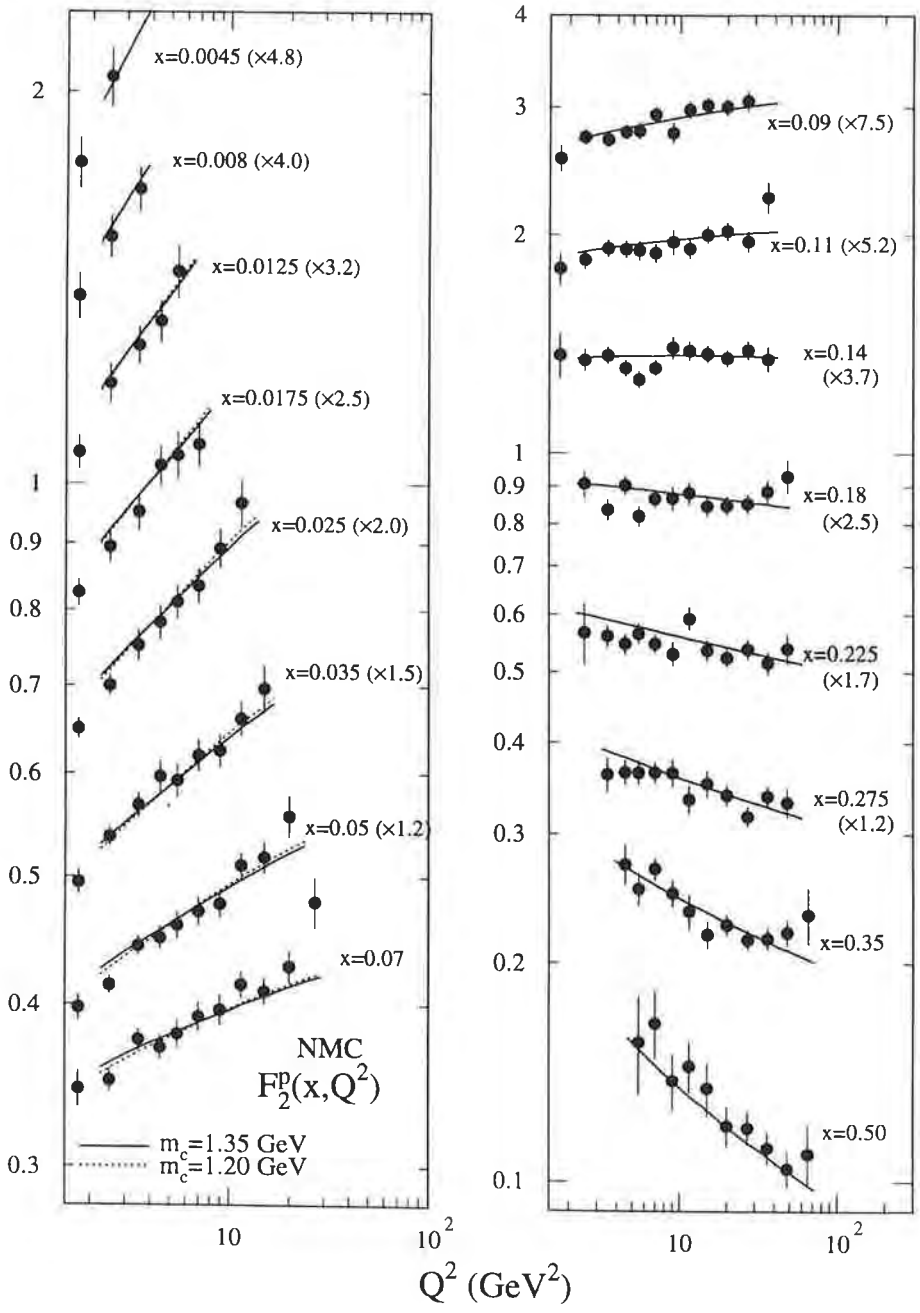

Figure 7: Description of the NMC F_2^p data [13] by the MRST partons. The effect of lowering the charm quark mass from 1.35 to 1.20 GeV is shown by the dotted curve. For display purposes we have multiplied F_2^p by the numbers shown in brackets.

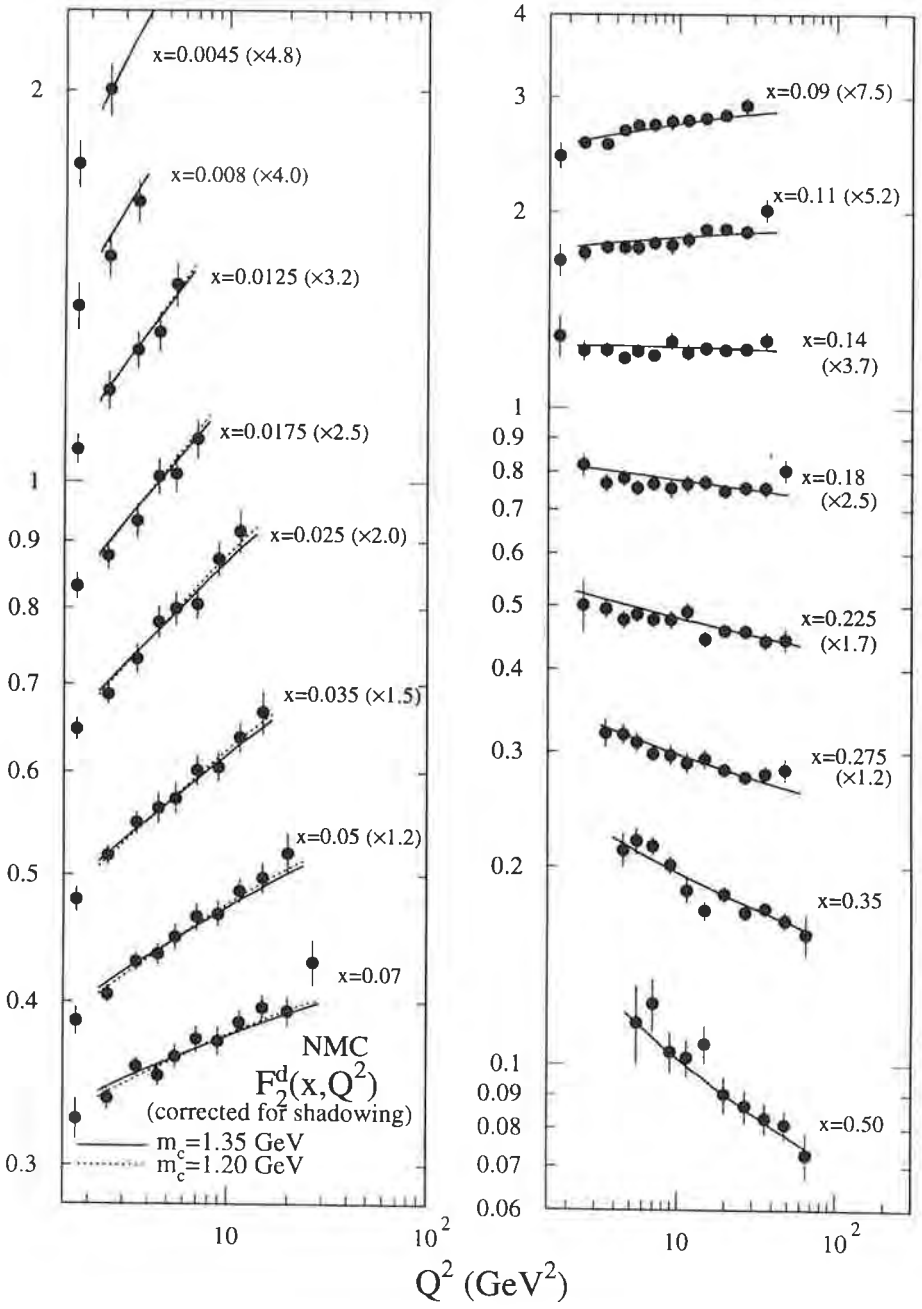

Figure 8: Comparison of F_2^d from the MRST set with the NMC deuteron data [13]. The effect of lowering the charm quark mass from 1.35 to 1.20 GeV is shown. For display purposes we have multiplied F_2^d by the numbers shown in brackets.

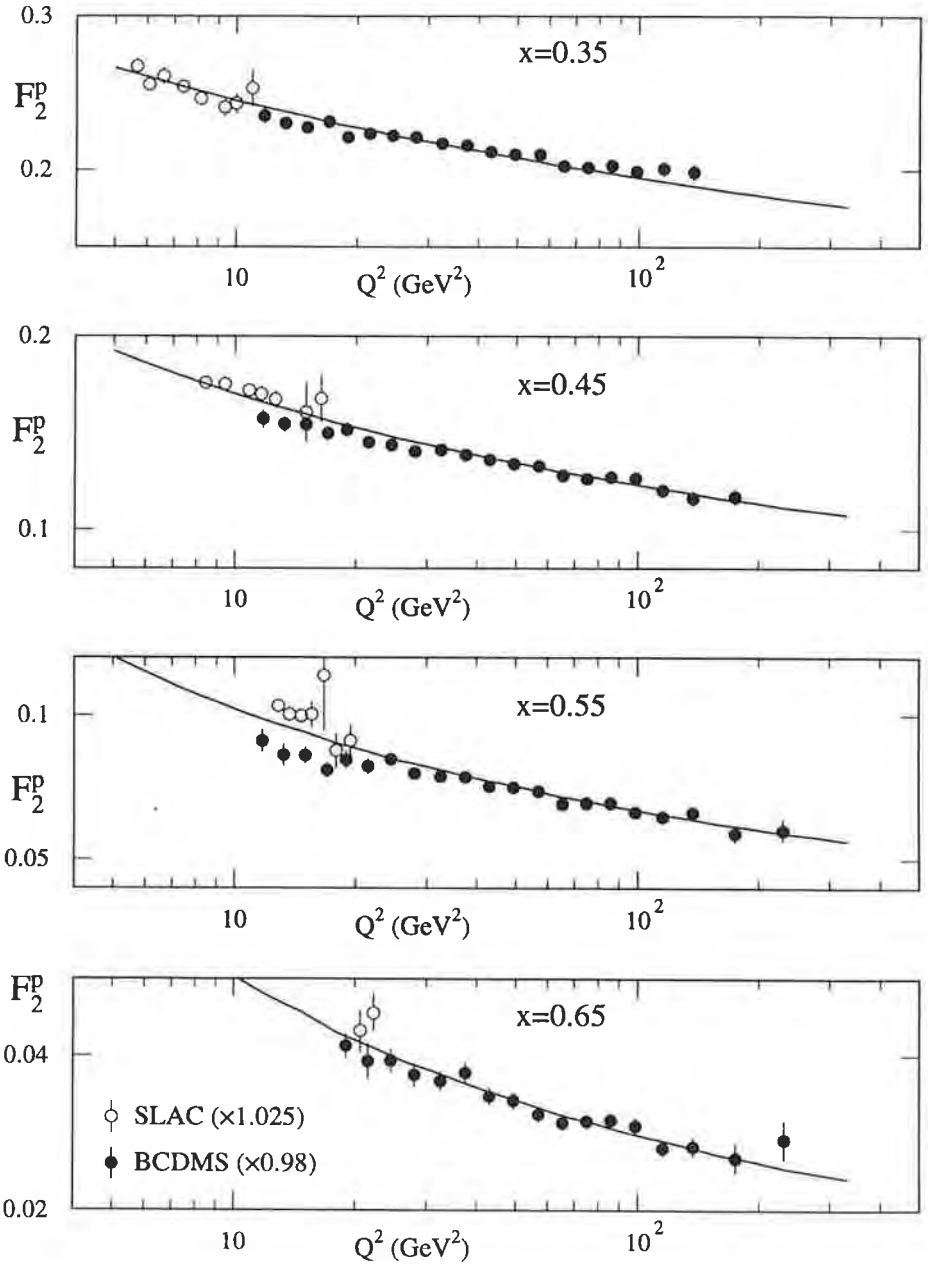

Figure 9: The description of the large x BCDMS [22] and SLAC [24] measurements of F_2^p by the MRST partons.

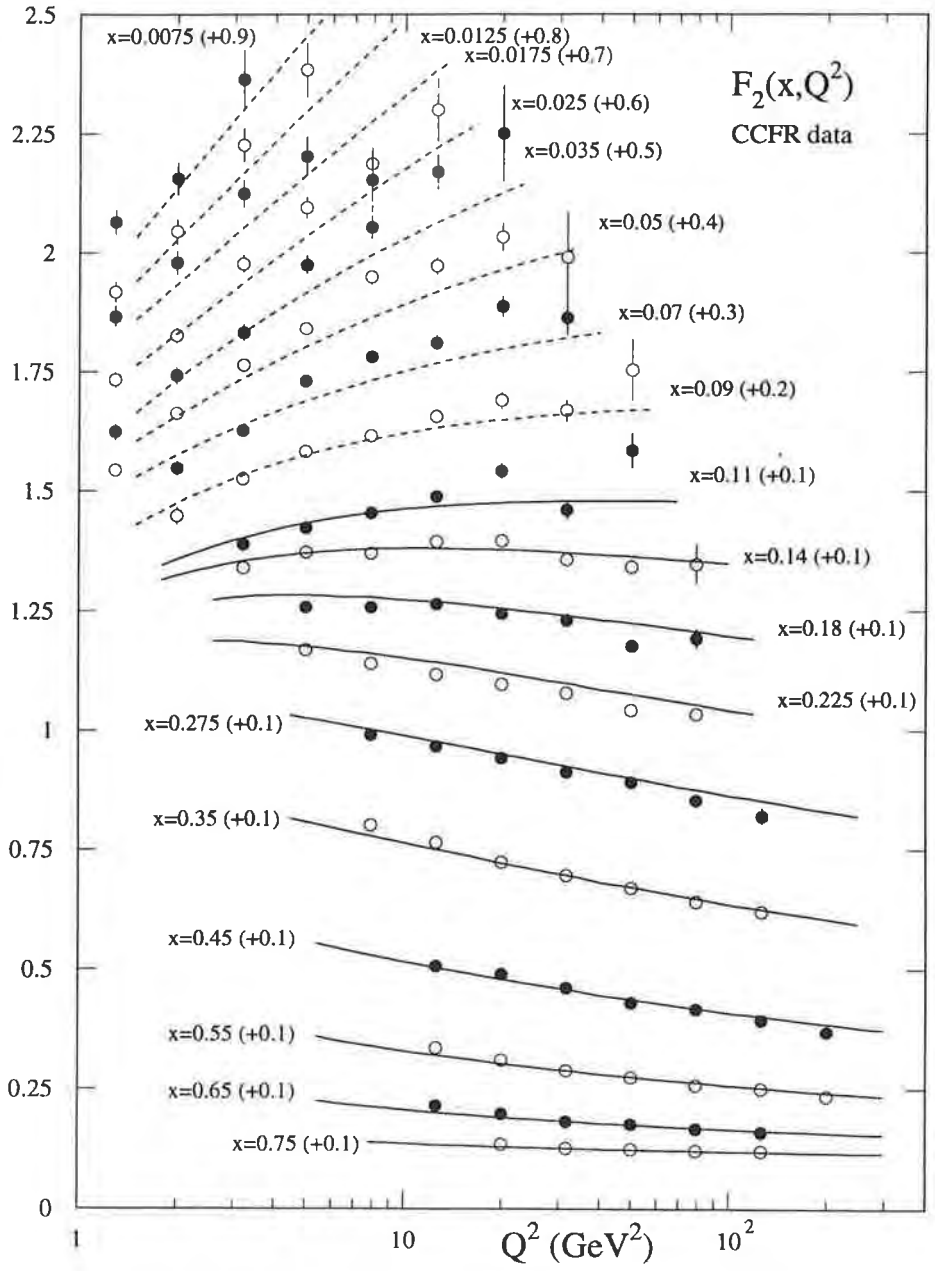

Figure 10: The description of the CCFR [3] measurements of $F_2^{\nu N}$ by the MRST partons. Only the data with $x > 0.1$ are included in the global fit. An x-dependent heavy target correction has been applied. The errors shown correspond to the quoted statistical errors together with a 1.5% uncertainty to represent the uncertainty of the heavy target correction. For display purposes we have added to $F_2^{\nu N}$ the numbers shown in brackets.

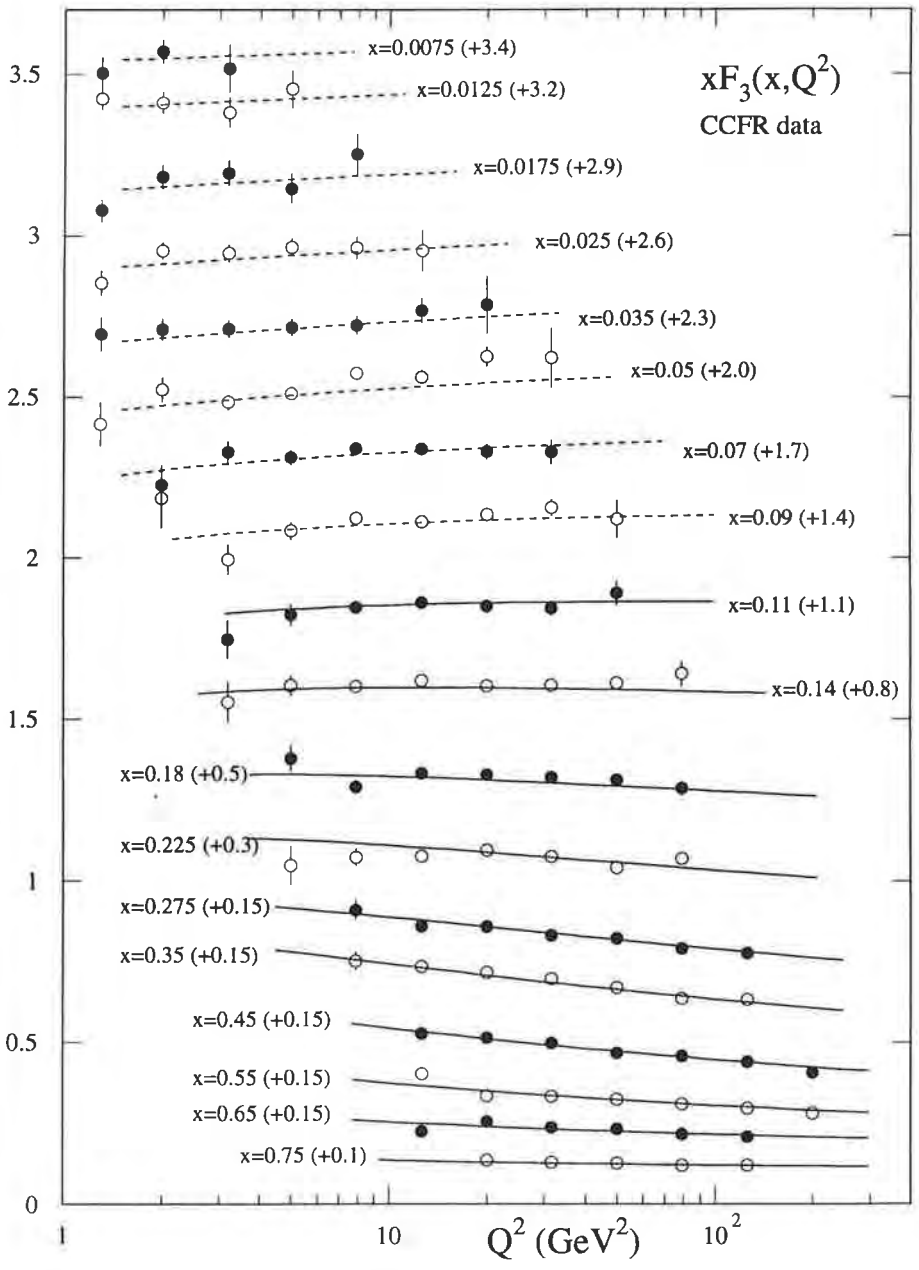

Figure 11: The same as Fig. 10 but for the structure function $xF_3^{\nu N}$.

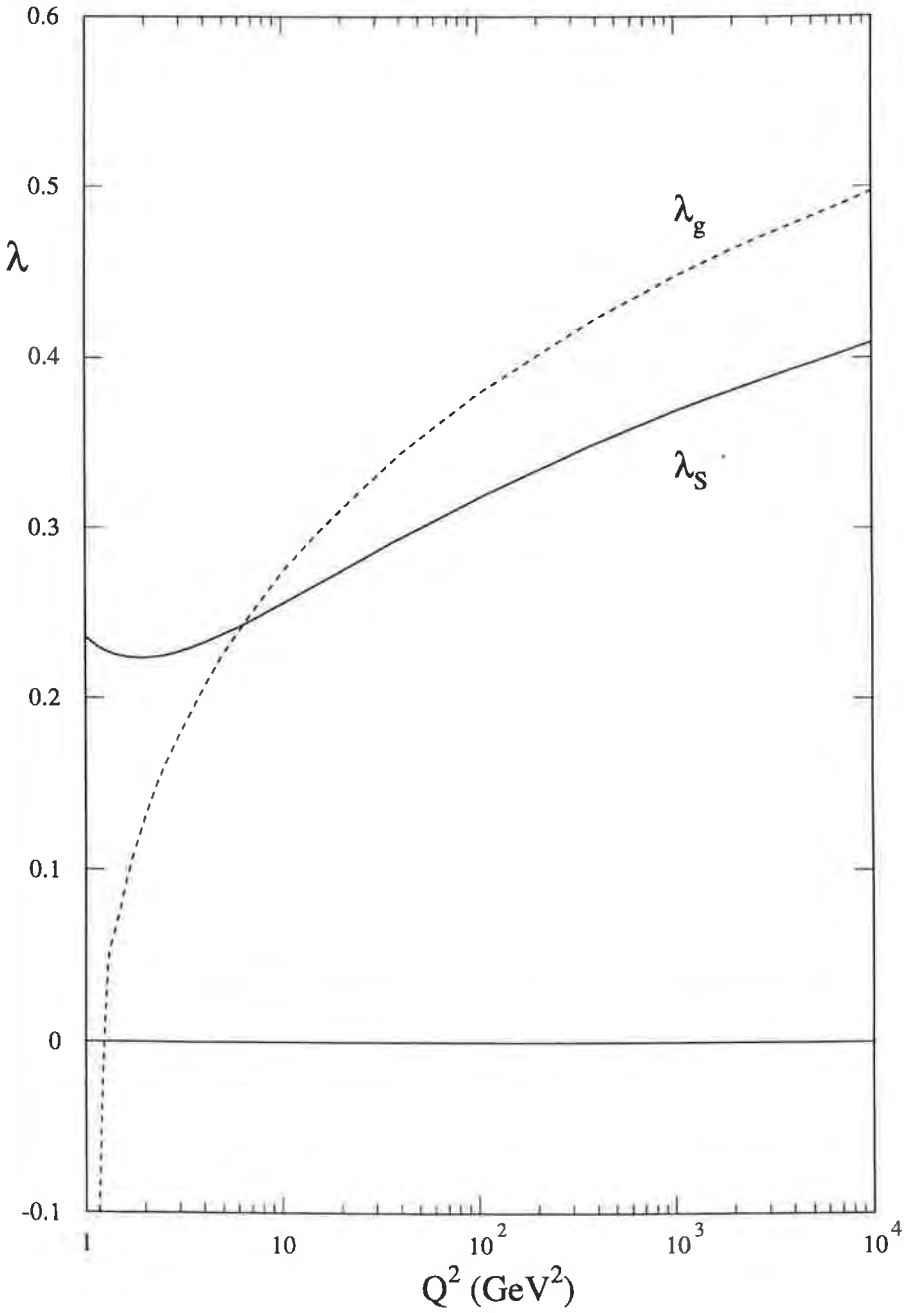

Figure 12: The effective exponents λ_S, λ_g of the small x behaviour of the sea-quark and gluon distributions of the default MRST partons versus Q^2, defined such that $xS \sim x^{-\lambda_S}$ and $xg \sim x^{-\lambda_g}$.

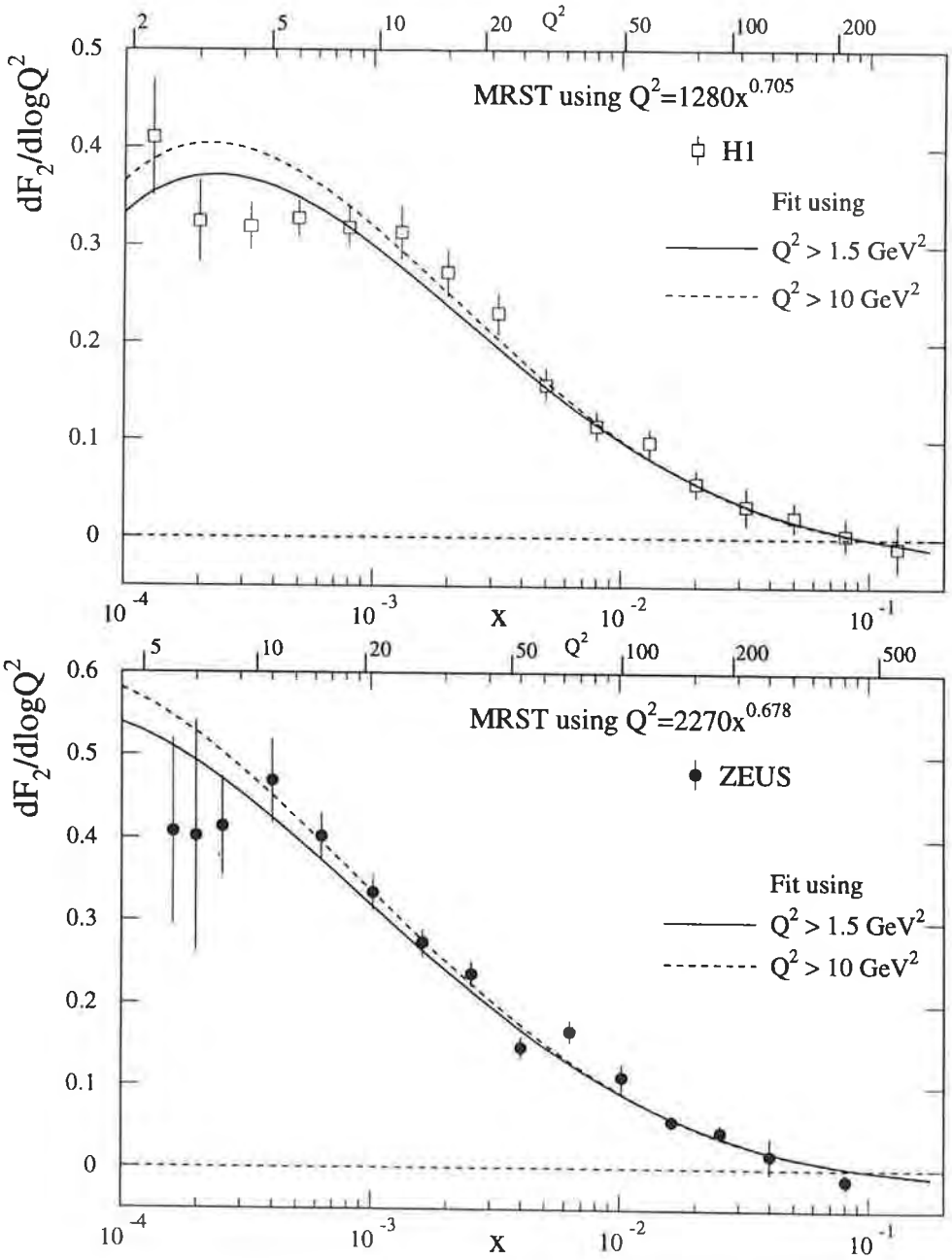

Figure 13: The description of the slopes $\partial F_2/\partial \ln Q^2$ versus x for the HERA data. The experimental points were computed from linear fits to the data in Fig. 5. The solid curve corresponds to the MRST set while the dashed line indicates the effect of removing low Q^2 data (with $Q^2 < 10$ GeV^2) from the fit. The values of Q^2 appropriate to the data are given (in GeV^2) approximately by the formulae shown and the corresponding scale is indicated on the upper edge of each plot.

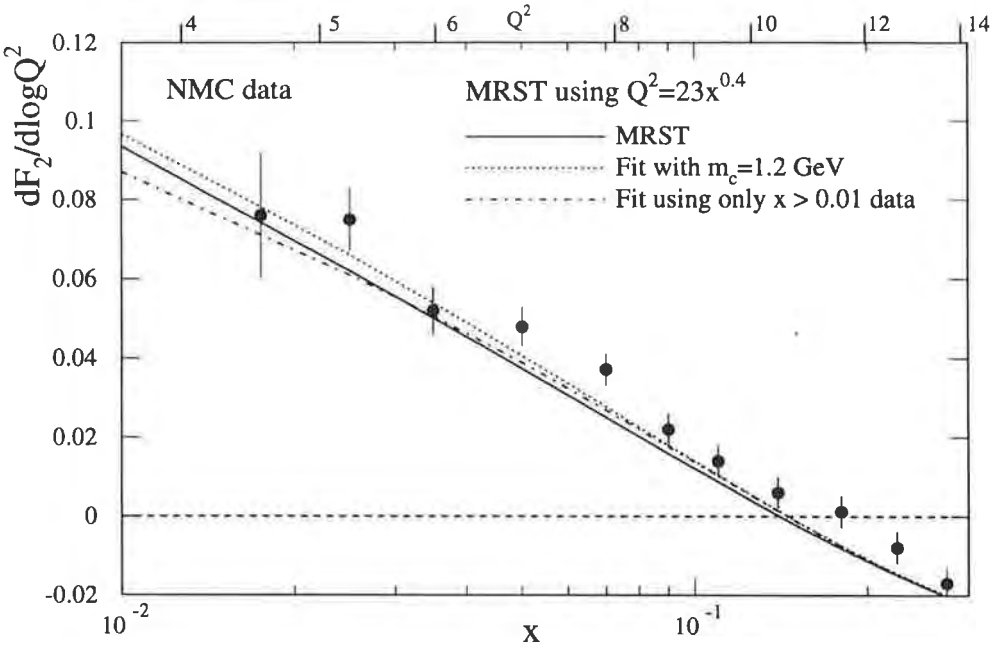

Figure 14: The continuous curve is the description of the slopes $\partial F_2/\partial \ln Q^2$ of the NMC proton data. The experimental points were computed from linear fits to the data in Fig. 7. We also show the effect of modifying the charm quark mass and of excluding low x data (with $x < 0.01$) from the global fit.

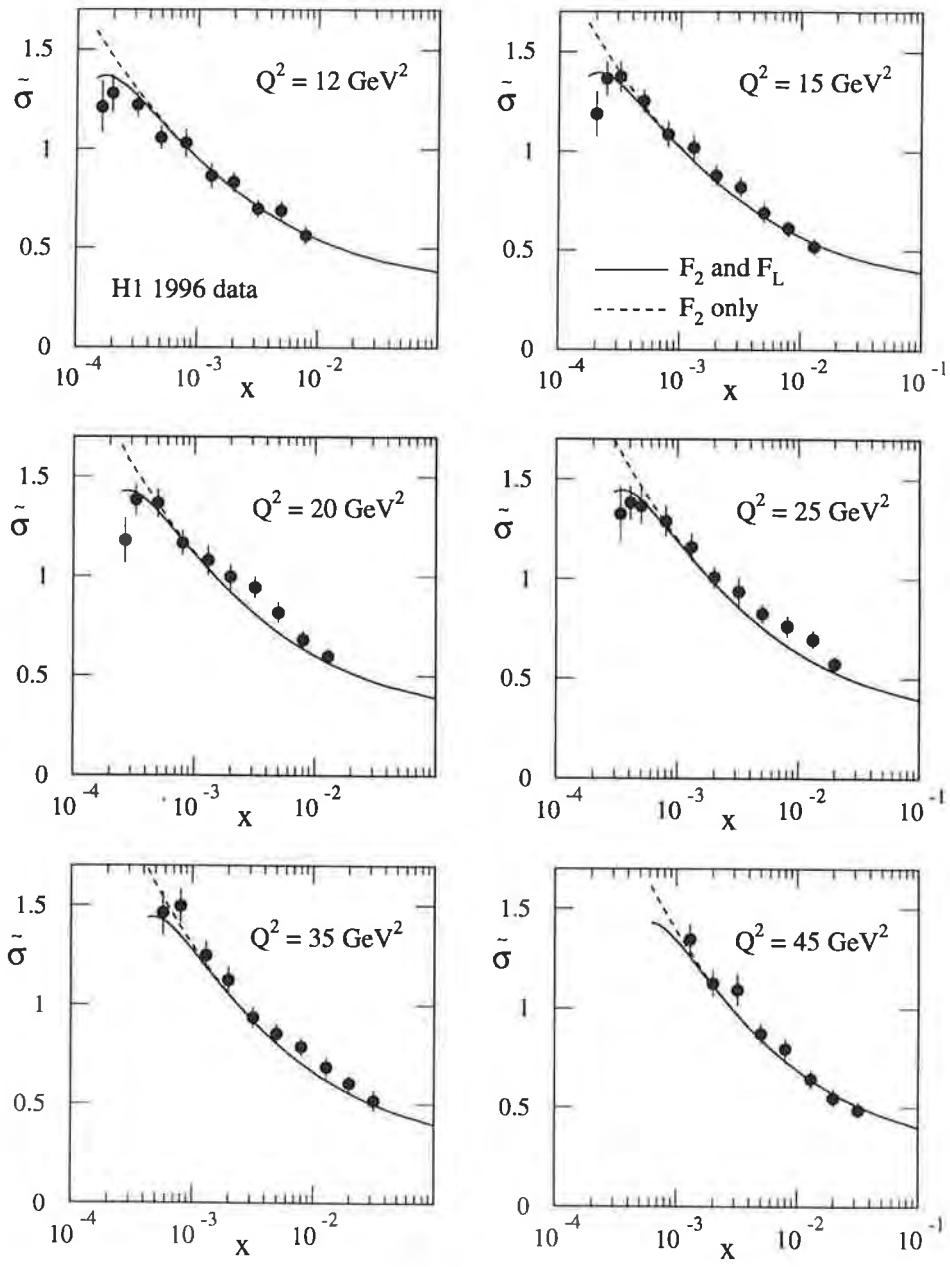

Figure 15: The description of the quantity $\tilde{\sigma} = F_2 - y^2/[1 + (1 - y)^2]F_L$ compared with the H1 1996 [26] data. Also shown (dashed curve) is the contribution to $\tilde{\sigma}$ of F_2 only.

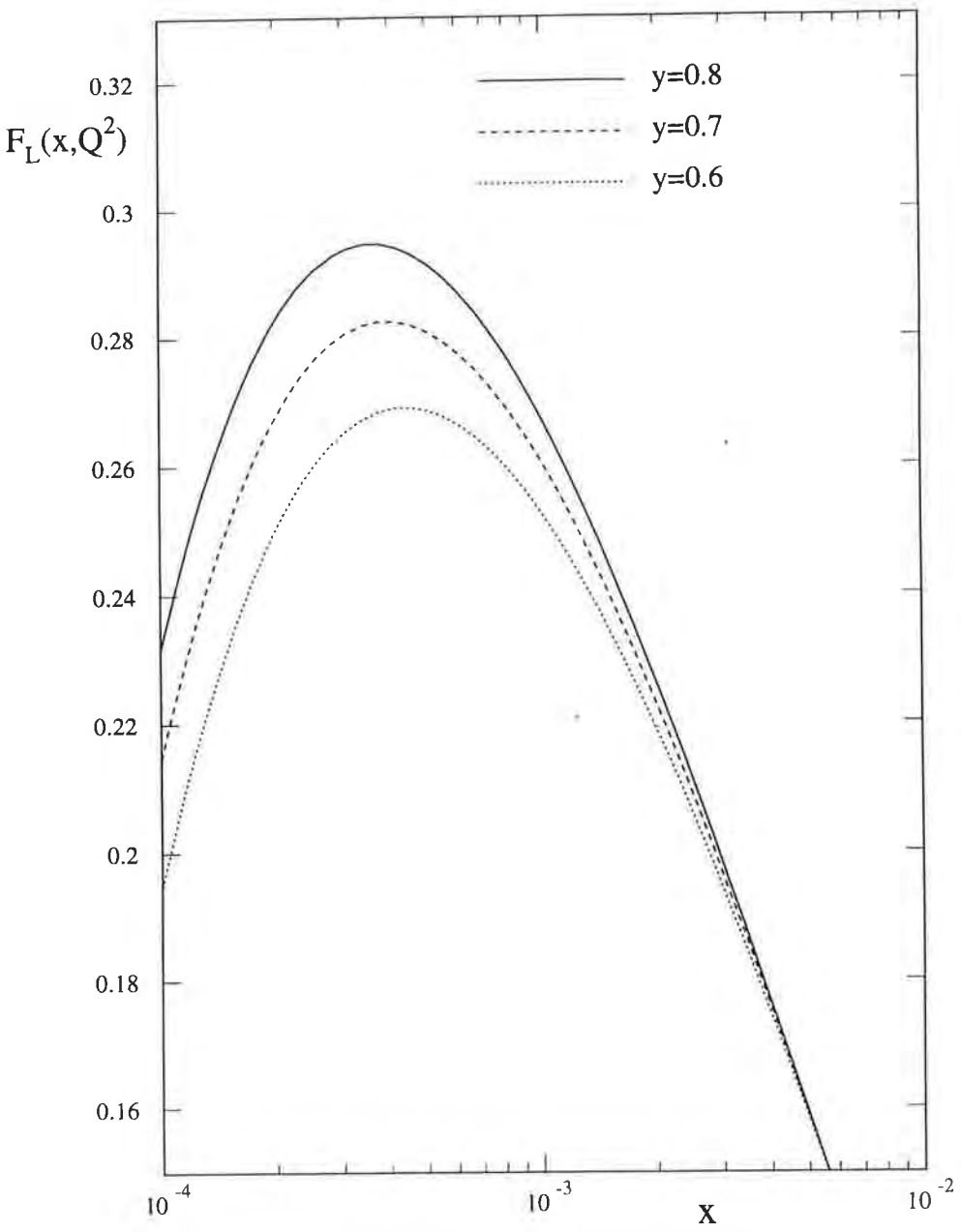

Figure 16: Prediction for F_L at HERA versus x for $y = 0.6, 0.7, 0.8$. Note that F_L has an implicit y dependence via the relation $Q^2 = xys$.

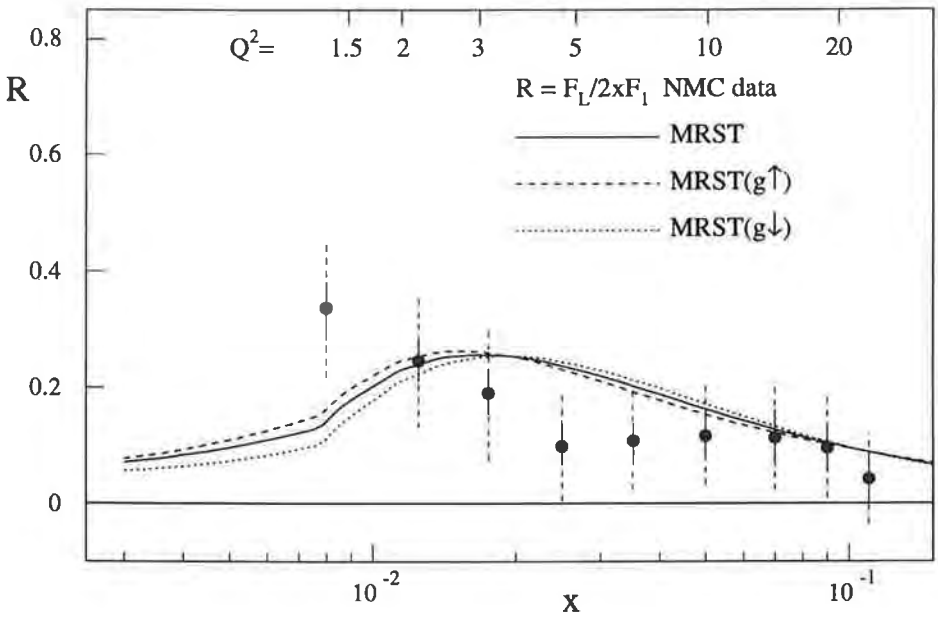

Figure 17: Comparison of the predictions for $R = F_L/2xF_1$ with the NMC [13] data. The values of Q^2 appropriate to the data are given (in GeV^2) approximately by the formula $Q^2 = 262x^{1.09}$, and the corresponding scale is indicated on the upper edge of the plot.

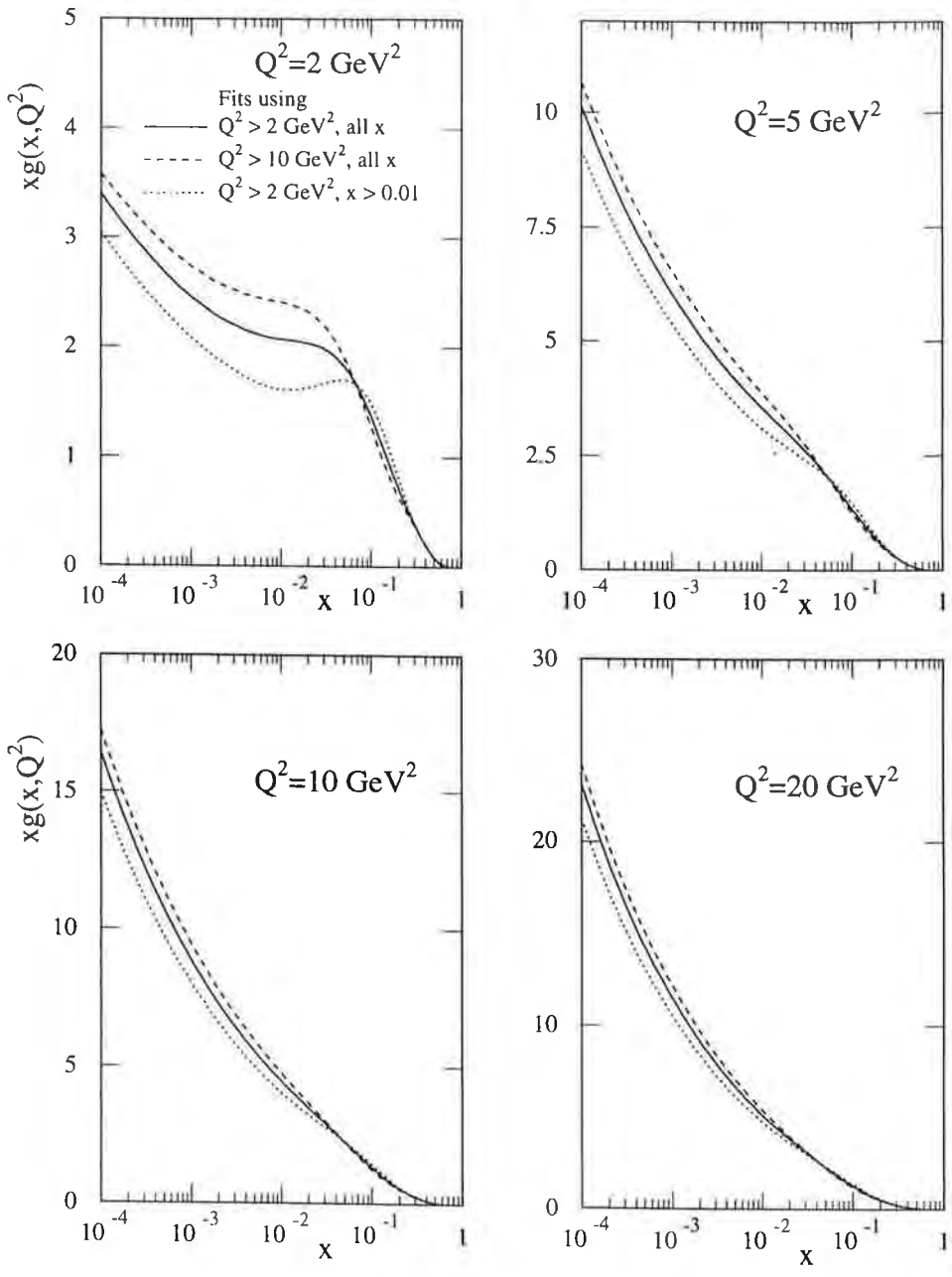

Figure 18: The gluon distributions which result from making different cuts in Q^2 and x to the data included in the fits. The cuts which we use are specified in the first plot.

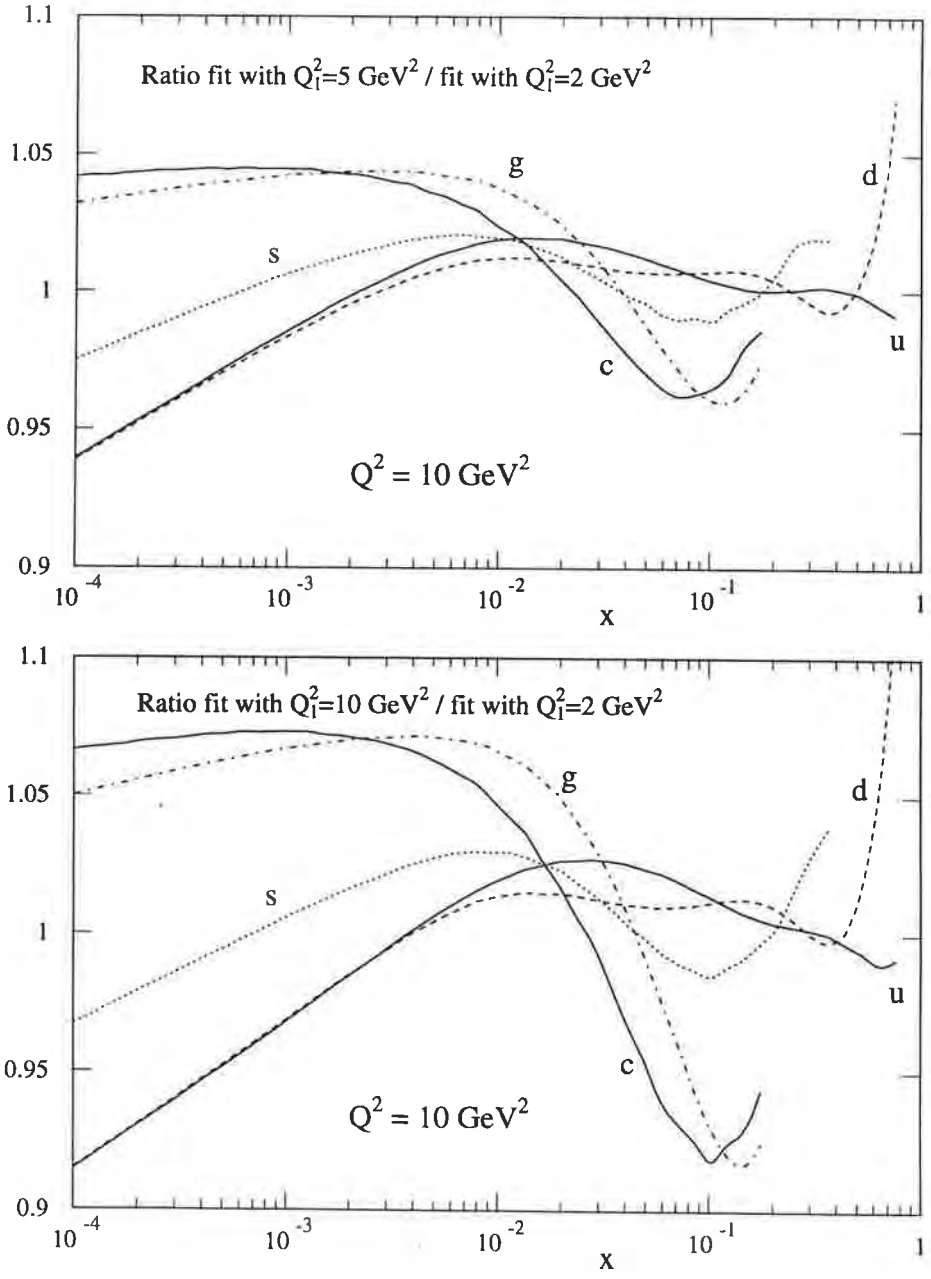

Figure 19: The parton distributions at $Q^2 = 10$ GeV^2, compared with the default MRST partons, obtained by making $Q_1^2 = 5$ GeV^2 and $Q_1^2 = 10$ GeV^2 cuts in Q^2 to the data included in the fits.

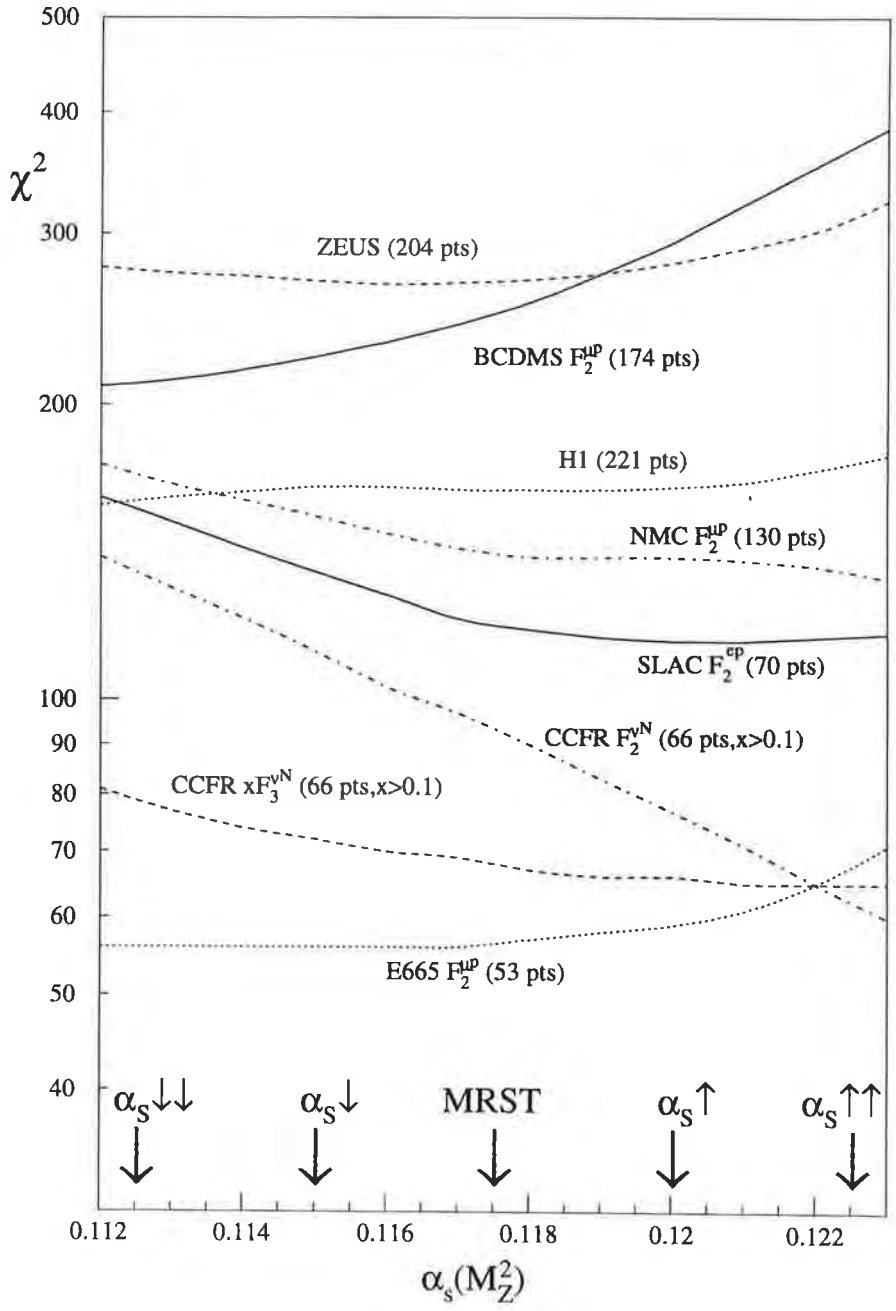

Figure 20: The contributions to the total global fit χ^2 from the various data sets as a function of α_S. The parton set corresponding to the optimum value $\alpha_S = 0.1175$ is denoted simply MRST and is the default set of partons used throughout the paper. The four other sets, which correspond to the adjacent values of α_S indicated by arrows, are used for comparison purposes. The χ^2 values for the CCFR data are obtained from the statistical error and an additional 1.5% 'systematic' error added in quadrature.

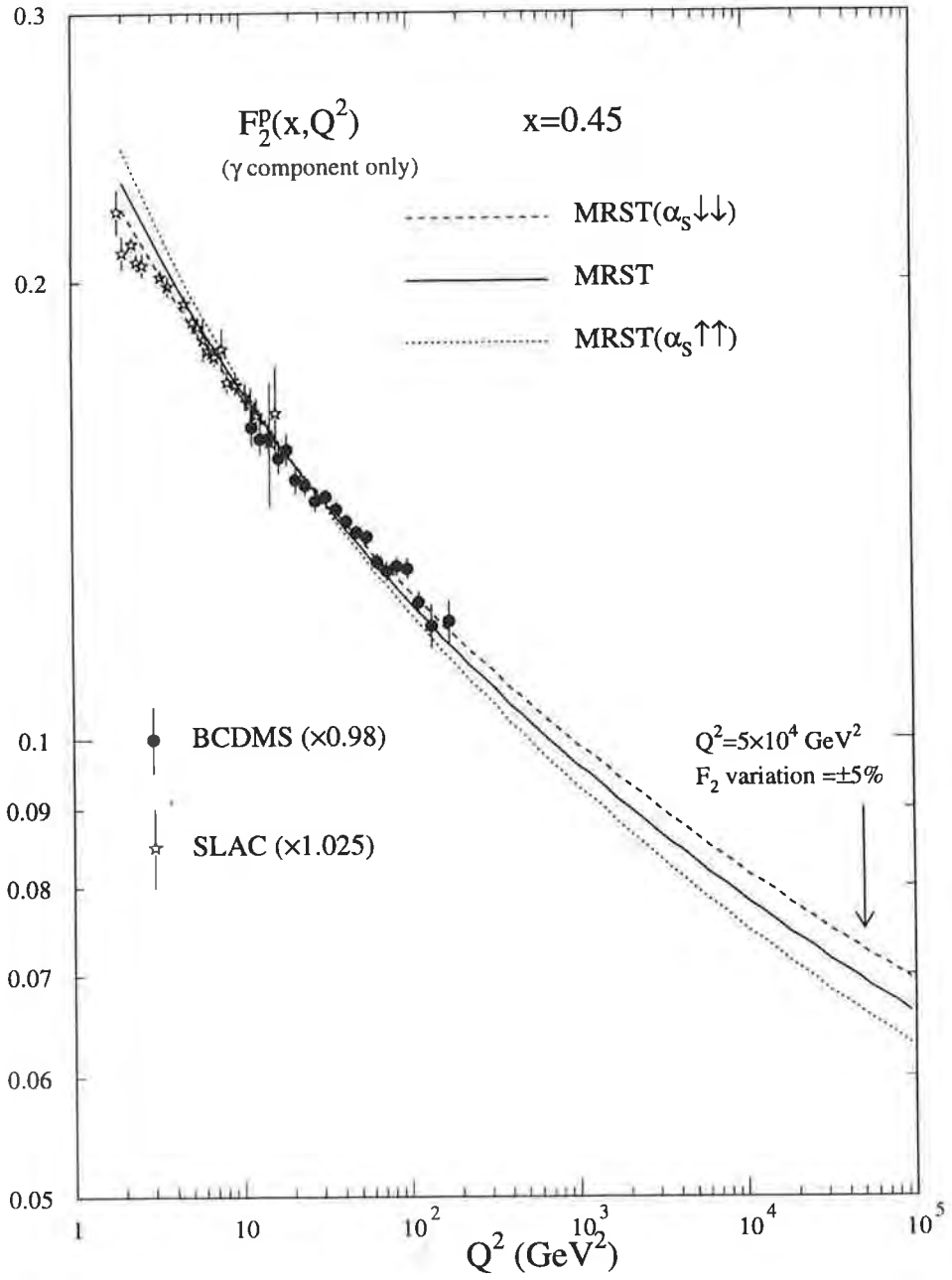

Figure 21: The extrapolation of the fits at $x = 0.45$ to high Q^2 using the MRST, MRST($\alpha_S \uparrow\uparrow$) and MRST($\alpha_S \downarrow\downarrow$) set of partons.

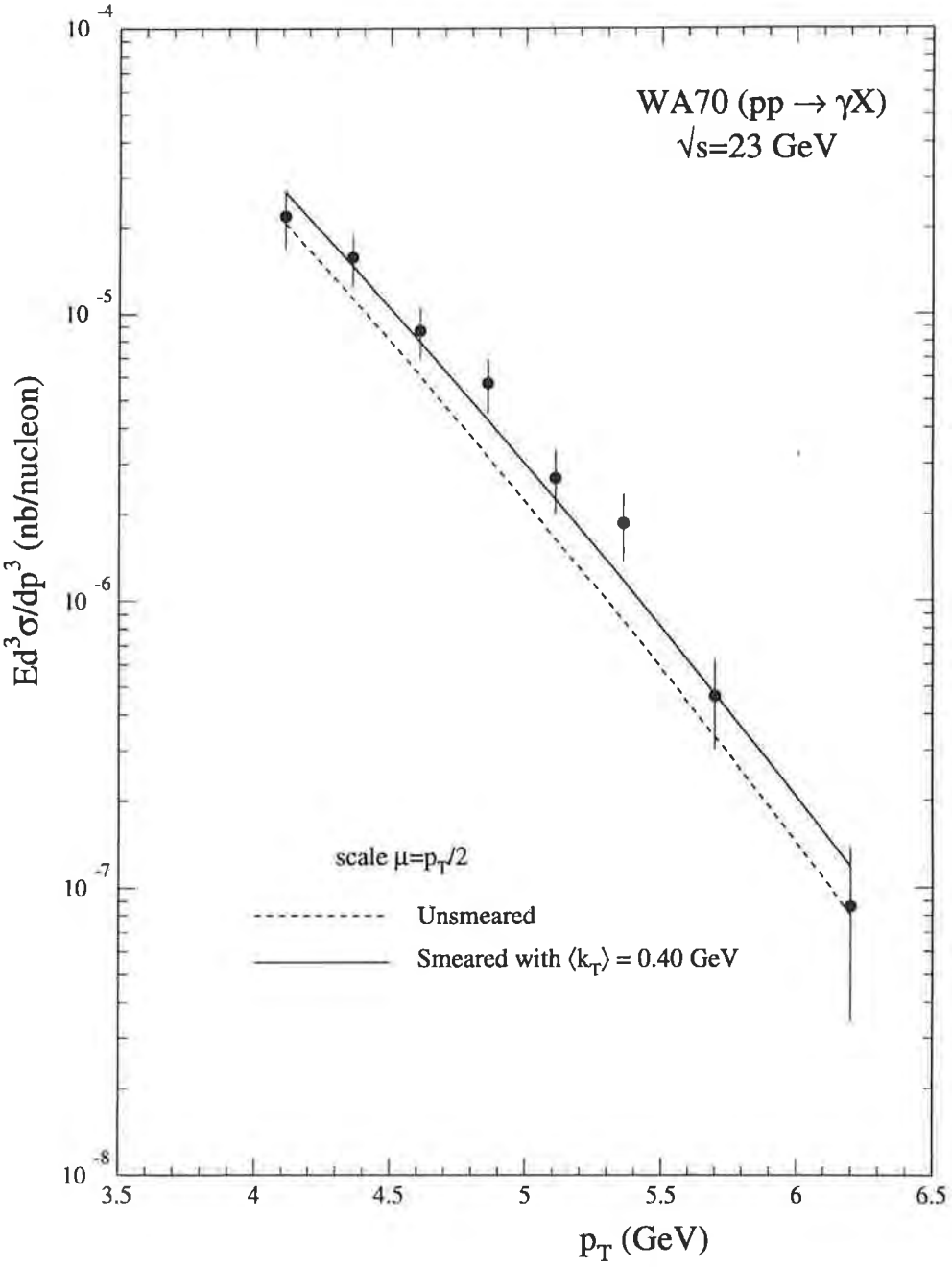

Figure 22: Comparison of the WA70 [9] data with the MRST parton set with and without smearing in transverse momentum.

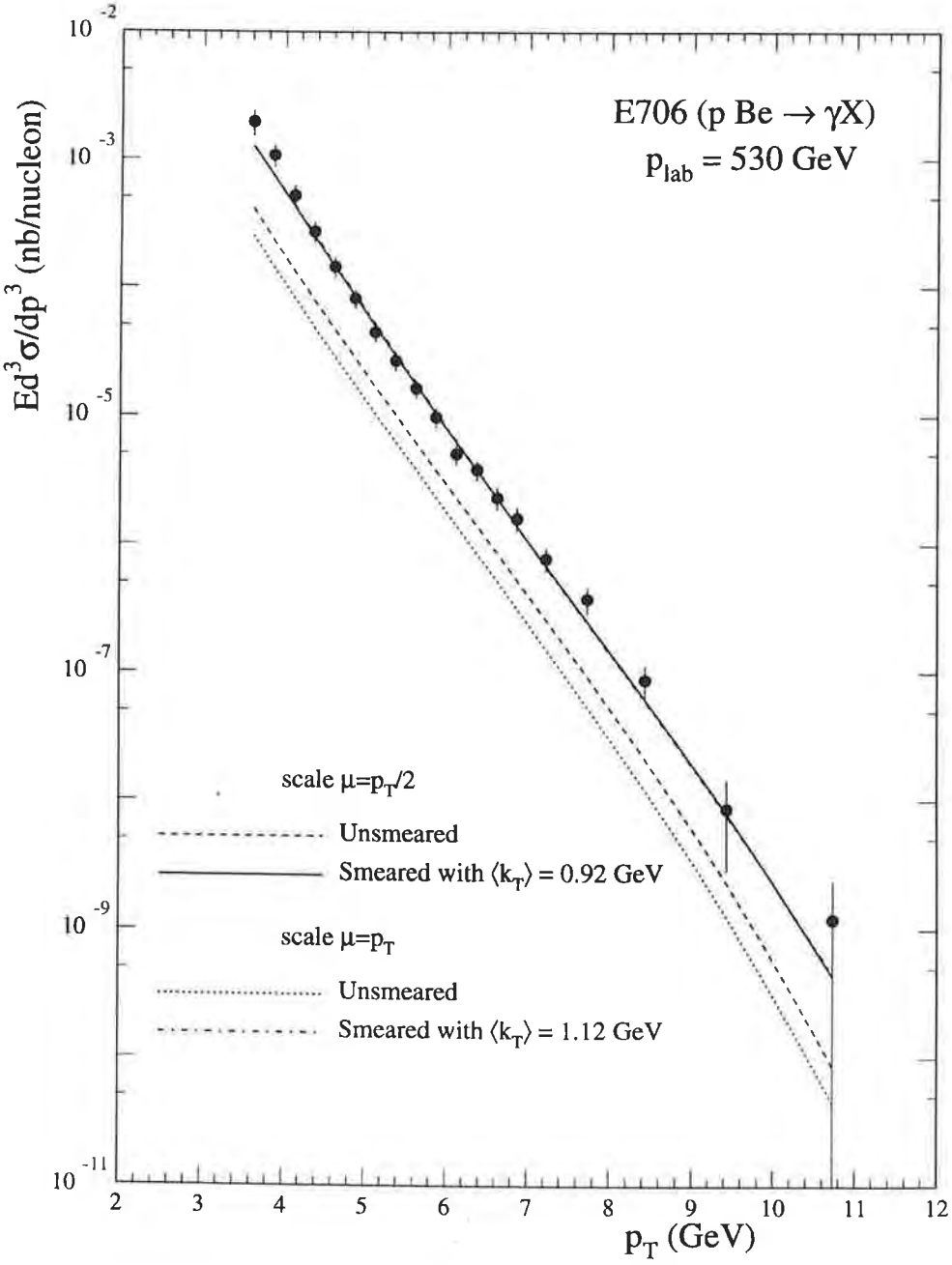

Figure 23: Comparison of the E706 [8] data at 530 GeV with the MRST parton set. The results for two choices of the factorization scale are shown, together with the improvement of the description obtained by including parton transverse momentum in each case. The two 'improved' curves lie on top of each other.

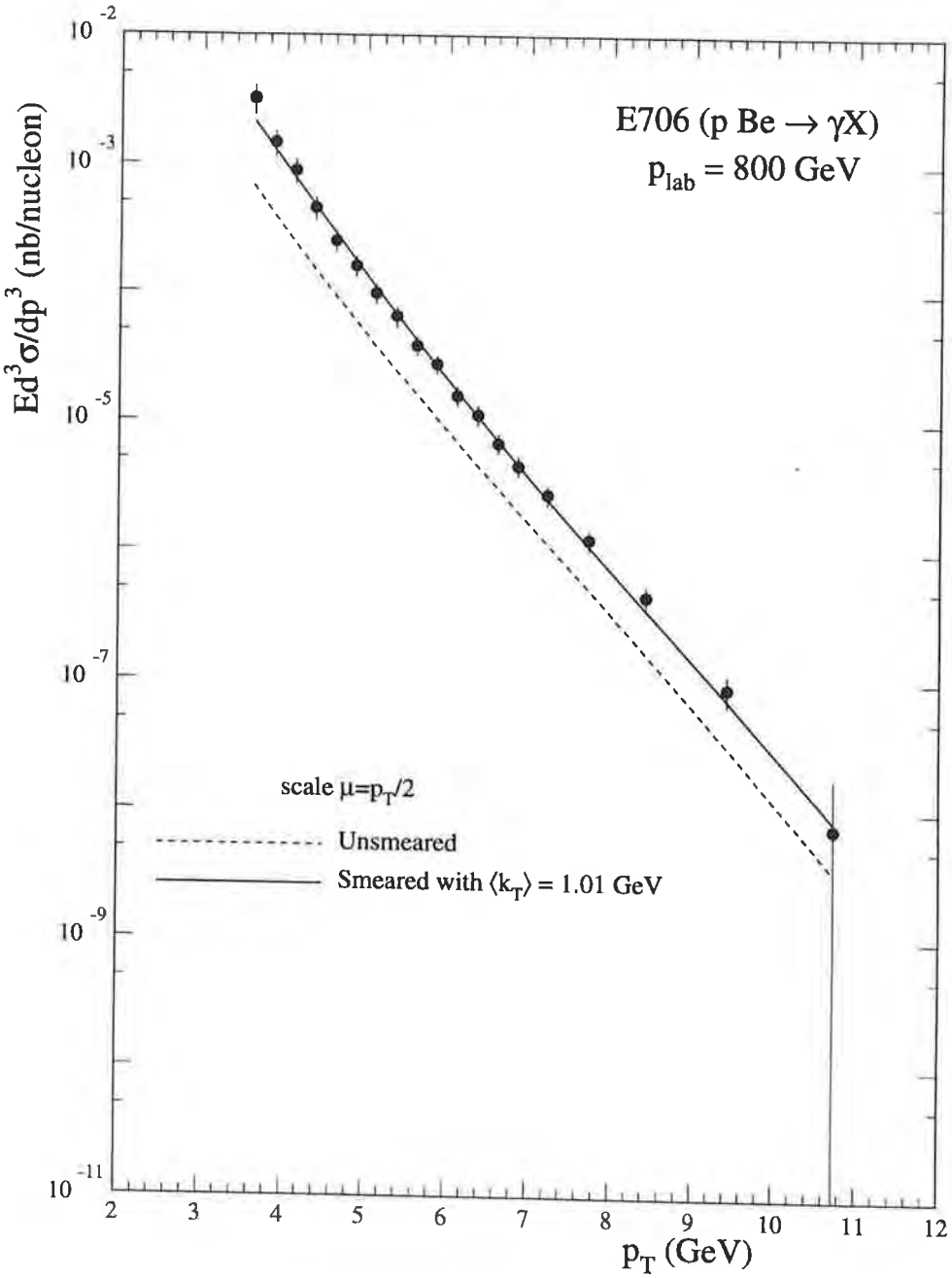

Figure 24: Comparison of the E706 [8] data at 800 GeV with the MRST parton set. The scale is chosen to be $p_T/2$ and the effect of including parton transverse momentum is shown.

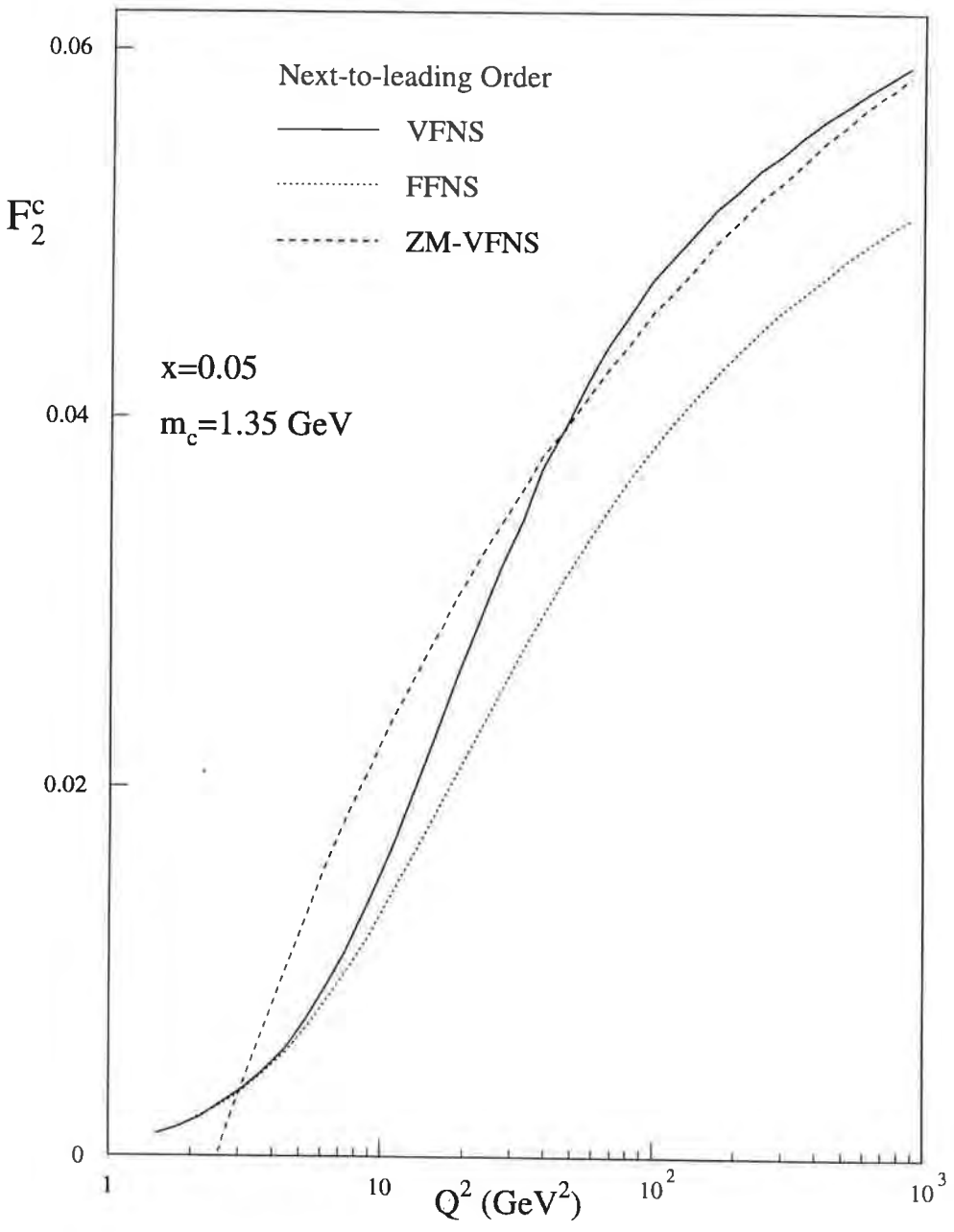

Figure 25: The continuous curve is the MRST charm structure function at $x = 0.05$ obtained using the NLO prescription and NLO evolution (VFNS). For comparison, the prescriptions of the fixed flavour number scheme (FFNS) and the zero mass scheme (ZM-VFNS) are also shown.

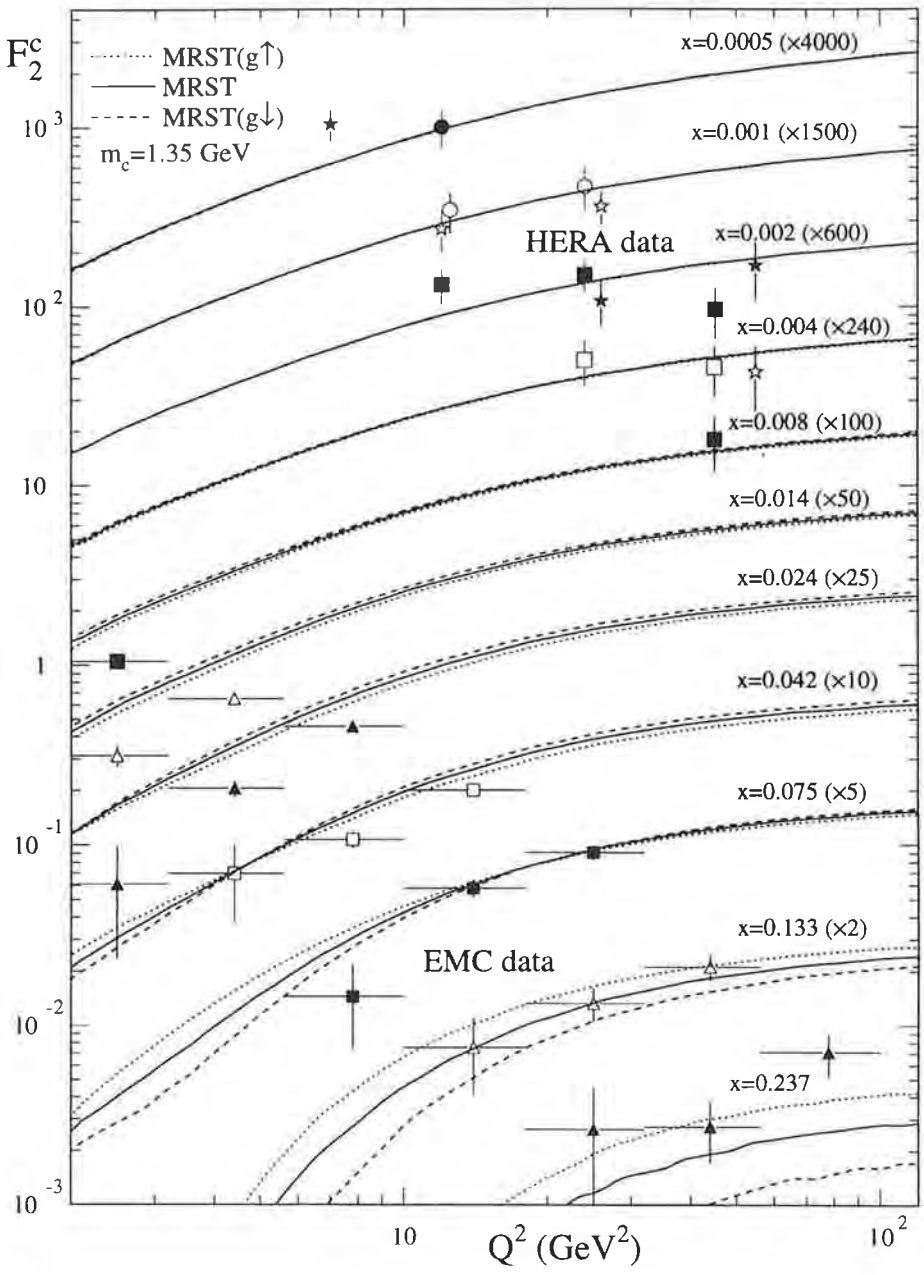

Figure 26: The prediction for the charm structure function using the three MRST parton sets characterized by the different large x gluon behaviour. The HERA data at small x are from H1 [5] and ZEUS [6], and the large x data are from EMC [7].

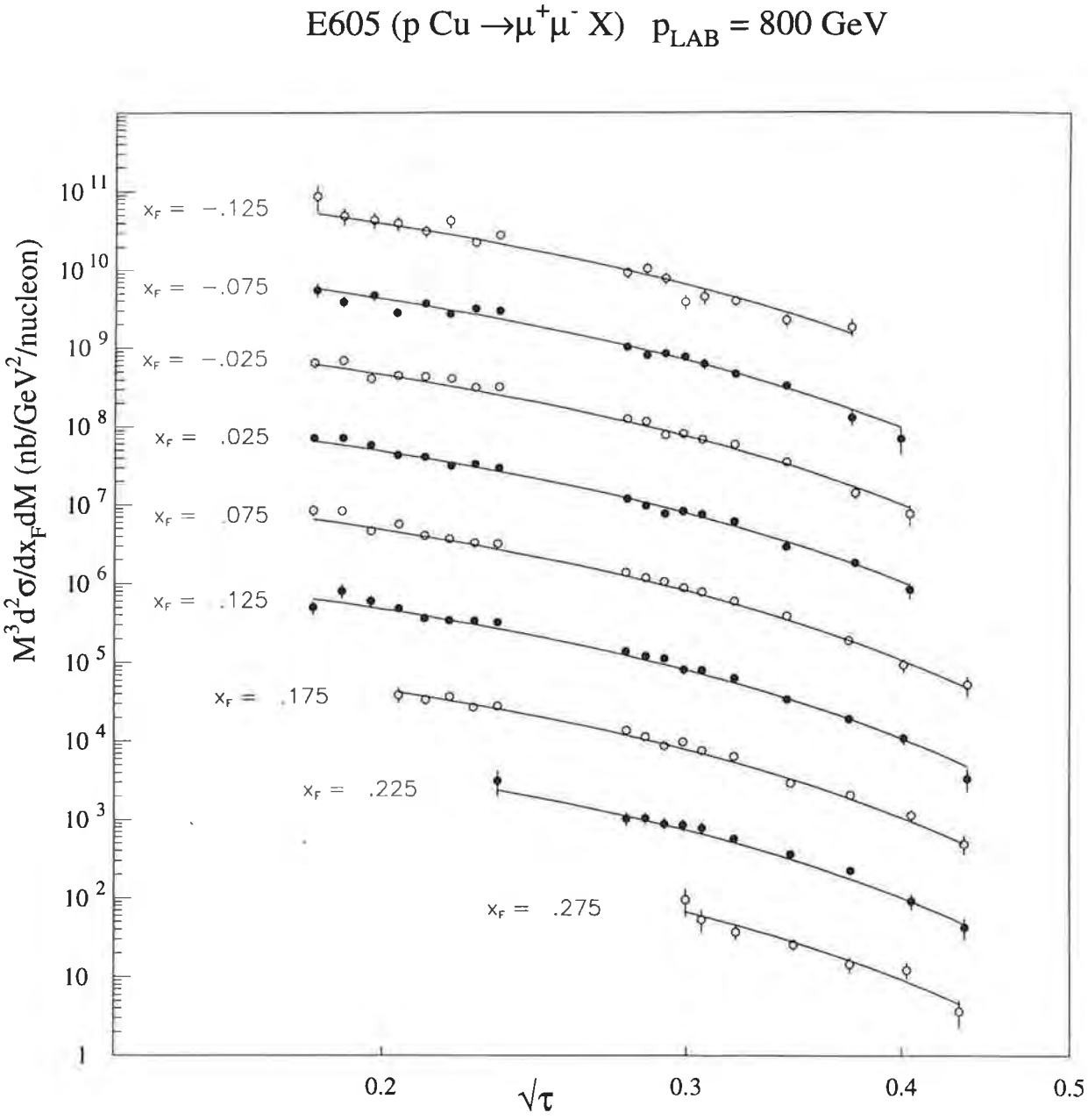

Figure 27: Hadroproduction of dileptons computed from the MRST parton set compared with the E605 data [15]. The theory curves include an additional K' factor of 0.9. No correction for the heavy target has been made. The scale on the left–hand axis is appropriate for the theory and data at $x_F = -0.125$. For display purposes the normalization is then decreased by a factor of ten for each step upwards in x_F.

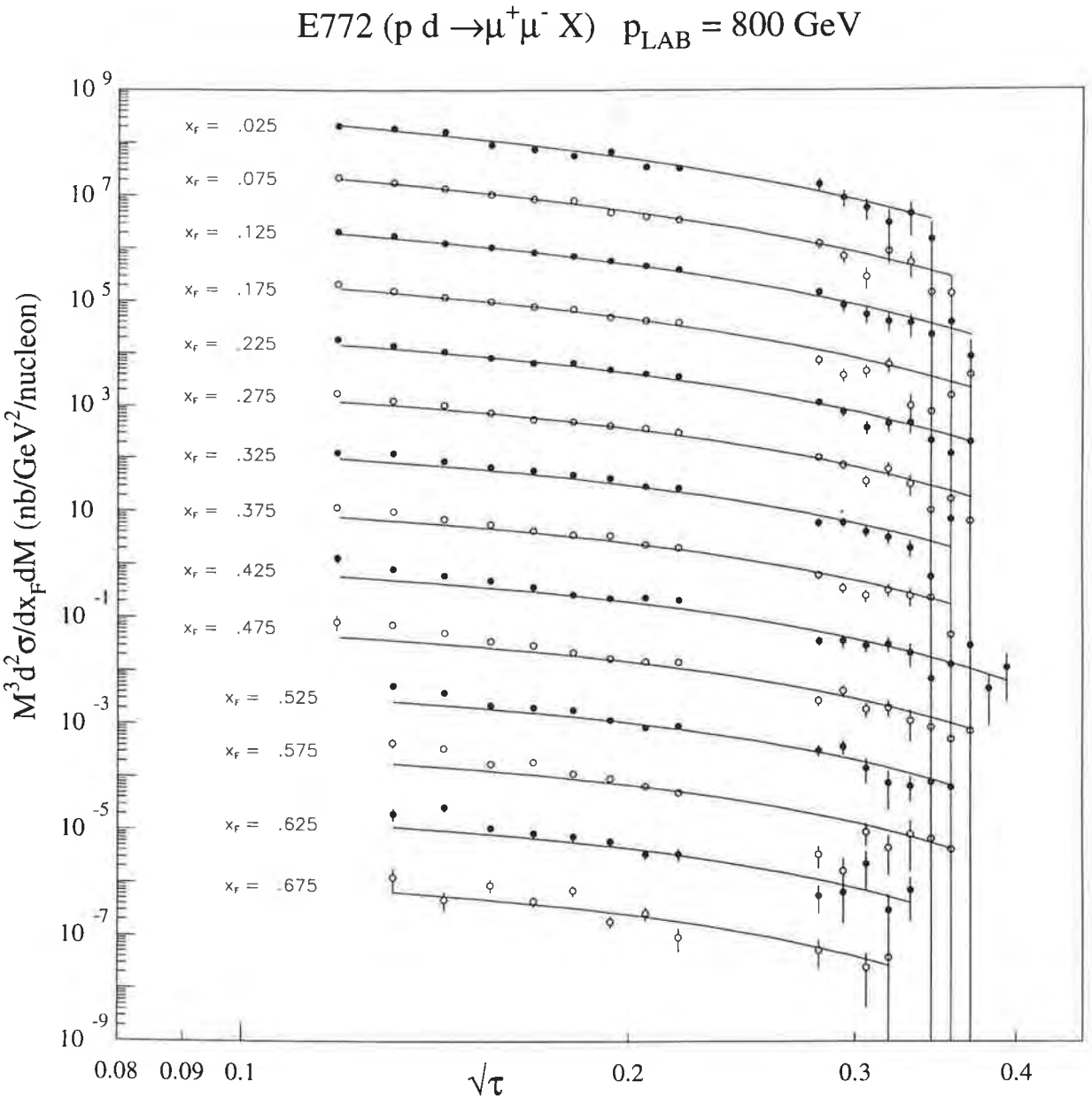

Figure 28: Hadroproduction of dileptons computed from the MRST parton set compared with the E772 data [14]. The theory curves include an additional K' factor of 0.96. The scale on the left-hand axis is appropriate for the theory and data at $x_F = 0.025$. For display purposes the normalization is then decreased by a factor of ten for each step upwards in x_F.

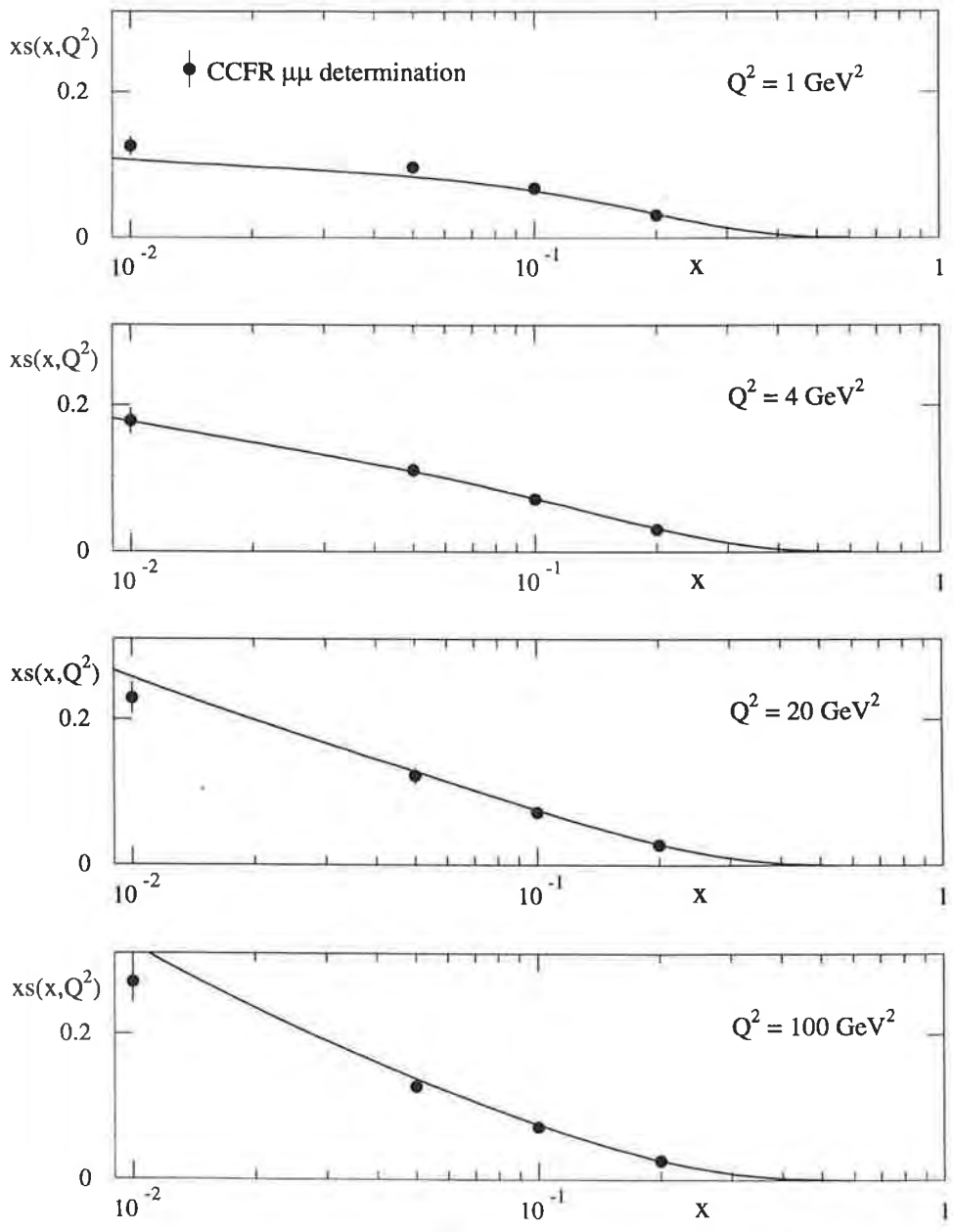

Figure 29: Comparison of the strange quark distribution from the MRST set of partons compared with the determination of the strange sea obtained by the CCFR collaboration [16] in a NLO analysis of their data on the neutrino production of dimuons.

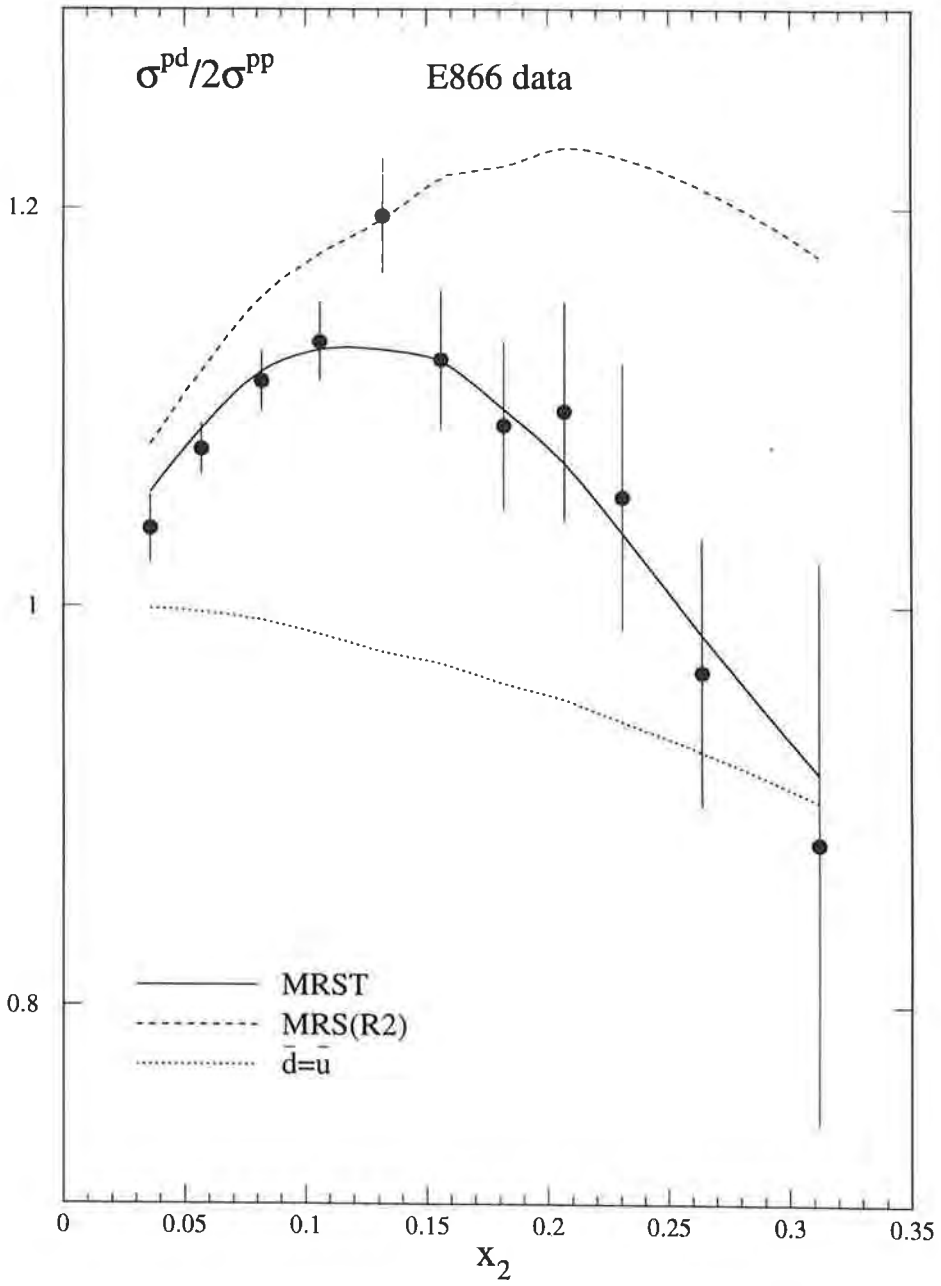

Figure 30: The continuous curve is the MRST description of the E866 [10] data for the ratio of the cross sections for hadroproduction of dileptons for proton and deuterium targets versus x_2, the fractional momentum of the parton in the target. The other curves are for comparison only.

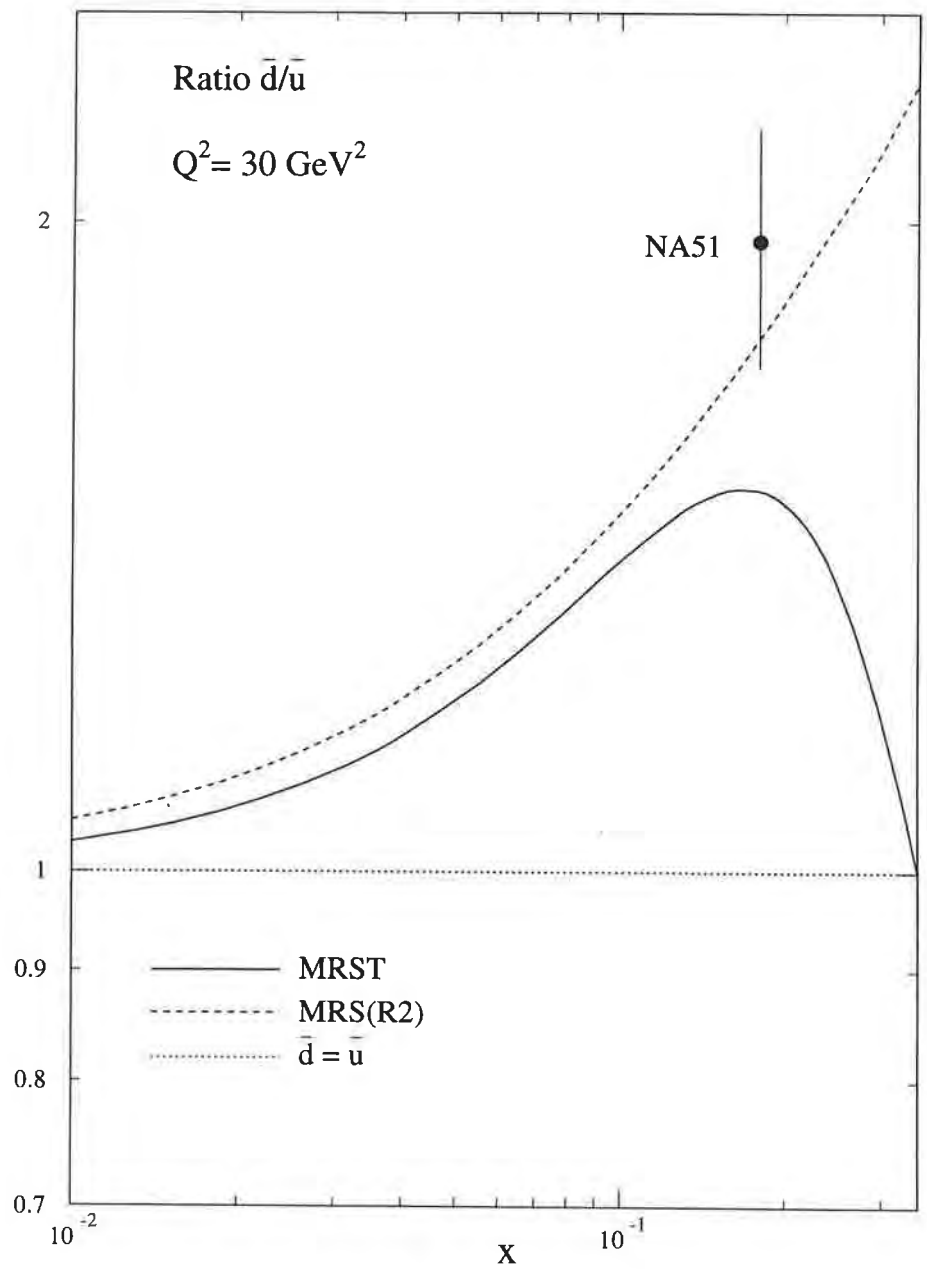

Figure 31: The ratio of the parton distributions $\bar{d}/\bar{u}$ at $Q^2 = 30$ GeV^2 for the MRST and MRS(R2) parton sets compared to the estimate from the NA51 [11] measurement of the Drell-Yan asymmetry.

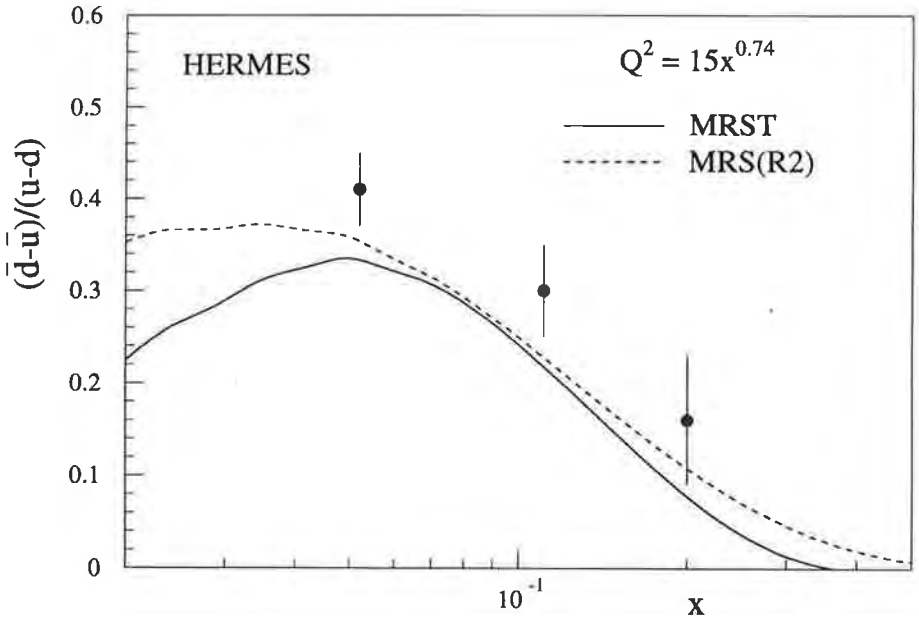

Figure 32: Predictions for the ratio $(\bar{d} - \bar{u})/(u - d)$ from the parton sets MRST and MRS(R2) compared with the preliminary estimates obtained by the HERMES collaboration [50] from their measurements of semi-inclusive pion production in DIS. Note that there is an additional overall systematic error on the data of ± 0.07. The Q^2 values of the data vary with x approximately according to the formula Q^2 (GeV^2) $= 15x^{0.74}$.

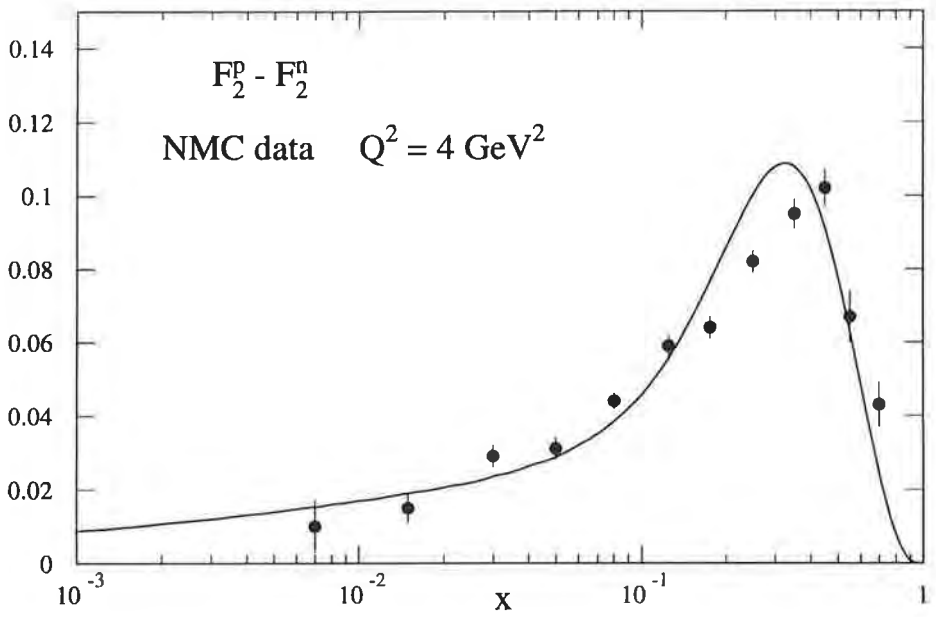

Figure 33: The MRST description of the difference $F_2^p - F_2^n$ at $Q^2 = 4$ GeV^2 compared with the measurements from NMC [51].

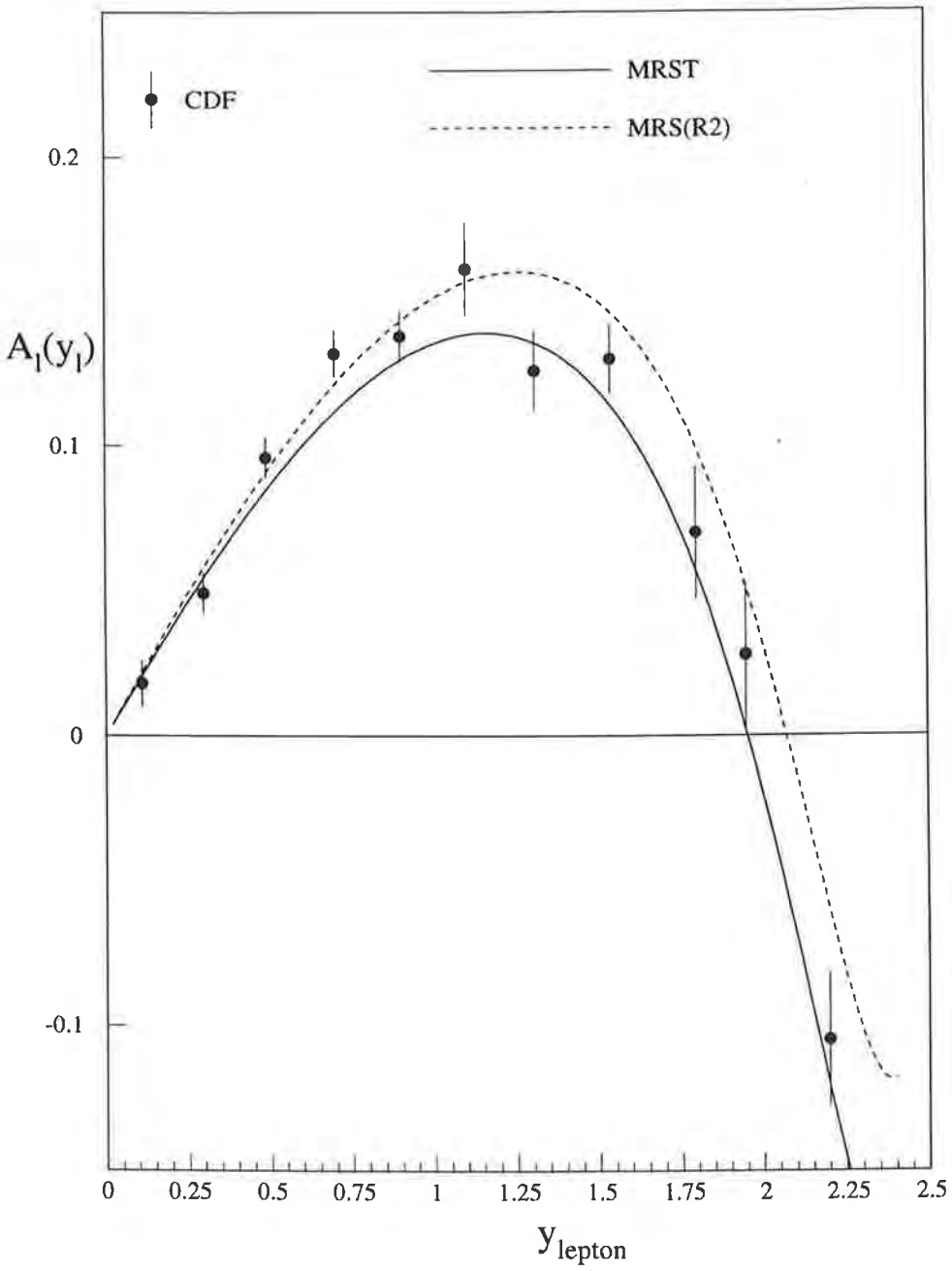

Figure 34: The description of the lepton asymmetry for $W^{\pm}$ production in $\bar{p}p$ collisions at $\sqrt{s}$ = 1.8 TeV. The data from CDF [12] are compared with the new MRST parton set and with the previous set MRS(R2).

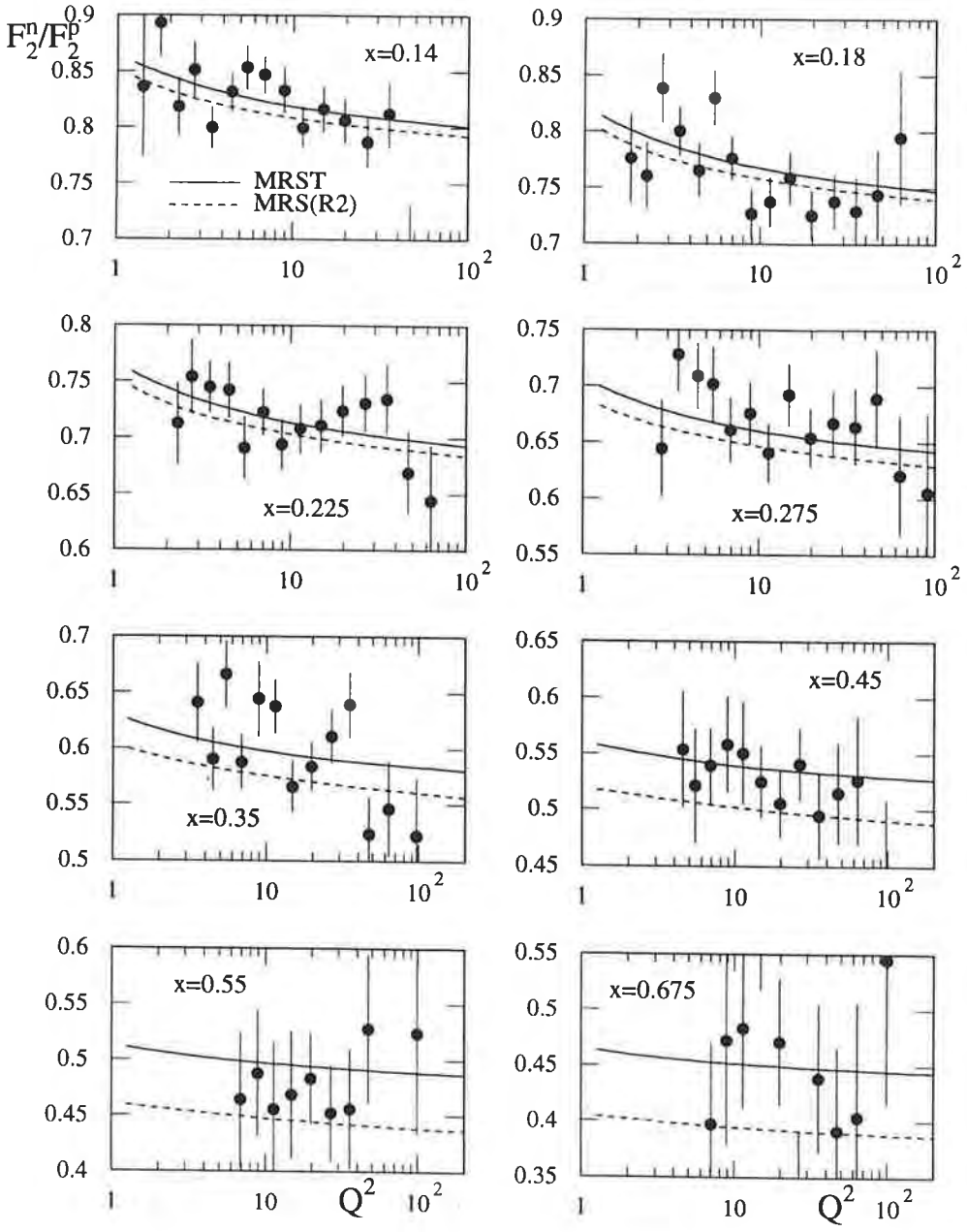

Figure 35: The large x data on the ratio F_2^n/F_2^p extracted from the measurements of F_2^d/F_2^p by NMC [13] compared with the MRST and MRS(R2) descriptions.

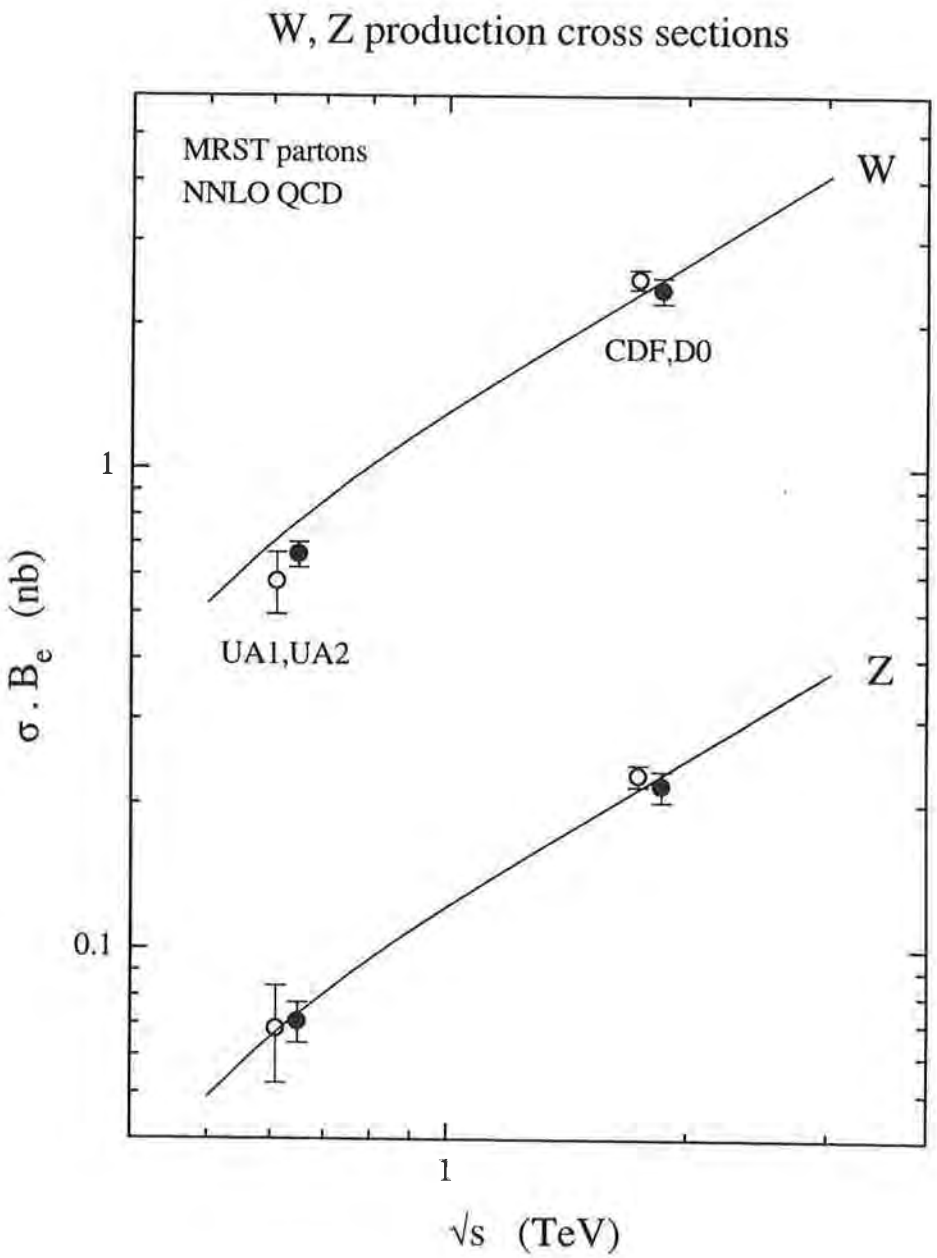

Figure 36: Total W, Z production cross sections times leptonic branching ratios as a function of the $(p\bar{p})$ collider energy $\sqrt{s}$, calculated using the default MRST partons. Experimental measurements from UA1 [58], UA2 [59], CDF [60] and D0 [61] are also shown.

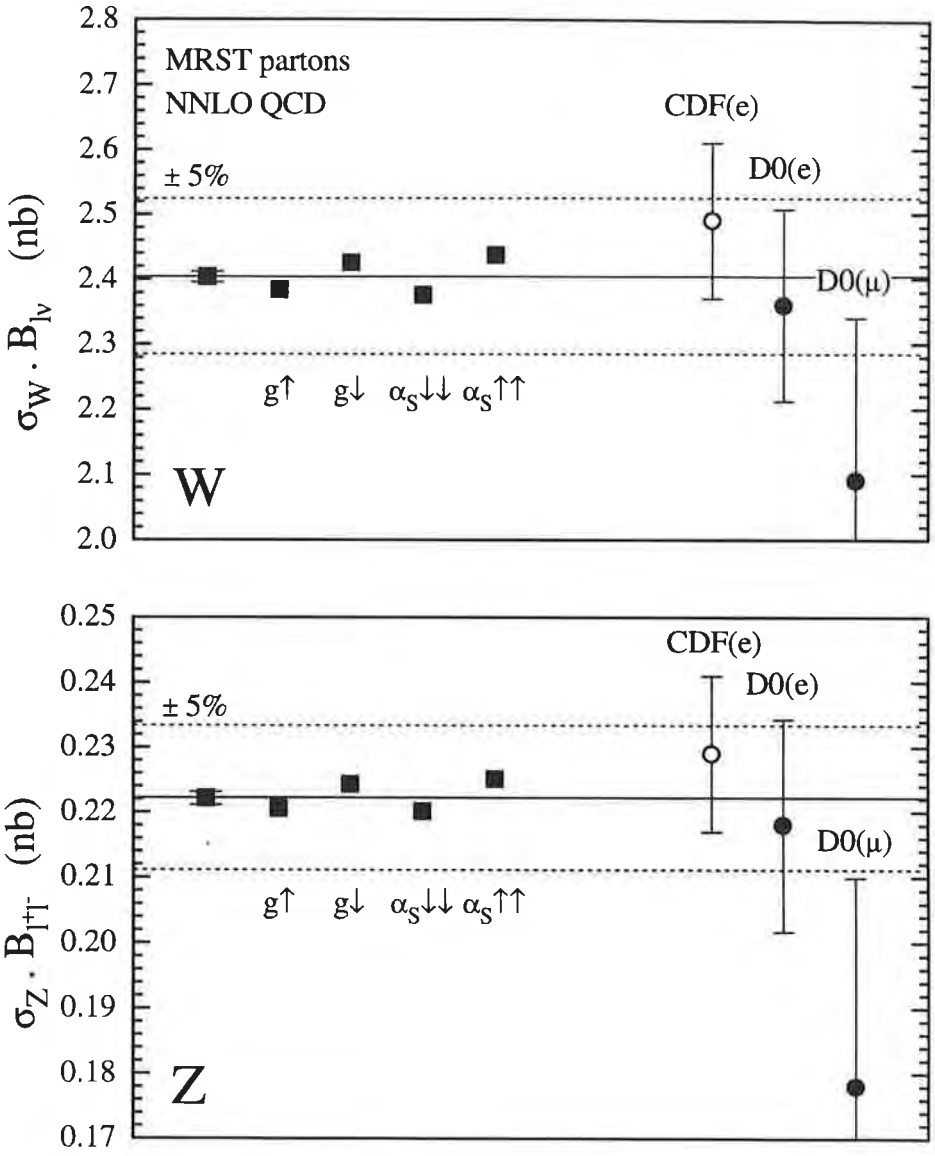

Figure 37: Predictions for the W and Z production cross sections times leptonic branching ratios in $p\bar{p}$ collisions at 1.8 TeV using the five MRST parton sets. The error bars on the default MRST prediction correspond to a scale variation of $\mu = M_V/2 \to 2M_V$, $V = W, Z$. Experimental measurements from CDF [60] and D0 [61] are shown.

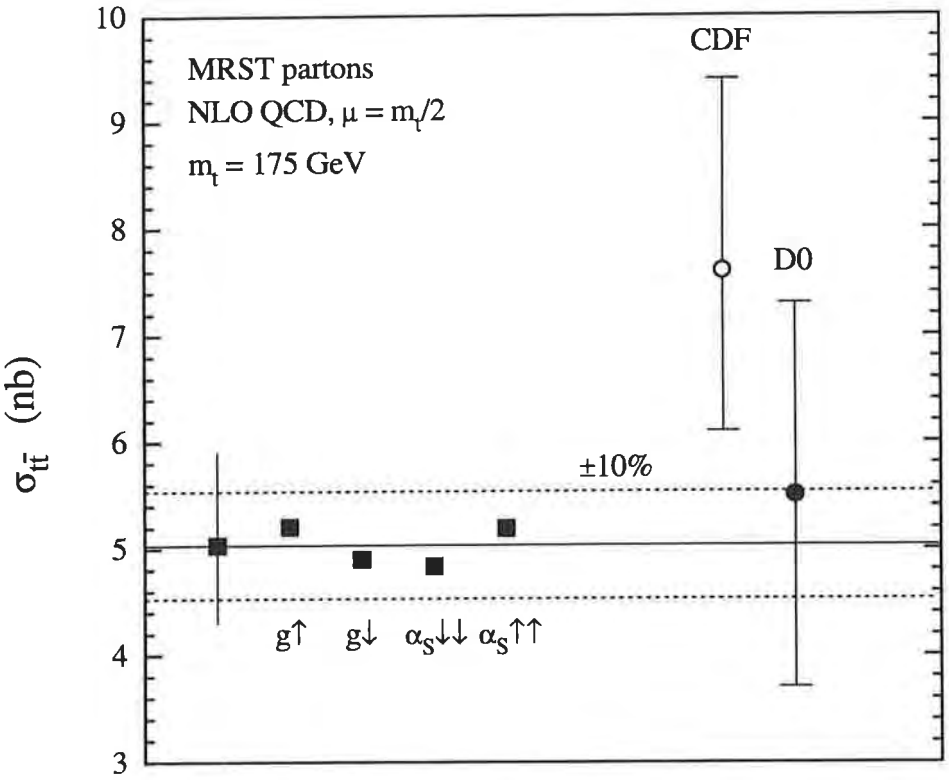

Figure 38: Predictions for the $t\bar{t}$ total cross section in $p\bar{p}$ collisions at 1.8 TeV using the five MRST parton sets. The error bars on the default MRST prediction correspond to a variation in the top mass of ± 5 GeV. Experimental measurements from CDF [65] and D0 [66] are shown.

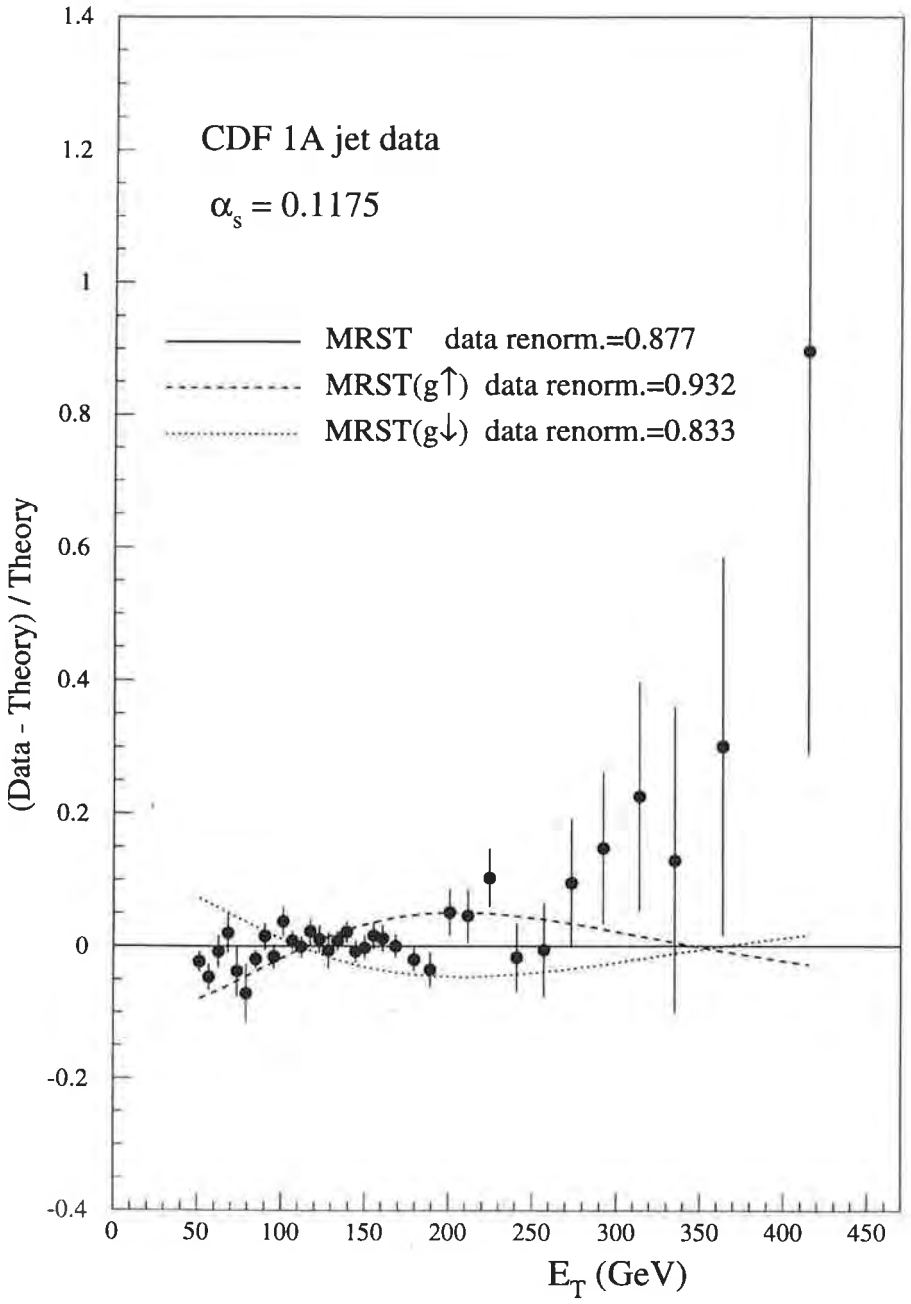

Figure 39: The next-to-leading order QCD description of the CDF [36] single jet inclusive E_T distribution by the MRST set of partons. The overall normalization of the QCD prediction is fitted to the data. The comparisons with the MRST($g\uparrow$) and MRST($g\downarrow$) parton sets are also shown.

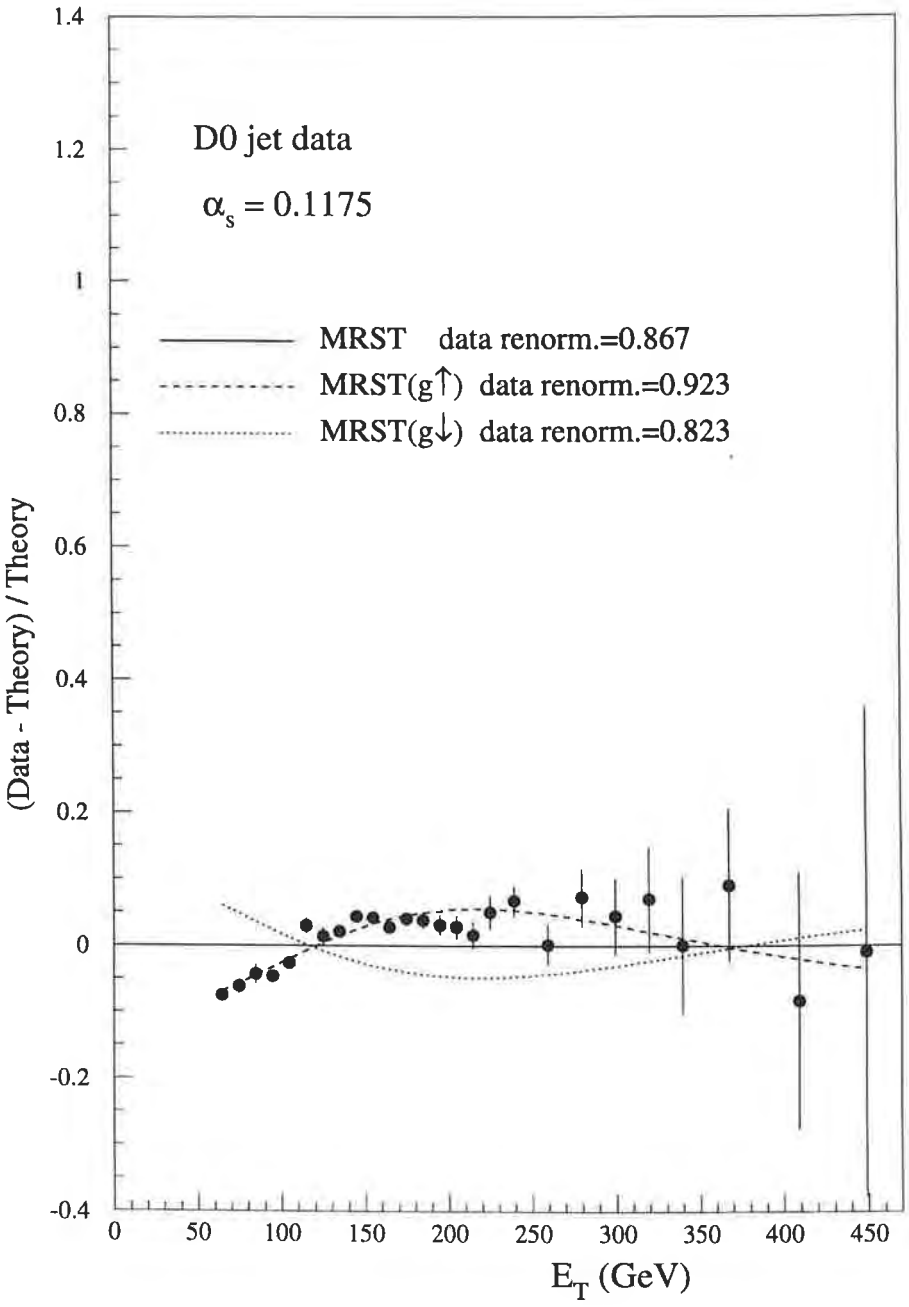

Figure 40: The next-to-leading order QCD description of the D0 [37] single jet inclusive E_T distribution by the MRST set of partons. The overall normalization of the QCD prediction is fitted to the data. The comparisons with the MRST($g\uparrow$) and MRST($g\downarrow$) parton sets are also shown.

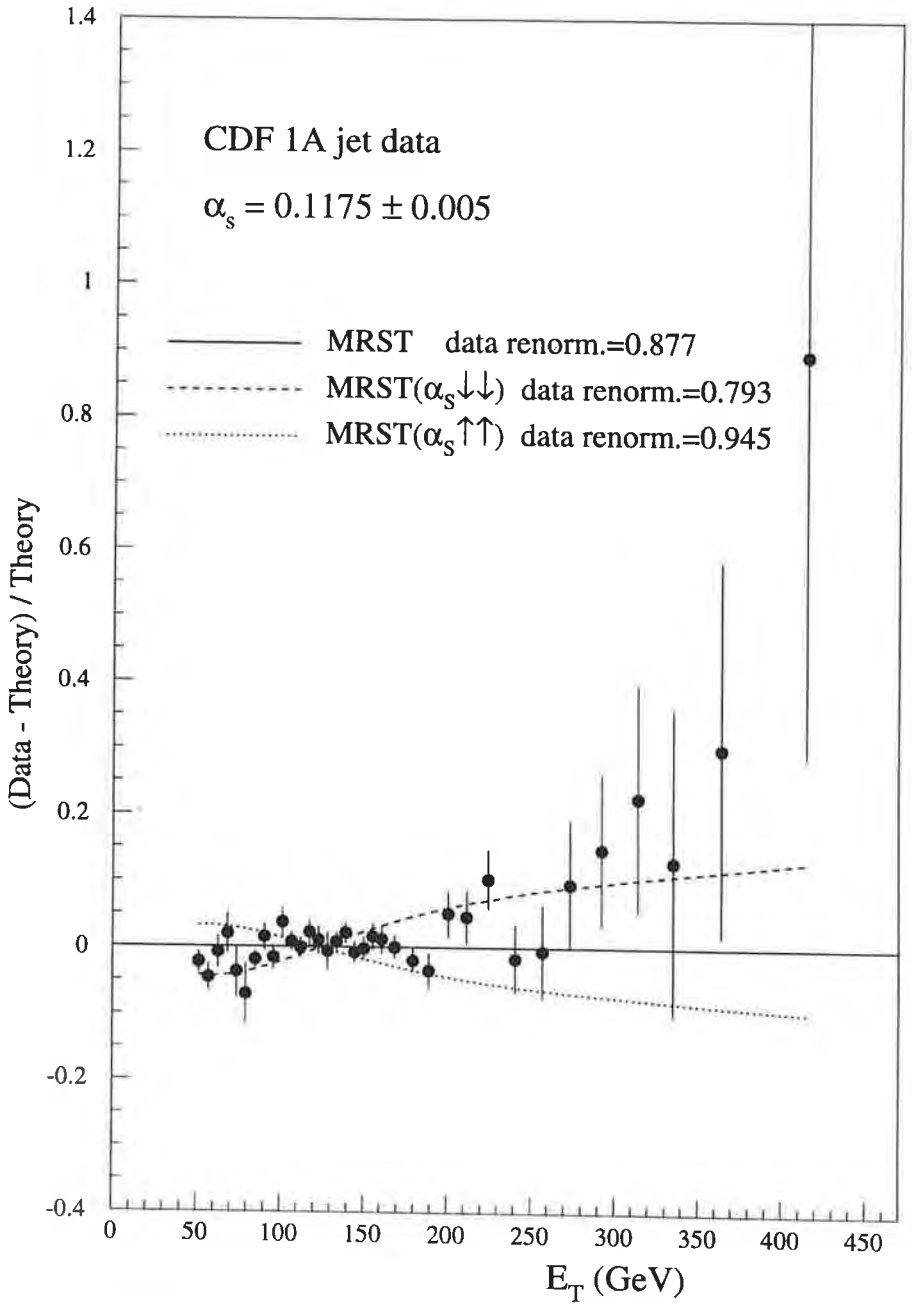

Figure 41: As for Fig. 39 but including the comparisons with the MRST($\alpha_S \uparrow\uparrow$) and MRST($\alpha_S \downarrow\downarrow$) parton sets.

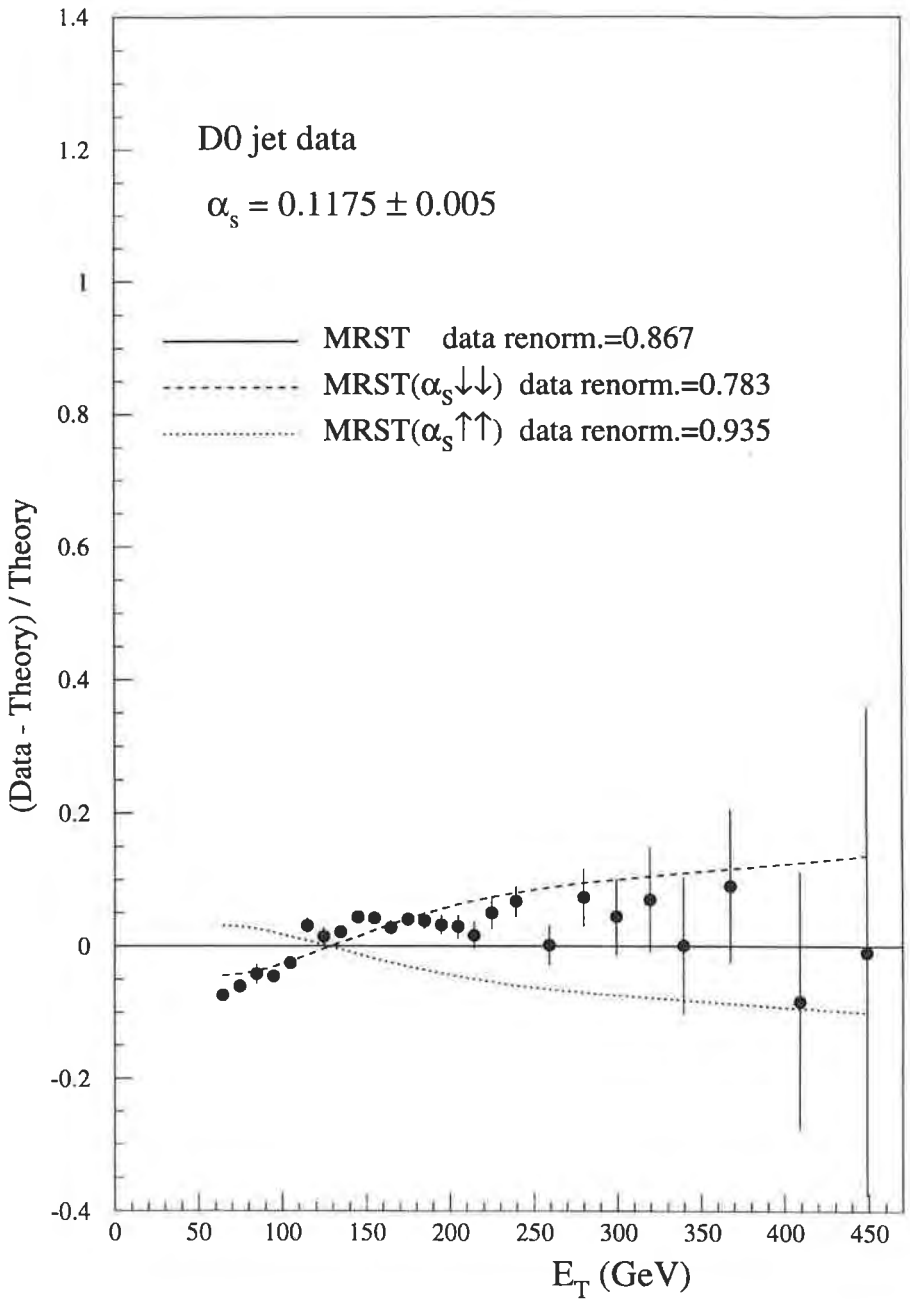

Figure 42: As for Fig. 40 but including the comparisons with the MRST($\alpha_S \uparrow\uparrow$) and MRST($\alpha_S \downarrow\downarrow$) parton sets.

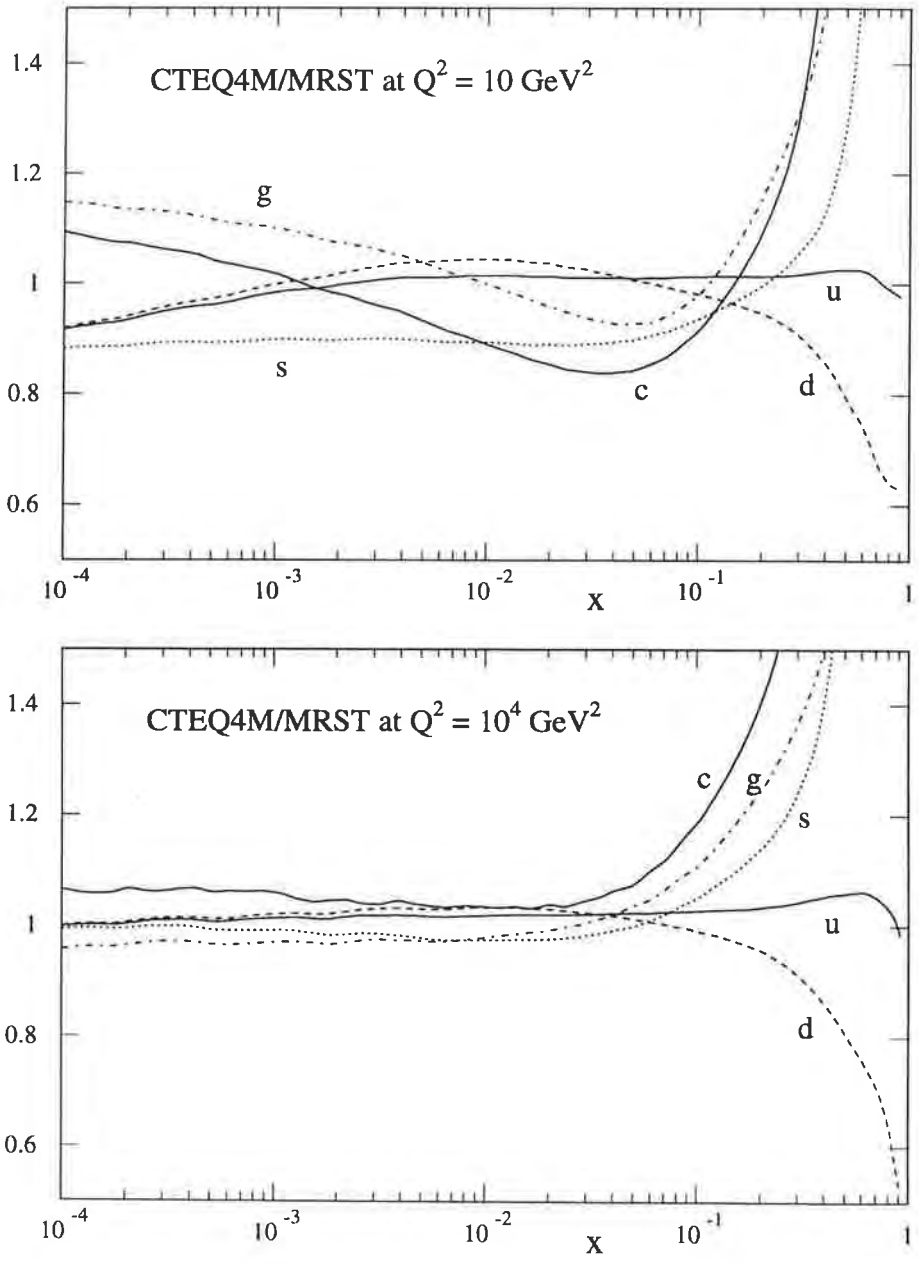

Figure 43: Ratio of the partons of the CTEQ4M [20] set to those of the MRST set at $Q^2 = 10$ and 10^4 GeV^2.